MAGNETIC REFRIGERATION: AN ATTRACTION TOWARD OUR FUTURE

CLAUDIA MASSELLI

Unione Europea

UNIVERSITÀ DEGLI
STUDI DI SALERNO

FONDO SOCIALE EUROPEO

Programma Operativo Nazionale 2000/2006
"Ricerca Scientifica, Sviluppo Tecnologico, Alta Formazione"
Regioni dell'Obiettivo 1 – Misura III.4
"Formazione superiore ed universitaria"

Department of Industrial Engineering

Ph.D. Course in Industrial Engineering
(XV Cycle-New Series, XXIX Cycle)

MAGNETIC REFRIGERATION: AN ATTRACTION TOWARD OUR FUTURE

Supervisor
Prof. Ciro Aprea

Ph.D. Student
Claudia Masselli

Co-Supervisors
Prof. Adriana Greco
Prof. Angelo Maiorino

Ph.D. Course Coordinator
Prof. Ernesto Reverchon

Acknowledgements

Special thanks go to the research group I belong to: my supervisor, Prof. Ciro Aprea, who has been a beacon that lit the Ph.D. way; the co-supervisor Prof. Angelo Maiorino who accompanied me in the experimental part, giving to me considerable food for thought; finally, special singular gratitude goes to the co-supervisor from University of Naples “Federico II”, Prof. Adriana Greco, who has constantly encouraged myself and led me by the hand to the achievement of several scientific goals.

Thanks to everyone who has supported myself during the Ph.D. period: my parents, Olimpia and Vincenzo, whose support has been essential; my boyfriend Daniele, who every day takes care of me with his love; the whole family, with special dedication to my aunt Marina, who is a great supporter of all my scientific achievements. Finally, thanks to all the friends and colleagues who accompanied me in these wonderful three years.

List of publications

Aprea C., Cardillo G., Greco A., Maiorino A. and **Masselli C.** (2014) La refrigerazione magnetica: simulazione numerica e risultati sperimentali a confronto Proc. of *III Congresso nazionale del coordinamento della meccanica.*, June 30th and July 1st, 2014, Naples, Italy. ISBN:8890209623.

Aprea C., Cardillo G., Greco A., Maiorino A. and **Masselli C.** (2015) An innovative rotary permanent magnetic refrigerator based on AMR cycle, Proc. of *ASME ATI UIT 2015, Conference on Thermal Energy Systems: Production, Storage, Utilization and the Environment*, May 17-20, 2015, Naples, Italy, ISBN 978-88-98273-17-1.

Aprea C., Cardillo G., Greco A., Maiorino A. and **Masselli C.** (2015) A comparison between first and second order phase magnetic transition materials for an AMR refrigerator at room temperature, Proc. of *ASME ATI UIT 2015, Conference on Thermal Energy Systems: Production, Storage, Utilization and the Environment*, May 17-20, 2015, Naples, Italy, ISBN 978-88-98273-17-1.

Aprea C., Greco A., Maiorino A. and **Masselli C.** (2015) Magnetic refrigeration: an eco-friendly technology for the refrigeration at room temperature. Proc. of *33rd UIT Heat Transfer Conference*, June 22-24, 2015, L'Aquila, Italy.

Aprea C., Cardillo G., Greco A., Maiorino A. and **Masselli C.** (2015) A comparison between experimental and 2D numerical results of a packed-bed active magnetic regenerator. *Appl. Therm. Eng.*, **90**, 376-383. DOI: 10.1016/j.applthermaleng.2015.07.020.

Aprea C., Greco A., Maiorino A. and **Masselli C.** (2015) A comparison between rare earth and transition metals working as magnetic materials in an AMR refrigerator in the room temperature range. *Appl. Therm. Eng.*, **91**, 767-777. DOI: 10.1016/j.applthermaleng.2015.08.083.

Aprea C., Greco A., Maiorino A. and **Masselli C.** (2015) Magnetic refrigeration: an eco-friendly technology for the refrigeration at room temperature. *J. of Phys.: Conf. Ser.* **655** (1), 012026. DOI:10.1088/1742-6596/655/1/012026.

Aprea C., Greco A., Maiorino A. and **Masselli C.** (2016c) The energy performances of a rotary permanent magnet magnetic refrigerator. *Int. J. of Refrig.*, **61**, 1-7. DOI: 10.1016/j.ijrefrig.2015.09.005

Aprea C., Cardillo G., Greco A., Maiorino A. and **Masselli C.** (2016) A rotary permanent magnet magnetic refrigerator based on AMR cycle. *Appl. Therm. Eng.*, **101**, 699-703. DOI: 10.1016/j.applthermaleng.2016.01.097.

Aprea C., Greco A., Maiorino A., **Masselli C.** and Metallo A. (2016) HFO1234yf as a drop-in replacement for R134a in domestic refrigerators: a life cycle climate performance analysis, Proc. of *10th AIGE 2016 and 1st AIGE/IIETA International Conference on "Energy Conversion, Management, Recovery, Saving, Storage and Renewable Systems*, June 9-10, 2016, Naples, Italy, ISSN: 0392-8764.

Aprea C., Greco A., Maiorino A. and **Masselli C.** (2016) A comparison between different materials in an active electrocaloric regenerative cycle with a 2D numerical model, *Int. J. of Refrig.*, **69**, 369-382. DOI: 10.1016/j.ijrefrig.2016.06.016.

Aprea C., Greco A., Maiorino A. and **Masselli C.** (2016) Electrocaloric refrigeration: an innovative, emerging, eco-friendly refrigeration technique Proc. of *34th UIT Heat Transfer Conference*, July 04-06, 2016, Ferrara, Italy.

Aprea C., Greco A., Maiorino A. and **Masselli C.** (2016) A two-dimensional investigation about magnetocaloric regenerator design: parallel plates or packed bed? Proc. of *34th UIT Heat Transfer Conference*, July 04-06, 2016, Ferrara, Italy.

Aprea C., Greco A., Maiorino A. and **Masselli C.** (2016) The optimization of the energy performances of a PMRR by using neural networks. Proc. of *7th IIR/IIF International Conference on Magnetic Refrigeration at Room Temperature*, THERMAG 2016; September 11-14, 2016, Torino, Italy. DOI: 10.18462/iir.thermag.2016.0132 - ISBN: 978-2-36215-016-6 - ISSN: 0151-1637.

Aprea C., Greco A., Maiorino A., **Masselli C.** and Metallo A. (2016) HFO1234ze as drop-in replacement for R134a in domestic refrigerators: an environmental impact analysis. Proc. of *71st Conference of the Italian Thermal Machines Engineering Association*, ATI 2016; September 14-16, 2016, Turin, Italy.

Aprea C., Greco A. and **Masselli C.** (2016) Magnetic refrigeration: an attraction toward the future, Proc. of XXII Convegno A.I.P.T, during participation to "Ermanno Grinzato" award.

Aprea C., Greco A., Maiorino A., **Masselli C.** and Metallo A. (2016) HFO1234yf as a drop-in replacement for R134a in domestic refrigerators: a life cycle climate performance analysis, *International Journal of Heat and Technology*, **34**, Special Issue 2. DOI:10.18280/ijht.34S2 - ISSN: 0392-8764.

Aprea C., Greco A., Maiorino A. and **Masselli C.** (2016) Electrocaloric refrigeration: an innovative, emerging, eco-friendly refrigeration technique. Accepted by *J. of Phys.: Conf. Ser*.

Aprea C., Greco A., Maiorino A. and **Masselli C.** (2016) A two-dimensional investigation about magnetocaloric regenerator design: parallel plates or packed bed? Accepted by *J. of Phys.: Conf. Ser*.

Aprea C., Greco A., Maiorino A., **Masselli C.** and Metallo A. (2016) HFO1234ze as drop-in replacement for R134a in domestic refrigerators: an environmental impact analysis, *Energy Procedia*, **101**, 964–971. DOI: 10.1016/j.egypro.2016.11.122.

Aprea C., Greco A., Maiorino A. and **Masselli C.** (2017) The drop-in of HFC134a with HFO1234ze in a household refrigerator, Submitted at *International Journal of Thermal Science.*

Aprea C., Greco A., Maiorino A. and **Masselli C.** (2017) A comparison between electrocaloric and magnetocaloric materials for solid state refrigeration, *International Journal of Heat and Technology*, **35**, 1.

Summary

Index of figures

Index of Tables

Abstract

Magnetic refrigeration is an innovative, promising and ecologic technology, which aims to substitute the conventional vapor-compression refrigeration by the employment of solid materials as refrigerants instead of the fluid-state ones, own of vapour compression refrigeration. This emerging technology bases its operation on the magnetocaloric effect (MCE), which is a physical phenomenon, related to solid-state materials with magnetic properties. The magnetic field causes an entropy change due to magnetic ordering. The maximum MCE occurs near the magnetic ordering temperature, which is recognized as the Curie temperature of a ferromagnetic material. For materials displaying simple magnetic ordering (i.e. paramagnetic to ferromagnetic phase transformations) a rapid increase in magnetic field causes a temperature rise in the material; likewise, a rapid reduction in the field causes cooling. This variation in temperature is called adiabatic temperature change which is a function of the magnetic field intensity and of the initial temperature.

To reach a useful temperature span it is required employing a regenerative thermodynamic cycle. In 1982, the employment of a reciprocating thermal regenerator coupled with magnetocaloric cycle has been shown: it was introduced the Active Magnetic Regenerative refrigeration cycle, well known as AMR cycle. The innovative idea leads to a new magnetic cycle, different from the previous ones (Carnot, Ericsson, Brayton, or Stirling). It considers a magnetic Brayton cycle but the main innovation consists of introducing the AMR regenerator concept, i.e. the employment of the magnetic material itself both as refrigerant and as regenerator. A secondary fluid is used to transfer heat from the cold to the hot end of the regenerator. Substantially every section of the regenerator experiments its own AMR cycle, according to the proper working temperature. Through an AMR one can appreciate a larger temperature span among the ends of the regenerator.

Active Magnetic Regenerator is the core of a magnetic refrigerator system. The performance of an AMR system strongly depends on the magnetocaloric effect of the magnetic material used to build the regenerator, on the geometry of the regenerator and on the secondary fluid.

The present thesis aims to explore, report and explain all the aspects of the research, treated during the PhD period. The personal contribution in the research field of magnetic refrigeration has combined both the numerical and the experimental research that have been done hand in hand.

At the Refrigeration Lab (LTF) of University of Salerno, the first Italian prototype of a Rotary Permanent Magnet Magnetic Refrigerator (RPMMR) has been projected and developed (Aprea et al., 2014), whose name is 8Mag and presents a rotating magnetic group whereas the magnetocaloric material (MCM) is stationary. Gadolinium has been selected as magnetic refrigerant and demineralized water has been employed as heat transfer fluid.

In the present thesis, the experimental tests conducted on the RPMMR have been presented, with the purpose to investigate the energy performances of the device, like temperature span, refrigerating power and COP, when the system was subjected to different operating conditions obtained by varying the cycle operating frequency, the thermal load, the volumetric flow rate of the auxiliary fluid and the temperatures of the cold and hot heat exchangers. In particular, the results of three different campaigns of tests are presented: 1) a primary campaign based on zero load tests; then two other campaigns have been conducted in order to explore the energetic performances of 8Mag: 2) by changing the cycle frequencies, the cooling load and fluid flow rate, while the hot side temperature was fixed, in order to give an overview of the performances and to underline an optimal operating frequency, for each set of operating conditions. 3) Fixing flow rate and AMR cycle frequency to the optimal value, a further investigation has been conducted by varying cooling load.

A two-dimensional numerical model of a packed bed- AMR regenerator has been developed, as primary purpose, to operate according to the prototype, since the model replicates the thermo-fluid-dynamical behavior of one of the RPMMR's regenerators, including the magnetocaloric effect acting into the solid refrigerant. To this aim, the model has been experimentally validated with experimental results provided by the prototype. This model has been used to optimize the experimental device and to identify significant areas of device improvement. Thus, it has been used to explore the critical aspects of 8Mag and to outline the way to improve performances. Anyway, the model has been easily generalized to consider different device geometries, temperature spans, secondary fluids, and magnetic materials. As a matter of fact, in this thesis are shown the results obtained investigating, through the model, the effect of other different magnetocaloric materials when they act as refrigerant employed in one of the AMR regenerator of the prototype. Moreover, the environmental impact in terms of greenhouse effect has also been investigated, by comparing the performances of the RPMMR with the one of a vapor compression plant in terms of TEWI index (Total Equivalent Warming Impact).

Introduction

Nowadays, the refrigeration is responsible of more than 17% of the overall energy consumption all over the world and most modern refrigeration units are based on Vapor Compression Plants (VCP). The traditional refrigerant fluids employing VCP, i.e. CFCs and HCFCs, have been banned by the Montreal Protocol in 1987 (Montreal Protocol, 1987), because of their contribution to the disruption of the stratospheric ozone layer (Ozone-Depleting Potential substances ODPs). Over time it has been following periodical meetings among the Parties to the Montreal Protocol. Since 2000 the usage of HCFCs in new refrigerating systems was forbidden, letting HFCs the only fluorinated refrigerants allowed because of their zero ODP characteristic. Since 2009, each meeting related to Montreal protocol, initially dedicated to the phase-out of the substances depleting the stratospheric ozone layer, namely CFCs and HCFCs, had been leading to conflicting exchanges on high Global Warming Potential HFCs which replace CFCs and HCFCs most of the time. Year after year, human activities have been increasing the concentration of greenhouse gases in the atmosphere, thus resulting in a substantial warming of both earth surface and atmosphere. The impact of greenhouse gases on global warming is quantified by their GWP (Global Warming Potential). Thus, over the year measures to reduces global warming have been taken, beginning with the Kyoto Protocol (Kyoto Protocol, 1997) and consequently with the EU regulations applying the prescriptions derived from it, like EU regulation 517/2014 (EU No 517/2014) on fluorinated greenhouse gases.

The above described general frameworks led scientific community to studying and applying (Aprea et al., 2012; Palm, 2008) resolutions with environmentally friendly gases, with small GWP and zero ODP: one of the most focused classes of new generation refrigerants is hydrofluoroolefins (HFO) (Aprea et al., 2016a; Mota-Babiloni et al., 2016), descending of olefins rather than alkanes (paraffins) and they are known as unsaturated HFCs, with environmentally friendly behavior, quite low costs. Despite all these advances, it is essential to underline that a vapor compression plant produces both a direct and an indirect contribution to global warming. The former depends on the GWP of refrigerant fluids and on the fraction of

refrigerant charge which is either directly released in the atmosphere during operation and maintenance, or is not recovered when the system is scrapped. The indirect contribution is related to energy-consumption of the plant. In fact, a vapor compression refrigerator requires electrical energy produced by a power plant that typically burns a fossil fuel, thus releasing CO_2 into the atmosphere. The amount of CO_2 emitted is a strong function of the COP of the vapor compression plant.

For all these reason, in the last decades the interest of scientific community has oriented itself in studying and developing new refrigeration technologies of low impact in our ecosystem: a class of them is composed by solid-state cooling (Kitanovski and Egolf, 2006; Ožbolt et al., 2014; Tušek et al., 2015), which are gaining more and more attention, due to their potential in being performing and ecological methodologies. Recent discoveries of giant caloric effects (Pecharsky and Gschneidner, 1997; Lu et al., 2010; Liu et al., 2014) in some ferric materials have opened the door to the use of solid-state materials as an alternative to gases for conventional and cryogenic refrigeration.

Actually, the most promising, eco-friendly, emerging solid-state technique is constituted by magnetic refrigeration (MR) (Kitanovski et al., 2016), whose main innovation consists in employing solid materials with magnetic properties as refrigerants, able to increase or decrease their temperature when interacting with a magnetic field. Instead of the fluid refrigerants, proper of vapour compression, a magnetic refrigerant is a solid and therefore it has essentially zero vapour pressure, which means no direct ODP and zero GWP.

Specifically, magnetic refrigeration is related to magnetocaloric effect (MCE) (Warburg, 1881), a physical phenomenon observed in some material with magnetic properties and it consists in an increment of temperature in the MCE material because of material's magnetization under adiabatic conditions. A regenerative Brayton based thermodynamical cycle, called Active Magnetic Regenerative refrigerant (AMR) cycle, is the one where magnetic refrigeration founds its operations. Therefore, Active Magnetic Regenerator is the core of a magnetic refrigerator system. It is a special kind of thermal regenerator made of material with magnetic properties, which works both as a refrigerant and as a heat regenerating medium. The performance of an AMR system strongly depends on the magnetocaloric effect of the magnetic material used to build the regenerator, on the geometry of the regenerator and on the operating conditions of the system. The cooling efficiency in magnetic refrigerators can reach 60% of the theoretical limit, as compared to the 40% achieved by the best vapor compression plant.

At the Refrigeration Lab (LTF) of University of Salerno, the first Italian prototype of a Rotary Permanent Magnet Magnetic Refrigerator (RPMMR) has been projected and developed (Aprea et al., 2014), whose name is 8Mag

and presents a rotating magnetic group whereas the magnetocaloric material (MCM) is stationary. Gadolinium has been selected as magnetic refrigerant and demineralized water has been employed as heat transfer fluid. The total mass of gadolinium (1.20 kg), shaped as packed bed spheres, is housed in 8 regenerators. A magnetic system, based on a double U configuration of permanent magnets, provides a magnetic flux density of 1.25 T with an air gap of 43 mm. A rotary vane pump forces the regenerating fluid through the regenerators.

The present thesis aims to explore, report and explain all the aspects of the research, treated during the PhD period. The personal contribution in the research field of magnetic refrigeration has combined both the numerical and the experimental research that have been done hand in hand.

A two-dimensional numerical model of a packed bed- AMR regenerator has been developed, as primary purpose, to operate according to the prototype, since the model replicates the thermo-fluidodynamic behavior of one of the RPMMR's regenerators, including the magnetocaloric effect acting into the solid refrigerant. To this aim, the model has been experimentally validated (Aprea et al., 2015a) with experimental results provided by the prototype. This model has been used to optimize the experimental device and to identify significant areas of device improvement. Thus, it has been used to explore the critical aspects of 8Mag and to outline the way to improve performances. Anyway, the model has been easily generalized to consider different device geometries, temperature spans, secondary fluids, and magnetic materials. To this purpose, the model has been tested when employing new magnetocaloric materials (Aprea et al., 2015b), whose performance have been also compared (Aprea et al., 2015c), from an environmental point of view, with the ones of a commercial vapor-compression refrigerator working with R134a. Moreover, additional investigations have been conducted to explore the behavior of the regenerator with a parallel-plate configuration (Aprea et al., 2016b), employing a number of different magnetocaloric materials.

As a matter of fact, in this thesis are shown the results obtained investigating (Aprea et al., 2015b), through the model, the effect of other different magnetocaloric materials when they act as refrigerant employed in one of the AMR regenerator of the prototype. Different magnetic materials have been considered as refrigerant: second order phase magnetic transition materials, like pure gadolinium, $Pr_{0.45}Sr_{0.35}MnO_3$ and first order phase magnetic transition alloys $Gd_5(Si_xGe_{1-x})_4$, $LaFe_{11.384}Mn_{0.356}Si_{1.26}H_{1.52}$, $LaFe_{11.05}Co_{0.94}Si_{1.10}$ and $MnFeP_{0.45}As_{0.55}$. Such materials have also been object of an additional investigation (Aprea et al., 2016b) related to the evaluation of the performances between two different geometries of the AMR regenerator: packed-bed and parallel-plate. Moreover, the environmental impact in terms of greenhouse effect has also been investigated, by comparing (Aprea et al., 2015c) the performances of the

RPMMR with the one of a vapor compression plant in terms of TEWI index (Total Equivalent Warming Impact). A vapor compression plant (VCP) produces both a direct and an indirect contribution to global warming, whereas an AMR cycle has only an indirect effect. The analysis has been performed comparing the VCP and the magnetic refrigerator when the latter is working with several different magnetocaloric refrigerants.

Furthermore, are also presented the experimental tests conducted (Aprea et al, 2016c) on the RPMMR, with the purpose to investigate the energy performances of the device, like temperature span, refrigerating power and COP, when the system was subjected to different operating conditions obtained by varying the cycle operating frequency, the thermal load, the volumetric flow rate of the auxiliary fluid and the temperatures of the cold and hot heat exchangers. The results of three different campaigns of tests are presented: 1) a primary campaign based on zero load tests; then two other campaigns have been conducted to explore the energetic performances of 8Mag: 2) by changing the cycle frequencies, the cooling load and fluid flow rate, while the hot side temperature was fixed, in order to give an overview of the performances and to underline an optimal operating frequency, for each set of operating conditions. 3) Fixing flow rate and AMR cycle frequency to the optimal value, a further investigation has been conducted by varying cooling load.

Chapter I
Magnetic refrigeration: generalities

I.1 Magnetocaloric effect

Magnetocaloric effect is an intrinsic property of all solid-state materials, due to the coupling between the magnetic spin and the crystal lattice with an external magnetic field whom produces a change in magnetic entropy contribution. When the material is magnetized there will be some ordering of the magnetic spins, forcing them towards the direction of the applied field. If this is done isothermally, this will reduce the material's magnetic entropy by the isothermal entropy change (ΔS_M). On the other side, if the magnetization is done adiabatically, without any thermal interaction with the external ambient, the total sample entropy remains constant and the decrease in magnetic entropy is countered by an increase in the lattice and electron entropy. This causes a heating of the material and a temperature increase given by the adiabatic temperature change (ΔT_{ad}). The inverse procedure also applies: under adiabatic demagnetization the magnetic entropy increases, causing a decrease in lattice vibrations and by that a temperature decrease.

I.1.1 Historical background

MagnetoCaloric Effect (MCE) is a physical phenomenon discovered casually in 1881 by Emil Gabriel Warburg, a German professor of Physics at University of Strasbourg, during some experiments on ferromagnetic materials. Warburg observed (Warburg, 1881) a slight increment of temperature when the material was subjected to a huge magnetic field whereas, once it was extracted from the field, its temperature suffered a decrease. Cryogenic temperatures have been the first branch of refrigeration

where MCE found application, since 1920 (Debye, 1926; Giauque, 1927). It is maturely used in liquefaction of hydrogen and helium.

The research on room temperature magnetic refrigerators has taken place since 1976 with the first prototype developed by Brown at the NASA Lewis Research Centre (Brown, 1976). In 1982, the employ of a reciprocating thermal regenerator coupled with magnetocaloric cycle has been shown. It is well known as Active Magnetic Regenerator (AMR) (Barclay, 1982). Since then an appreciable number of AMR-based experimental prototypes have been developed, with a different configuration of regenerators, different magnetic materials and different magnetic source (Yu et al., 2010; Tomc et al., 2013; Tušek et al., 2013; Vuarnoz and Kawanami, 2013; Engelbrecht and Pryds, 2014; Jotani et al., 2014). Nevertheless, most of the experimental devices don't provide yet results in terms of energetic performances, cooling power and temperature span as satisfactory as being comparable with the one provided by vapor compression systems.

I.1.2 Magnetic substances and their classification

Every material able to interact with a magnetic field and therefore characterized by magnetic properties, belongs to the magnetic substances. A magnetic substance is conceivable as a collection of small magnetic dipoles, associated with its atomic characteristics that are oriented casually. If the substance interacts with an external magnetic field, whom is characterized by an intensity H>0, the dipoles orient themselves in the same direction of the field and the substance is magnetized. **M** is the magnetization field and is defined as the magnetic moment of the substance per unit of volume:

$$\boldsymbol{M} = \frac{\sum_i \boldsymbol{m_i}}{V} \tag{I.1}$$

where $\boldsymbol{m_i}$ is the magnetic moment related to the i^{th} molecule of the substance contained in the volume *V*.

It is possible relating **M** and the magnetic field **H** as:

$$\boldsymbol{M} = \chi \boldsymbol{H} \tag{I.2}$$

where χ is the magnetic susceptibility of the substance and it is dimensionless.

The relation between the magnetic field induction **B** and the magnetic field **H** is given by:

$$\boldsymbol{B} = \mu \boldsymbol{H} \tag{I.3}$$

where μ is the magnetic permeability of the materials, which expresses the attitude of the material in being magnetized. The magnetic permeability can be always reported as function of μ_0, the magnetic permeability of the vacuum:

$$\mu = \mu_r \mu_0 \tag{I.4}$$

where μ_r is the relative permeability index, depending on the magnetic substance.

The magnetic permeability and the magnetic susceptibility are related by the following relationship:

$$\mu = \mu_0(1 + \chi) \tag{I.5}$$

Therefore, considering (I.5) and (I.2), (I.3) could be also expressed as:

$$\boldsymbol{B} = \mu_0(\boldsymbol{H} + \boldsymbol{M}) \tag{I.6}$$

The magnetic substances are classifiable in:

a) diamagnetic;
b) paramagnetic;
c) ferromagnetic.

The diamagnetic materials, when come under the action of an external magnetic field **H**, see their dipoles ordering in opposition to **H**; the associated magnetization field **M** has opposite direction of **H**. Therefore, a diamagnetic material tends to weaken the external field, as shown in figure I.1.

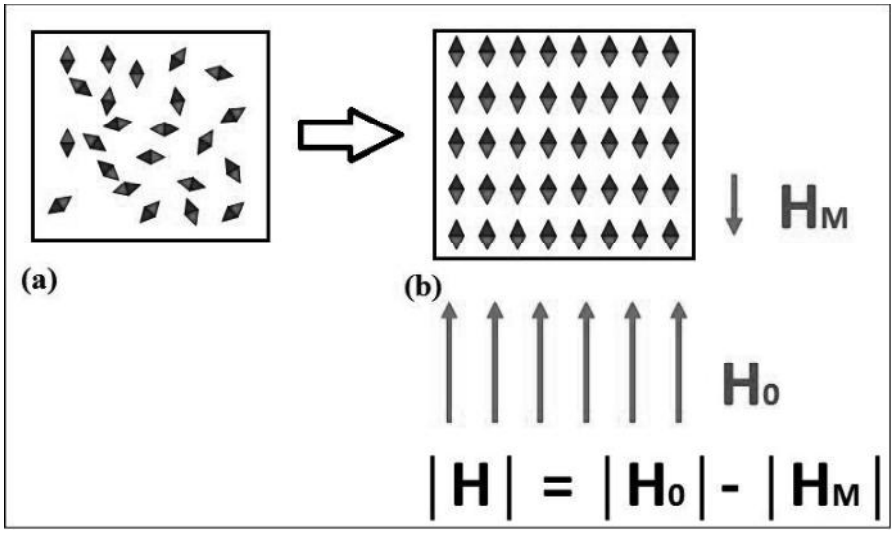

Figure I.1 *(a) A microscopic view of a demagnetized diamagnetic material; (b) a microscopic view of a magnetized diamagnetic material.*

The susceptibility of diamagnetic materials is always negative and non-depending both by temperature and by the magnetic field intensity, as shown in figures I.2(a) and I.2(b). Thus, the function which relies **M** and **H** is linearly decreasing, as plotted in figure I.3.

The most common diamagnetic materials are water, most of organic substances and some metals like mercury, gold, silver, copper and bismuth. For all of them, magnetic susceptibility belongs to $-10^{-4} \div -10^{-6}$ range.

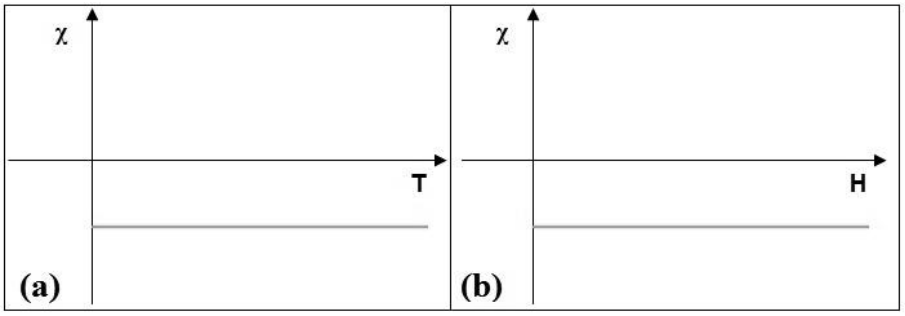

Figure I.2 *The susceptibility of a diamagnetic material as a function of: (a) temperature,(b) magnetic field intensity.*

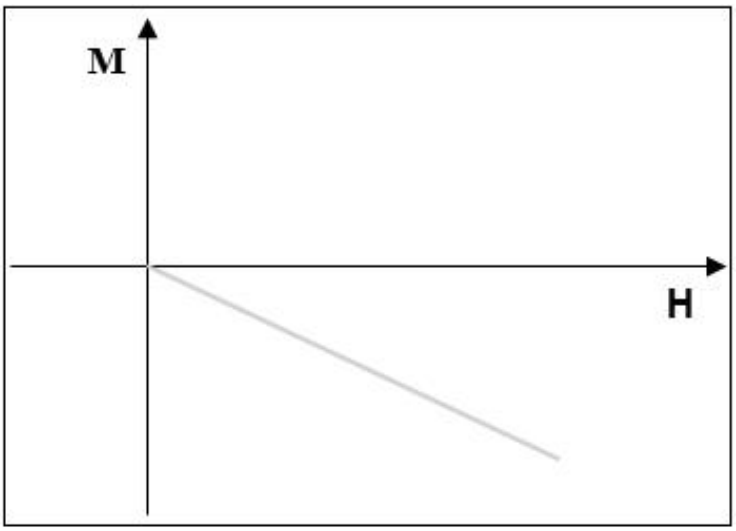

Figure I.3 *The magnetization field of a diamagnetic material as a function of magnetic field intensity.*

A magnetic substance is defined paramagnetic if, when it is under the action of an external magnetic field **H**, its dipoles orient themselves in the same direction of the field; the associated magnetization field **M** tends to strengthen **H**, since the two field are in phase, as shown in figure I.4.

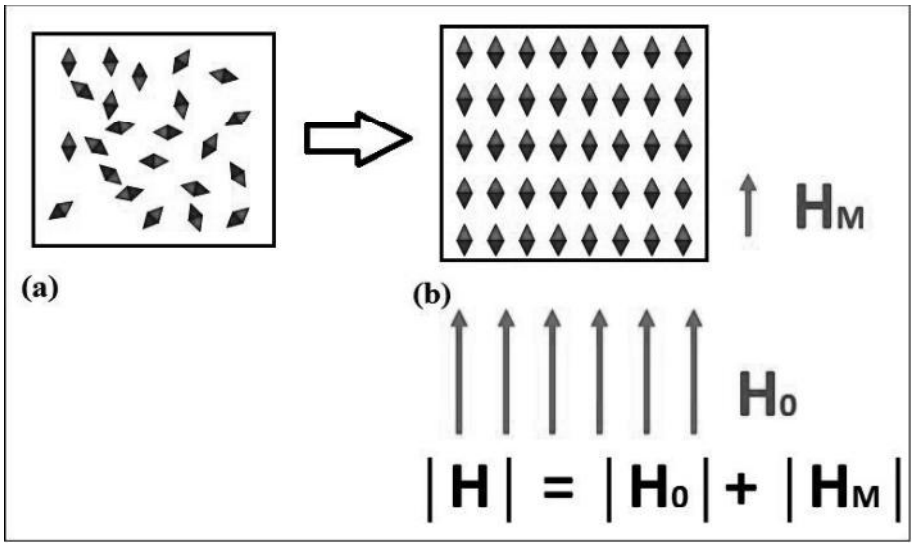

Figure I.4 *(a) A microscopic view of a demagnetized paramagnetic material; (b) a microscopic view of a magnetized paramagnetic material.*

The susceptibility χ of paramagnetic materials is always positive and independent by the external magnetic field. Moreover, χ is decreasing when temperature increases, because thermal agitations and lattice vibrations hinder the alignment of the magnetic moments of the atoms, in the **H** direction. The relationship between susceptibility and temperature, in paramagnetic materials is called *1st Curie law* and is given by:

$$\chi = \frac{\rho C}{T} \qquad \text{(I.7)}$$

where C is called Curie constant and its value depends of the material.
Figures I.5(a) and I.5(b) plot the χ trends as function of magnetic field and temperature, respectively.

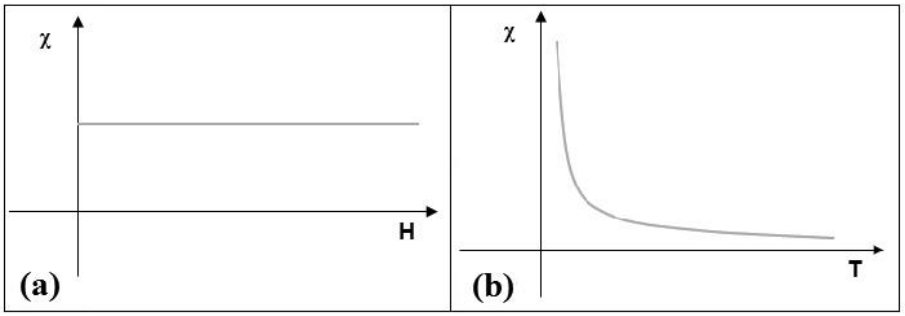

Figure I.5 *The susceptibility of a paramagnetic material as a function of: (a) magnetic field intensity, (b) temperature.*

As a result, **M** and **H** are bound by a linearly increasing function, as reported in figure I.6. The most common paramagnetic materials are aluminium, platinum, magnesium, calcium, sodium, oxygen and uranium. For all of them, magnetic susceptibility belongs to $10^{-4} \div 10^{-5}$ range, at room temperature.

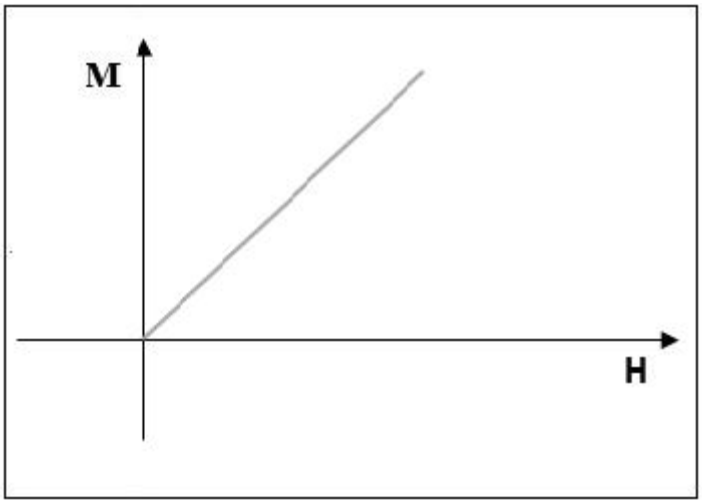

Figure I.6 *The magnetization field of a paramagnetic material as a function of magnetic field intensity.*

Ferromagnetic are all the materials whose susceptibility is strongly dependent by both the temperature and the applied magnetic field. Moreover, a ferromagnetic material is able to keep the magnetic moment even when the magnetizing field has been removed. The lattice structure of ferromagnetic materials is composed by a number of subdomains where the dipoles contained in, are locally aligned in the same direction. When a magnetizing filed is applied, all the dipoles of all the subdomains are arranged in the field direction, thus resulting in ferromagnetic material's magnetization, as shown in figures I.7(a) and I.7(b). The energy spent to demagnetize the material manifests itself in a delay in response, said hysteresis. Moreover, the correspondence between magnetic field induction **B** and the applied magnetic field **H** is regulated by the hysteresis loop, reported in figure I.8, which represents the state diagram of the ferromagnetic material. The shape of the hysteresis loop strongly depends by the material's characteristics, as well as by the intensity of the applied field.

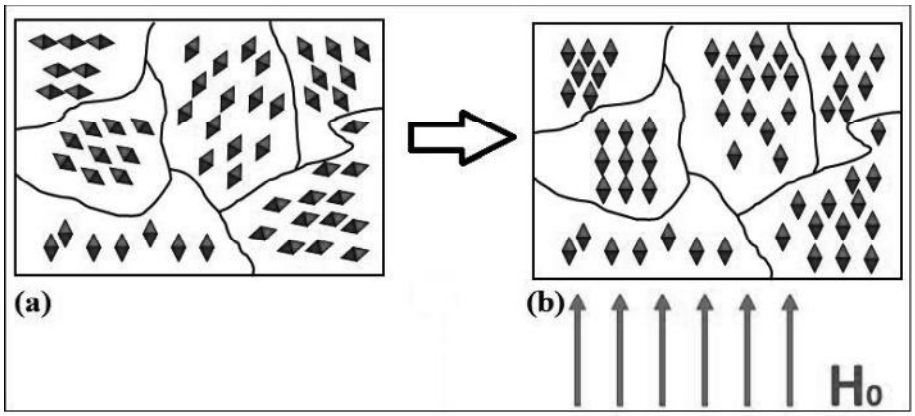

Figure I.7 *(a) A microscopic view of a demagnetized ferromagnetic material; (b) a microscopic view of a magnetized ferromagnetic material.*

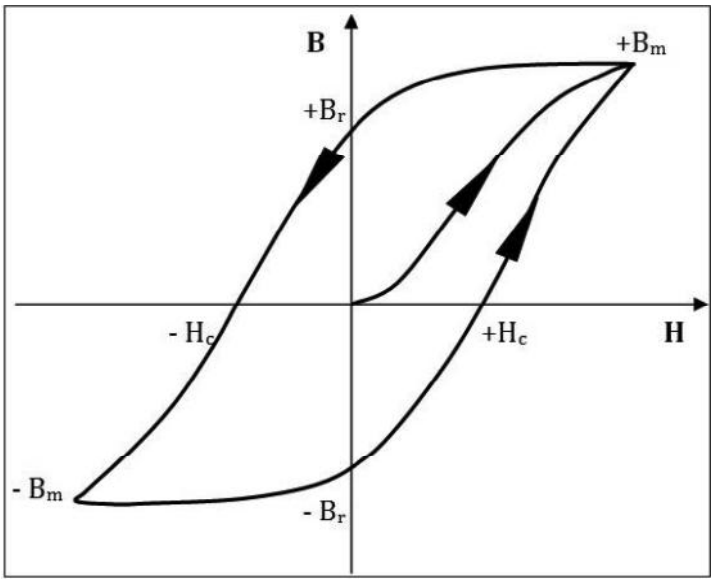

Figure I.8 *The hysteresis loop of a ferromagnetic material.*

The susceptibility χ of ferromagnetic materials obeys to the 2nd Curie law (also called Curie-Weiss law), visible in figure I.9(a), as follows:

$$\chi = \frac{\rho C}{T - T_c} \tag{I.8}$$

T_C is a critical temperature, called Curie temperature, where χ is maximum and above which, the material assumes a paramagnetic behaviour. Thus, the Curie temperature is also the temperature where the ferromagnetic to

paramagnetic transition takes place. The dependence of the susceptibility with the magnetic field is plotted in figure I.9(b).

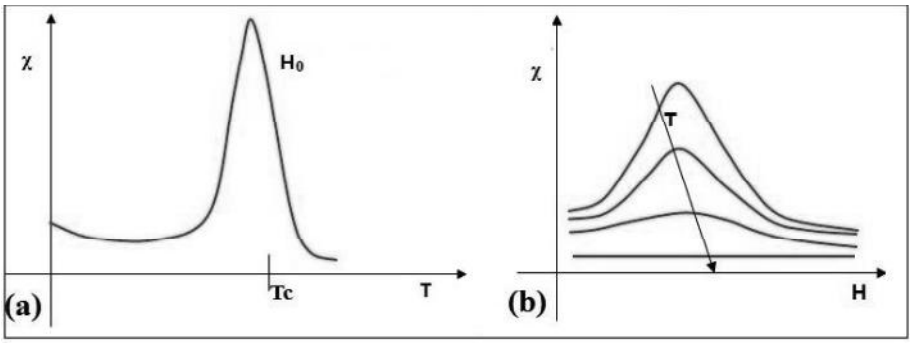

Figure I.9 *The susceptibility of a ferromagnetic material as a function of: (a) temperature, (b) magnetic field intensity.*

As a result, also the dependence of between the magnetization and the field is not linear anymore but regulated by the hysteresis loop, as illustrated in figure I.10.

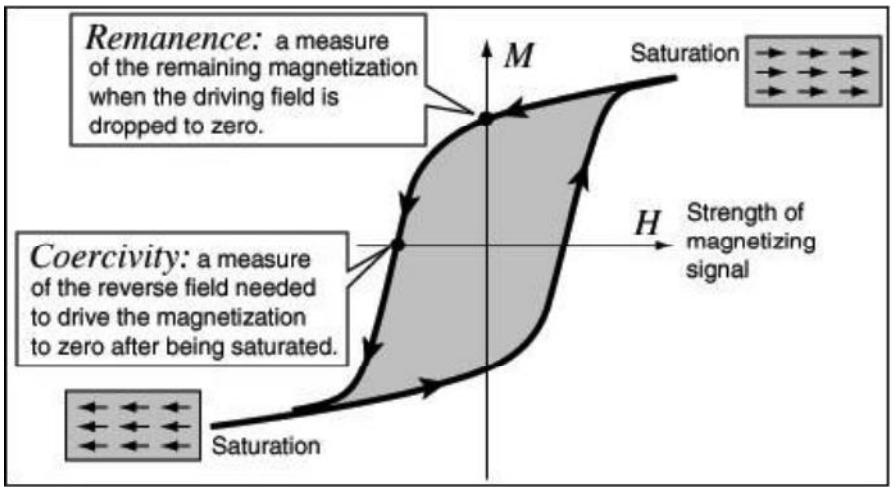

Figure I.10 *The hysteresis loop of magnetization field as a function of magnetic field intensity, in a ferromagnetic material.*

Some materials which belong to the ferromagnetic class are gadolinium, iron, nickel, as well as several iron-based alloys.

I.1.3 The entropy

Entropy *S* is a measure of the "disorder" of any physical system; its unit of measure in the international measurement system is Joule divided by Kelvin [J/K].

The entropy of a magnetic substance depends both by the temperature and the magnetic field and it is composed by three terms:

$$S(T,H) = S_L(T) + S_E(T) + S_M(T,H) \quad \text{(I.9)}$$

The first contribution $S_L(T)$ is called *vibrational entropy* since considers the disorder of the material due to the increase of lattice vibrations, when the system is supplied energy as heat. The heat supplying takes to another term of disorder: $S_L(T)$, the *electronic entropy*, which measure the disorder of system due to the increasing randomness of the electronic spins. The third contribution $S_M(T,H)$, called *magnetic entropy*, is related both to temperature and magnetic field. When the magnetic material goes under the presence of an external magnetic field, its magnetization takes the dipoles aligning with the field e therefore an increment of magnetic order, as well as a reduction of $S_M(T,H)$. Dually, when the external field is removed, the random disposition of the dipoles led to an increase of magnetic entropy. Figure I.11 plot the entropy curves of a ferromagnetic substance, together with the trends of the single contributions.

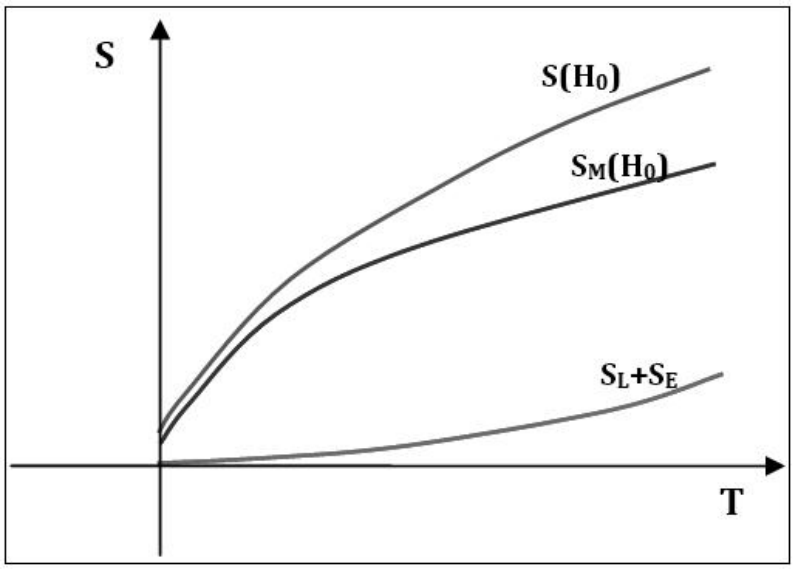

Figure I.11 *The entropy curves of a ferromagnetic material. Green line plots the totally entropy whereas blue and red line represent the magnetic and the thermal contributions, respectively.*

I.1.4 Heat capacities in magnetic materials

The heat capacity related to a generic process where the z parameter remains constant is:

$$C_z = \frac{\delta q_z}{dT} \tag{I.10}$$

Considering the second law of thermodynamic for a reversible process:

$$TdS = \delta q \tag{I.11}$$

the (I.10) becomes:

$$C_z = T\left(\frac{\partial S}{\partial T}\right)_z \tag{I.12}$$

In analogies with heath capacity at constant pressure and volume, for magnetic materials is interesting to consider the heat capacity at constant magnetic field and the heat capacity at constant magnetization, respectively defined as:

$$C_H = T\left(\frac{\partial S}{\partial T}\right)_H \tag{I.13}$$

$$C_M = T\left(\frac{\partial S}{\partial T}\right)_M \tag{I.14}$$

In the class of ferromagnetic materials C_H exhibits a peak at the Curie temperature of the material. Moreover, the temperature where the peak is located increases according to the intensity of the applied magnetic fields.

I.1.5 Magnetocaloric effect and magnetic transition materials

Magnetocaloric effect is a physical phenomenon, related to solid-state materials with magnetic properties. MCE consists in a coupling between the entropy of the Magnetocaloric Material (MM) and the variation of an external magnetic field applied to the material, which causes magnetic ordering in the MM structure. If the magnetization is done isothermally, it will decrease the magnetic entropy of the material, by the isothermal entropy change ΔS_M and, therefore, a change in the total entropy of the magnetic material is registered.

On the other side, if the magnetization occurs in an adiabatic process, without any interaction with the external environment, the total entropy of MM remains constant and the consequent decreasing in magnetic entropy is countered by an increase in the lattice and electron entropy contributions. This causes a heating of the material and a temperature increase given by the adiabatic temperature change (ΔT_{ad}). In figure I.12 are clearly visible the

quantities ΔS_M and ΔT_{ad} during an adiabatic magnetization of a ferromagnetic material.

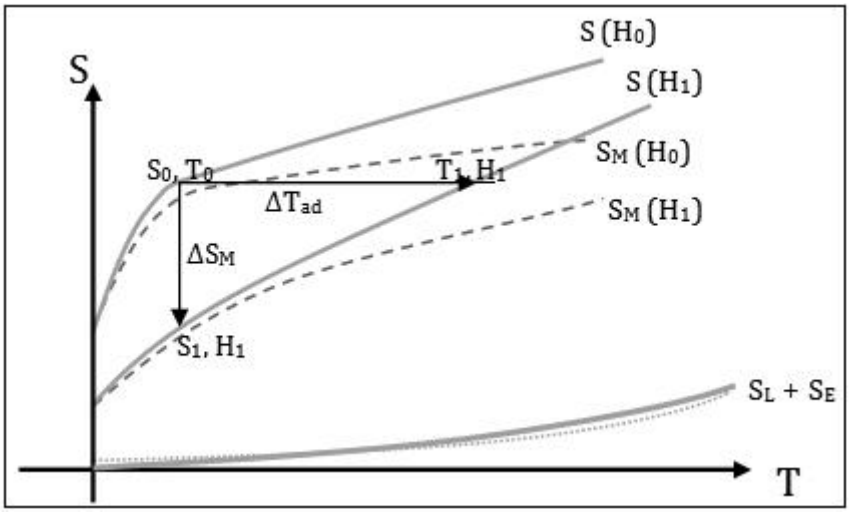

Figure I.12 *The magnetocaloric effect detected as ΔS_M and ΔT_{ad} in a ferromagnetic material where it is magnetized by magnetic field going from H_0 to H_1.*

Dually, under adiabatic demagnetization the magnetic entropy increases, causing a reduction in lattice vibrations and therefore a temperature decrease. At its Curie temperature, where is located its own magnetic phase transition, a MM shows the peak of MCE, in terms of ΔT_{ad} and ΔS_M. This occurs because the two opposite forces (the ordering force due to exchange interaction of the magnetic moments, and the disordering force of the lattice thermal vibrations) are approximately balanced near the Curie point T_C.

Hence, the isothermal application of a magnetic field produces a much greater increase in the magnetization (i.e., an increase of the magnetic order and, consequently, a decrease in magnetic entropy, ΔS_M) near the Curie point, rather than far away from T_c. The effect of magnetic field above and below T_c is significantly reduced because only the paramagnetic response of the magnetic lattice can be achieved for $T \gg T_c$, and for $T \ll T_c$ the spontaneous magnetization is already close to saturation and cannot be increased much more. Similarly, the adiabatic application of a magnetic field leads to an increase in the magnetic material temperature, ΔT_{ad}, which is also sharply peaked near the T_c.

The two possible magnetic phase changes that one can observe at the Curie point are First Order Magnetic Transition (FOMT) and Second Order Magnetic Transition (SOMT). At the Curie point a magnetic transition has FOMT characteristics when the material exhibits a discontinuity in the first derivative of the Gibbs free energy (G.f.e.), magnetization function, whereas

has a SOMT behavior when the gap is detected in the second derivative of G.f.e., magnetic susceptibility, while its first derivative is a continuous function. Most of the magnetic materials order with a SOMT from a paramagnet to a ferromagnet, ferrimagnet or antiferromagnet.

Considering an internally reversible process, the MCE for SOMT materials can be evaluated as:

$$(\Delta S_M)_T = \mu_0 \int_{H_i}^{H_f} \left(\frac{\partial M}{\partial T}\right)_H dH \quad \text{(I.15)}$$

$$(\Delta T_{ad})_s = -\mu_0 \int_{H_i}^{H_f} \frac{T}{C_H} \left(\frac{\partial M}{\partial T}\right)_H dH \quad \text{(I.16)}$$

For that reason, in a SOMT material, while $|(dM/dT)_H|$ exhibits its maximum value, one can register the peak of MCE, located at the Curie temperature or near absolute zero, respectively if the material is a ferromagnetic or paramagnetic. Instead in a FOMT material, the phase transition should ideally take place at constant temperature for an infinite value of $|(dM/dT)_H|$ resulting a giant magnetocaloric effect. The FOMT materials exhibit both an instantaneous orientation of magnetic dipoles and a latent heat correlated with the transition. Moreover, in some FOMT materials it is possible observing a coupled magnetic and crystallographic phase transition. Thus, in this case, applying a magnetic field to these FOMT materials, can produce both the magnetic state transition from a paramagnet or an antiferromagnet to a ferromagnet, simultaneously with a structural variation or a significant phase volume discontinuity but without showing a clear crystallographic alteration. Since that partial first derivatives of G.f.e. regarding T or H present a discontinuity at the first order phase transition, the bulk magnetization varies by ΔM and C_H ideally has an infinite value at the Curie temperature. Therefore, the isothermal magnetic entropy change (ΔS_M) in a FOMT material can be estimated by (I.17) coming from the Clasius-Clapeyron equation:

$$(\Delta S_M)_T = \left(\frac{dH}{dT_c}\right)_{eq} (\Delta M)_T \quad \text{(I.17)}$$

where the derivative is kept at equilibrium.

The discovery of giant magnetocaloric effect in $Gd_5(Si_{4-x}Ge_x)$, reported by Pecharsky and Gschneidner in 1997 (Pecharsky and Gschneidner Jr., 1997), stimulated a considerable growth of research to both find new materials where the effect is just as potent and to understand the role of magneto-structural transitions play in its enhancement. Giant MCE in FOMT materials, already observed, comes out since it is the result of two phenomena: the conventional magnetic entropy-driven process (magnetic entropy variation ΔS_M) and the difference in the entropies of the two crystallographic alterations (structural entropy variation ΔS_{ST}). The second

terms considers the greater contribution due to entropy variation in FOMT with respect to SOMT materials:

$$(\Delta S)_T = (\Delta S_M)_T + (\Delta S_{ST})_T \quad \text{(I.18)}$$

Assuming T/C_H constant, in a FOMT material ΔT_{ad} could be estimated as:

$$(\Delta T_{ad})_s = -\mu_0 \left(\frac{T}{C_H}\right)\left(\frac{dH}{dT_c}\right)(\Delta M)_T \quad \text{(I.19)}$$

The peak of adiabatic temperature variation is greater in most of the FOMT than SOMT materials.

There are fundamental differences in the behavior of FOMT and SOMT materials:

- in a first order transition the MCE is concentrated in a narrow temperature range, whereas in a second order the transition spread over a broad temperature range.
- In a SOMT materials the adiabatic temperature variation is nearly immediate whereas it doesn't happen in FOMT materials because of the consequent alteration in their crystallographic structure, which produces a displacement of the atoms, needing thus of an amount of time required many orders of magnitude larger. The non-instantaneous response to the magnetic field of FOMT material, could become a significant problem since the operation frequencies usually adopted by magnetic refrigerators are in [0.5÷10] Hz range, where the delay in materials' answer could assume significant values.
- A substantial hysteresis has generally been detected (Aprea et al, 2011a, 2011b) in FOMT materials, whereas it is very low in SOMTs. The consequences of hysteresis when analyzing the MCE are: i) history dependence: parameters such as magnetization and heat capacity now become non-single valued functions of temperature and field; ii) energy dissipation: heat is dissipated during the magnetization process, and the dissipation adds heat to the system.
- The large volume variation that one can observe in FOMT materials is another defect that must be considered when deciding to employ these materials.

I.2 Thermodynamical cycles for magnetic refrigeration

Magnetic refrigerator completes cooling/refrigeration by magnetic material through magnetic refrigeration cycle. In general, a magnetic refrigeration cycle consists of magnetization and demagnetization in which

heat is expelled and absorbed respectively, and two other benign middle processes.

The basic cycles for magnetic refrigeration are magnetic Carnot cycle, magnetic Stirling cycle, magnetic Ericsson cycle and magnetic Brayton cycle (Yu et al., 2003; Kitanovski and Egolf, 2006,). Among them, the magnetic Ericsson and Brayton cycles are applicable for room temperature magnetic refrigeration. The employment of a regenerator in the Ericsson and Brayton cycles lets the achievement of a large temperature span and easy operating.

I.2.1 Magnetic Ericsson cycle

Ericsson cycle consists of two isothermal processes/ stages and two isofield processes as illustrated in figures I.13(a) and I.13(b).

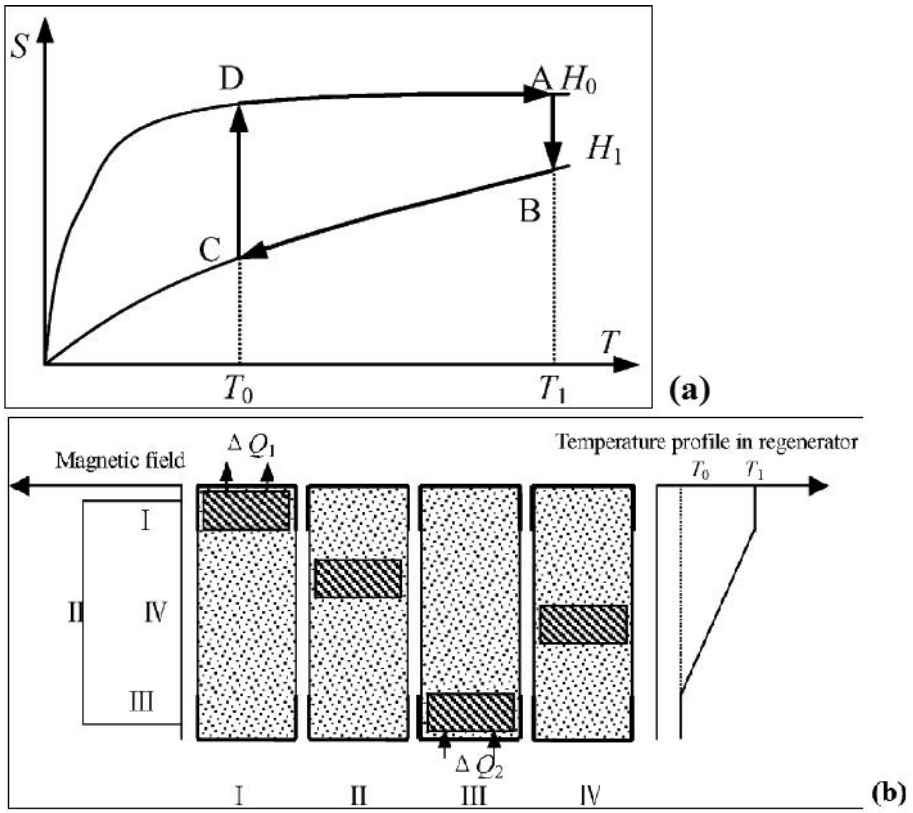

Figure I.13 *(a) The four processes of magnetic Ericsson cycle in T-S diagram. (b) Principle of magnetic Ericsson cycle refrigerator.*

1. In the isothermal magnetization process I(A→B in Fig. I.13(a)), when magnetic field increases from H_0 to H_1 the heat transferred from magnetic refrigerant to the upper regenerator fluid

$$Q_{ab} = T_1(S_a - S_b) \quad \text{(I.20)}$$

makes the latter increasing its temperature.

2. In the isofield cooling process II (B→C in Fig. I.13(a)), while magnetic field is kept constant at the maximum value H_1, both the refrigerant and the magnet which generates the field move downward to bottom and hence the heat

$$Q_{bc} = \int_{S_c}^{S_b} TdS \quad \text{(I.21)}$$

is transferred from magnetic refrigerant to regenerator fluid. Then a temperature gradient is set up in the regenerator.

3. In the isothermal demagnetization process III (C→D in Fig. I.13(a)), when magnetic field decreases from H_1 to H_0, the magnetic refrigerant absorbs heat:

$$Q_{ab} = T_0(S_d - S_c) \quad \text{(I.22)}$$

from the lower regenerator fluid. After that the fluid decreases its temperature.

4. In the isofield heating process IV (D→A in Fig. I.13(a)), while the magnetic field has kept constant at the minimum H_0, both the magnetic refrigerant and magnet move upward to the top and the regenerator fluid absorbs heat

$$Q_{da} = \int_{S_d}^{S_a} TdS \quad \text{(I.23)}$$

To make the Ericsson cycle possess the efficiency of magnetic Carnot cycle, it is required that the heat transferred in two isofield processes Q_{bc}, Q_{da} are equal. For an ideal Ericsson cycle, 'parallel' T–S curves are optimal, that is, ΔS_M keeps constant in the cooling temperature range.

I.2.2 Magnetic Brayton cycle

Magnetic Brayton cycle consists of two adiabatic processes and two isofield processes as shown in figure I.14.

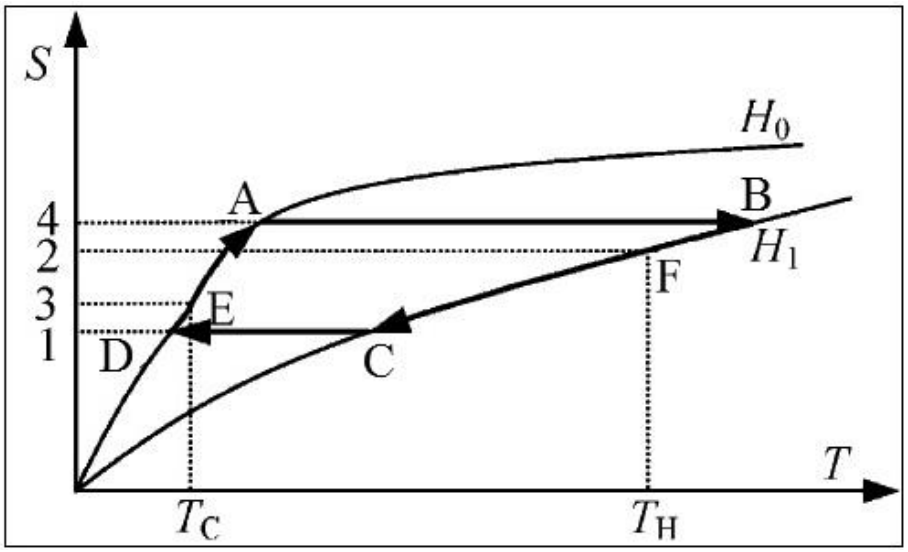

Figure I.14 *The four processes of magnetic Brayton cycle in S-T diagram.*

The first process (A→B in Fig. I.14) consists in and adiabatic magnetization, due to magnetic field increasing from H_0 to H_1, that leads to a temperature increment of $\Delta T_{ad,AB}$ in the solid refrigerant. With the field kept constant at H_1, in the isofield process (B→C in Fig. I.14) the heat of the area BC14 is transferred from the refrigerant to the hot heat exchanger at temperature T_H. In the adiabatic demagnetization (C→D in Fig. I.14) process the applied magnetic field falls from H_1 to H_0 and the solid refrigerant reduces its temperature of a quantity $\Delta T_{ad,CD}$ as a result of magnetocaloric effect. In the isofield process at H_0 the heat of the area AD14 is subtracted from the cold heat exchanger at T_C. No heat flows from and out of the magnetic refrigerant during the adiabatic magnetization and demagnetization processes.

The Brayton cycle can exhibit optimal performance as well with magnetic refrigerants having parallel T–S curves.

I.2.3 Magnetic Carnot cycle

The magnetic Carnot cycle, consists of two adiabatic and two isothermal processes, applied to a magnetic refrigerant, as shown in figure I.15.

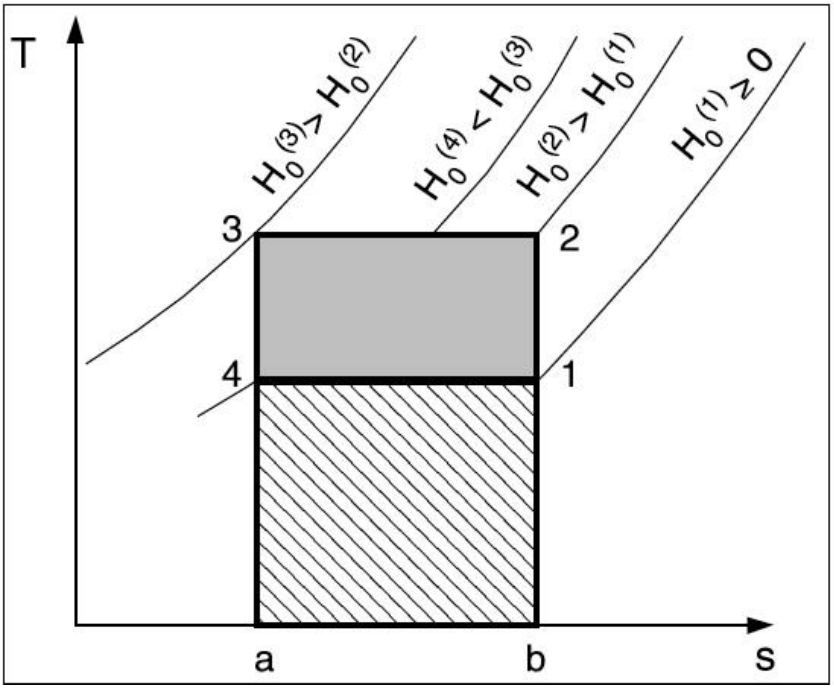

Figure I.15 *The four processes of magnetic Carnot cycle in S-T diagram.*

An adiabatic magnetization occurs in process 1→2 (figure I.15) and it continues with a further magnetization in stage 2→3, which is now an isothermal magnetization. During this process generated heat is extracted from the system. The next process step, namely 3→4, is an adiabatic demagnetization process. Connecting the system with a heat source leads to an isothermal demagnetization, resulting in process 4→1.

It becomes clear that the Carnot cycle can only be run, if a minimum of four different magnetic fields occur, through which the magnetocaloric material is moved. In the vertical process 1→2 the alteration of the magnetic field has to be applied quickly, not allowing heat to diffuse away or be transported out by convection. In 2→3 the isothermal magnetization requires an alteration of the magnetic field and simultaneous rejection of heat. This process will therefore be slower. The area between (1–2–3–4) represents the work required and the area (1–4–a–b) is related to the thermal cooling energy.

I.3 Cascade systems regenerators

All the cycles previously discussed are ideal cycles. At present the existing magnetocaloric materials could do not show sufficiently wide temperature differences for some frequently occurring refrigeration and heat pump applications. A solution to this problem is to build magnetic

refrigerators and heat pumps, which take advantage of cascades. However, both—the regeneration and the cascade systems—show additional irreversibility in their cycles. These leads to lower coefficients of performance.

Cascade systems are well known from conventional refrigeration technology. A cascade system is a serial connection of some refrigeration apparatuses. They may be packed into one housing to give the impression of having only a single unit. Each of these apparatuses has a different working domain and temperature range of operation. This can be seen in Fig. I.16(a) by the decreasing temperature domains of stages I– III. In this figure the cooling energy of stage I (surface: ef14) is applied for the heat rejection of stage II (surface cd23). Analogously, the cooling energy of stage II (surface cd14) is responsible for the heat rejection in stage III. The cooling energy of the entire cascade system is represented by the surface ab14 of the last stage (white domain). The total work performed in the total cascade system is given by the sum of the areas 1234 of all present stages I, II, and III.

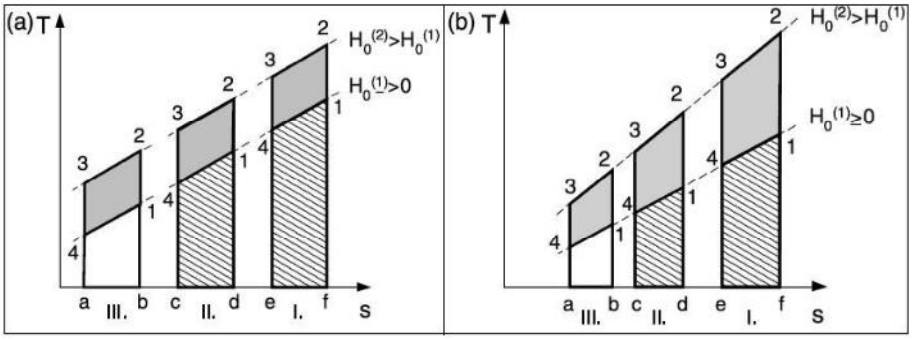

Figure I.16 *Two cascade systems based on the Brayton cycle. In case (a) all stages (I, II and III) are designed to have a different optimally adapted material, whereas in case (b) they are produced with the same material.*

The magnetocaloric effect is maximal at the Curie temperature. It is large only in the temperature interval around this temperature, with decreasing effect in the case of greater (temperature) differences. It is therefore, advantageous that the operating point of the refrigeration plant and this temperature interval of optimal magnetocaloric effect coincide. If the temperature span of the refrigeration process is too wide, a decrease in efficiency occurs. A solution to this problem is to work with a cascade system, where each internal unit has its own optimally adapted working temperature. Each stage of a cascade system contains a different magnetocaloric material (Fig. I.16(a)) or it contains the same (Fig. I.16(b)).

The disadvantage of a cascade system is that the cycles of each stage must be designed to avoid overlaps, as shown in figure I.17. An overlap leads to a narrower temperature span and reduced efficiency.

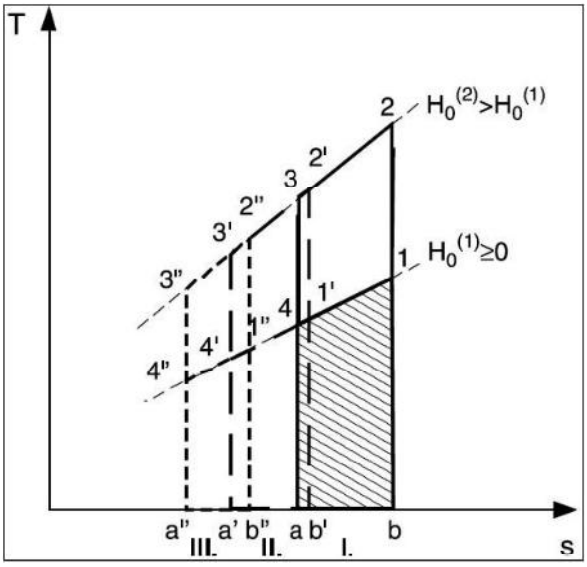

Figure I.17 *Overlaps in a cascade system lead to dissipation of energy and decrease the COP.*

A major advantage of a magnetic refrigeration cascade system over a conventional one is that in the magnetic refrigeration machine no heat exchangers are required between the cooling process of the higher stage and the heat rejection process of the lower stage. This is since the magnetocaloric material is solid and a single fluid may be transferred to both stages.

I.4 The regenerators

The introduction of regenerators in refrigeration systems, with reference to magnetic refrigeration, has the purpose to recover heat fluxes involved in Brayton cycle, that otherwise would have gone lost. The approach is particularly needed in room temperature magnetic refrigeration, where the vibrational entropy contribution becomes too high to be neglected. Therefore, a part of the magnetic refrigeration's cooling capacity is spent to cool the thermal load offered by the crystalline lattice, thus reducing the useful effect of the cycle. As a matter of fact, if a regenerator is added to the system, the heat rejected by the crystalline structure in one of the process of the cycle, is stored and then given back in the other process. By the way, the energy spent to cool the crystalline structure could be utilized effectively to increase of effective entropy change and temperature span (Yu et al., 2003).

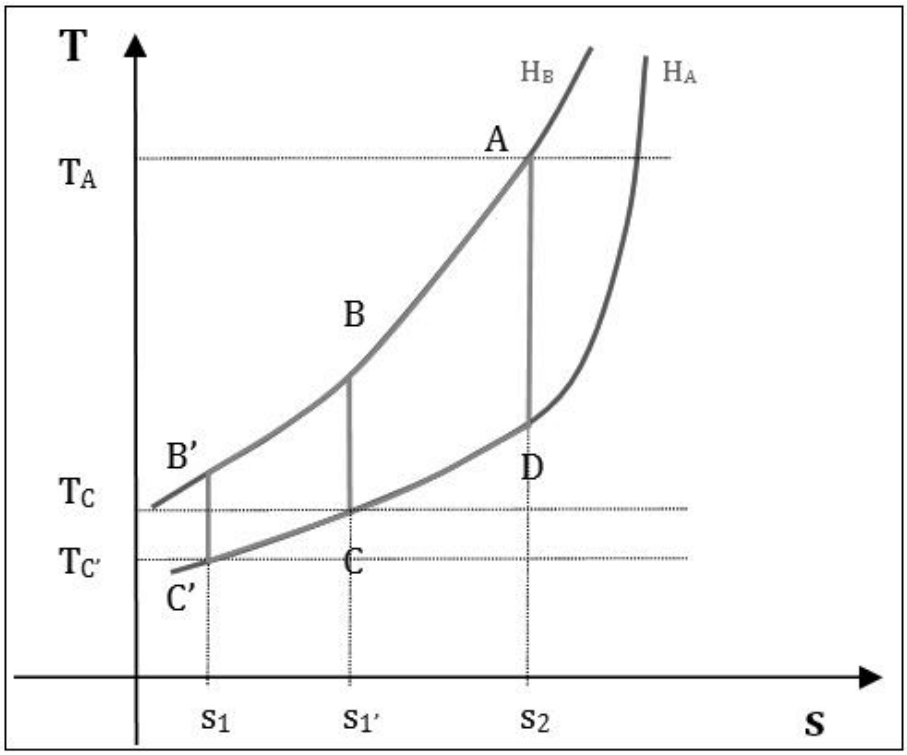

Figure I.18 *The regeneration effect in the Brayton cycle.*

In figure I.18 one can appreciate the effect of the regeneration in Brayton cycle: thanks to the thermal interchange is possible to reach a temperature range T_A-T_C 'greater than T_A-T_C, that would occur without regeneration, and a higher entropy change.

It is useful underlining the characteristics proper of the different typologies of regenerator. There are three types of regenerators employable in magnetic refrigerators:

a) external,
b) internal,
c) active.

Heat transferring through external regenerator between the regenerator material (which generally is solid-state) and the magnetic refrigerant is completed by an auxiliary heat transfer fluid.

With internal regenerator solution, the magnetic refrigerant is placed in regenerator together with the regenerator material and heat is transferred directly between themselves so that the regenerator should be in the magnetic field area.

If the regenerator is active, the magnetic material plays the double role of refrigerant and regenerator at the same time. It leads two advantages: both

the irreversibility losses, due to the auxiliary fluid, and the losses related to regenerating fluid mixing at different temperature are reduced. Thus the irreversible losses yielded by the second heat transferring in external regenerator or by mixing of the regenerator fluid with different temperature in internal regenerator, can be reduced.

The relative heat capacity between auxiliary fluid and magnetic refrigerant, plays a key role in choosing the best-fitting configuration of regenerator. If the heat capacity of the regenerator's fluid is higher than refrigerant magnetic material, it is better adopting an internal regenerator, where the temperature span in the regenerator is easily influenced by the fluid mixing. On the contrary case the best choice falls on active magnetic regenerator (AMR), where a high temperature span could be triggered and the requested fluid flow rate, on equal cooling power, is lower than the previous case.

There are several desirable characteristics for the perfect regenerator (Barclay, 1994):

- infinite thermal mass compared to the working material being cooled or heated;
- infinite heat transfer (a product of thermal conductance multiplied by the contact area) between working material and regenerator mass;
- zero void volume;
- zero pressure drop for convection of fluid through the regenerator;
- zero longitudinal conduction along the regenerator
- uniform, linear temperature gradient from the hot end to cold end of the unit.

The irreversible heat losses of the regenerator have a great influence on the performance of the whole magnetic refrigeration system. It has been analyzed the effect of thermal resistances and regenerative losses on the performance of magnetic Ericsson cycle qualitatively (Chen and Yan, 1998). Main irreversible heat losses are:

- loss of finite heat transfer between regenerator material and heat transfer fluid;
- loss of pressure drop yielded by flow resistance;
- thermal conduction along the magnetic material.
- loss of mixing of regenerator fluid in the internal regenerator;
- loss of heat leakage;
- losses of magnetic hysteresis and eddy currents;
- loss caused by viscous dissipation in the regenerator fluid;
- loss of ''dead volume''.

In an AMR, some amount of the heat transfer fluid is always in the connecting lines between the beds and the heat exchangers and never cycles

both through the beds and the heat exchangers. This trapped heat transfer fluid, commonly referred to as the ‘‘dead volume,’’ is a significant source of inefficiency in active magnetic regenerators (Lawton et al., 1999).

In figure I.19 are represented some typical structural configurations of AMR regenerators where:

a) parallel plate configuration;
b) perforated plate configuration;
c) grid configuration;
d) packed bed configuration.

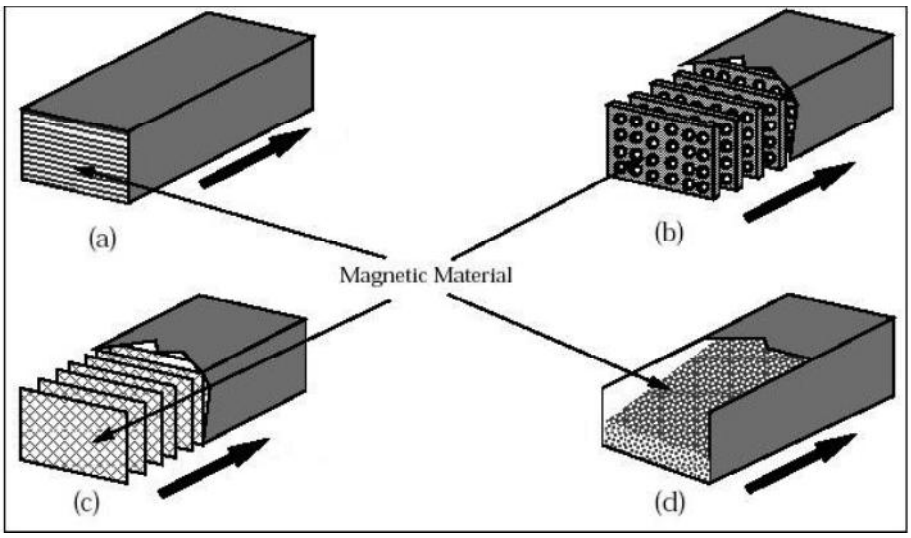

Figure I.19 *Typical AMR regenerator's configurations.*

I.5 Thermodynamical cycles employing active regenerators

I.5.1 Active Magnetic Regenerative refrigerant (AMR) cycle

Barclay firstly introduced the Active Magnetic Regenerative refrigeration cycle, well known as AMR, in 1982 (Barclay, 1982). The innovative idea leads to a new magnetic cycle, different from the previous ones (Carnot, Ericsson, Brayton, or Stirling). It is founded on a magnetic Brayton cycle as shown in Figure I.20.

The main innovation consists of introducing the AMR regenerator concept, i.e. the employment of the magnetic material both as refrigerant and regenerator. A secondary fluid is used to transfer heat from the cold to the hot end of the regenerator. Substantially every section of the regenerator experiments its own AMR cycle, according to the proper working temperature. Through an AMR one can appreciate a larger temperature span between the regenerator material and the auxiliary fluid.

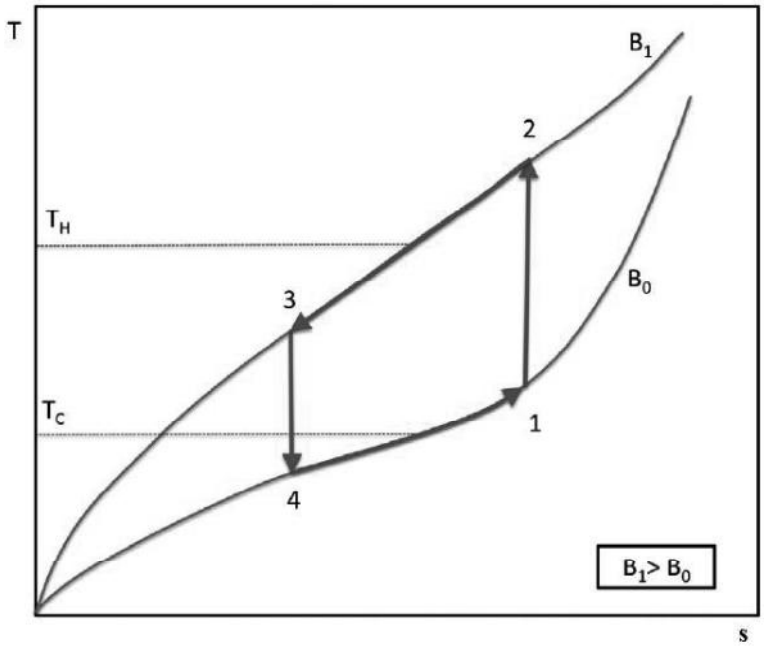

Figure I.20 *The four processes of AMR cycle in T-s diagram.*

During the entire cycle the magnetic field induction varies between a minimum value, B_0, and a maximum one, B_1. The regenerator works between a warm reservoir at T_H and a cold one at T_C. The AMR cycle consists of four processes. During the magnetization (1→2), the magnetic field is increased adiabatically with no fluid flow, causing the increase of the temperature of the magnetic material due to MCE, as displayed in figure I.21(a). In the cold-to-hot flow process (2→3), visible in figure I.21(b) the secondary fluid blows from the cold to the hot end of the regenerator when the field has kept constant at the maximum value. The fluid absorbs heat from the bed, reaching a temperature above T_H and rejects it through the warm heat exchanger. The next process, shown in figure I.21(c), is the adiabatic demagnetization (3→4) where, without any fluid flowing, the magnetic field is removed and the magnetic material temperature decreases because of the MCE. Finally, the heat transfer fluid flows through the bed from the hot to the cold end (4→1), as figure I.21(d) exhibits, with the applied magnetic field kept fixed at the minimum. The resulting hotter fluid cools the bed and reach a temperature lower than T_C. At this stage the secondary fluid absorbs heat from the cold heat exchanger producing a cooling load.

The AMR cycle described in this section has the peculiarity to employ a heat transfer fluid which has alternative motion. Other project solutions could take to slightly modifications of the cycle implementation.

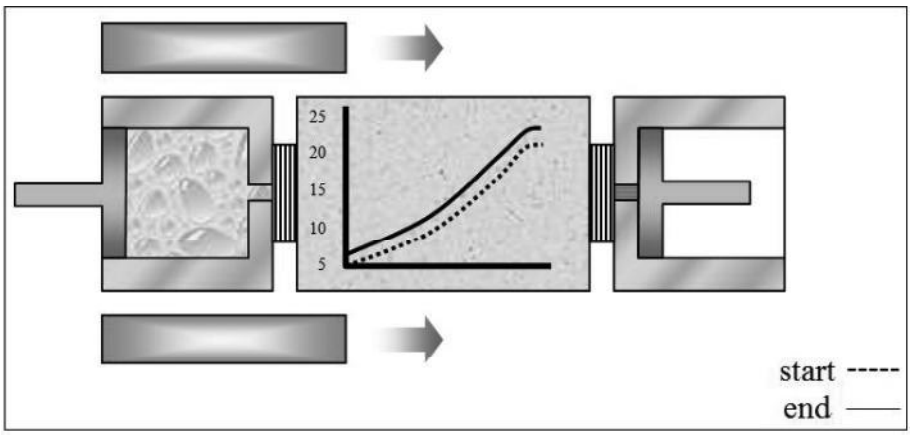

Figure I.21(a) *First process of AMR cycle: adiabatic magnetization.*

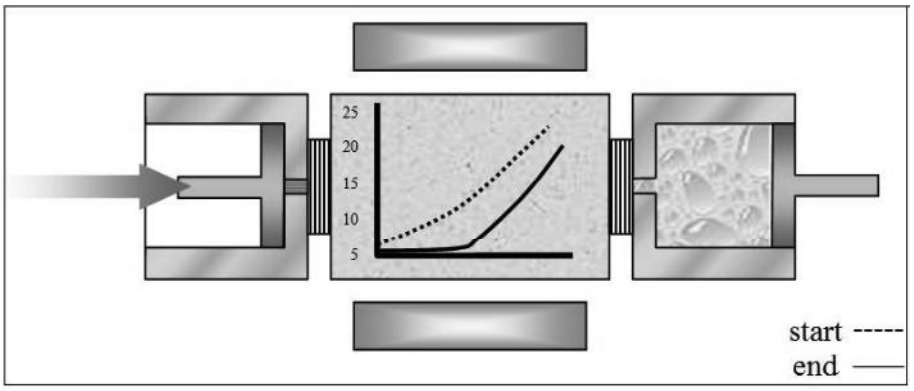

Figure I.21(b) *Second process of AMR cycle: cold-to-hot side fluid flowing.*

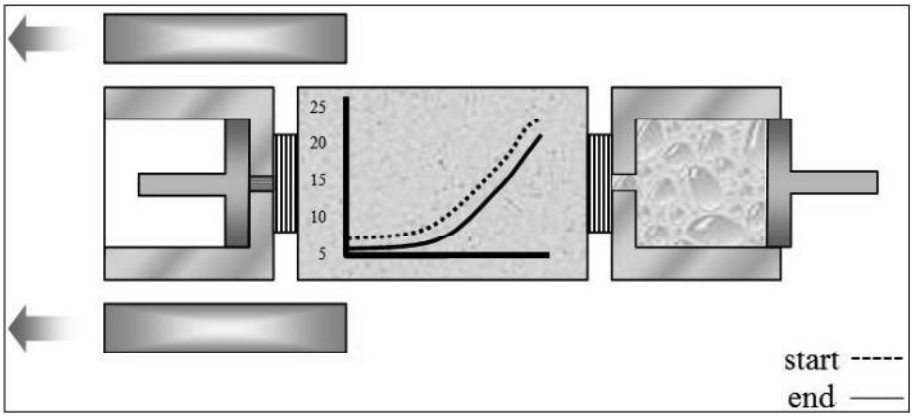

Figure I.21(c) *Third process of AMR cycle: adiabatic demagnetization.*

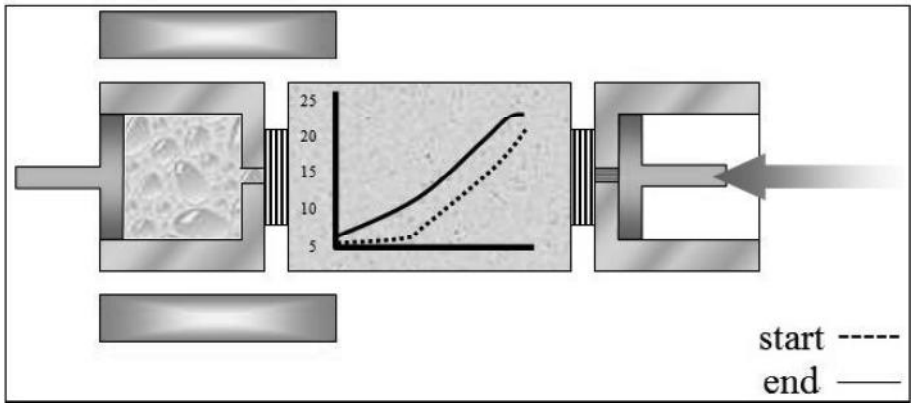

Figure I.21(d) *Fourth process of AMR cycle: hot-to-cold end fluid flowing.*

I.5.2 Active Magnetic Regenerative Rotary refrigerant (AMRR) cycle

At Astronautics Corporation of America, it has been introduced for the first time in 2001 (Zimm, 2003) a rotary AMR cycle, called Active Magnetic Regenerative Rotary refrigerant (AMRR) cycle. The cycle has been applied for a first time on an AMRR system (Zimm et al., 2006), where a wheel with multiple regenerators composed of a magnetocaloric material is kept in a relative rotating motion with a magnetic field generated by magnetic group, made of permanent magnets. The wheel is divided into six, separate active magnetic regenerator (AMR) beds. The beds are subjected to an oscillating flow of heat transfer fluid that is correctly phased relative to the position of the bed in the magnetic field. Fluid flow is provided by a single pump and fluid, exiting a bed during a cold-to-hot flow process, crosses the bed at an elevated temperature, is cooled to the hot reservoir temperature, and is sent into a bed that is experiencing hot-to-cold flow. The flow setup is analogous for fluid exiting and entering the cold side of the regenerator beds. This flow configuration is enabled by a sophisticated valve system; each bed contains its own fluid manifold system that passes under a distribution and recovery point at specific angular location.

The rotary regenerator considered in this section, useful to describe the AMRR cycle, is a ring that contains a number of regenerator beds which are aligned back-to-back (i.e. the cold and hot ends of adjacent beds are adjacent). Flow through the bed is in the tangential direction. The regenerator beds spin at constant angular velocity ω through a magnetic group that covers a specified arc over the regenerator bed. In figures 1.22(a), (b), (c) and (d) are described the four processed of the AMRR cycle, following the “A” regenerator.

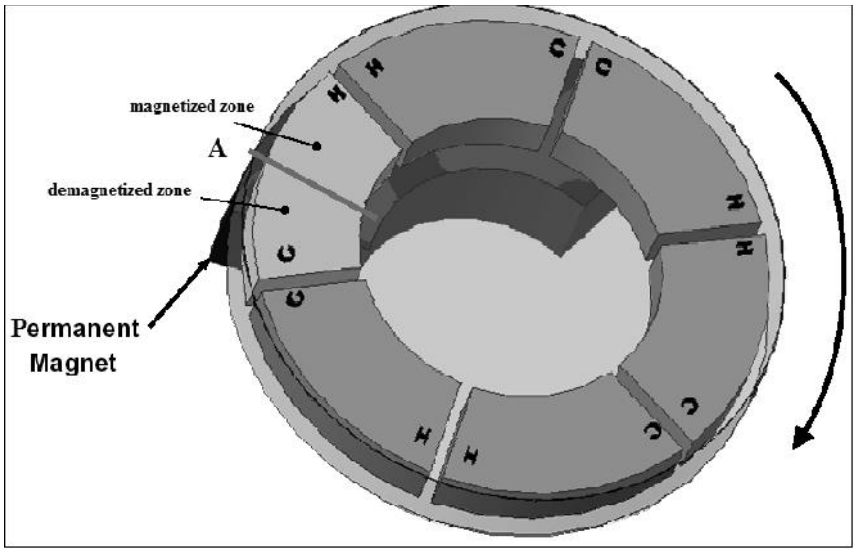

Figure I.22(a) *First process of AMRR cycle with respect to the "A" regenerator: adiabatic magnetization.*

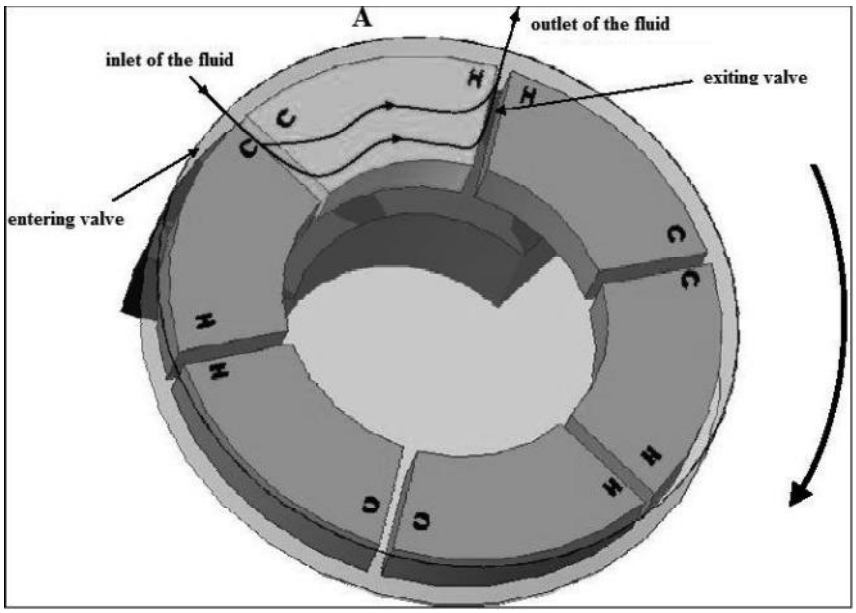

Figure I.22(b) *Second process of AMRR cycle with respect to the "A" regenerator: cold-to-hot flow.*

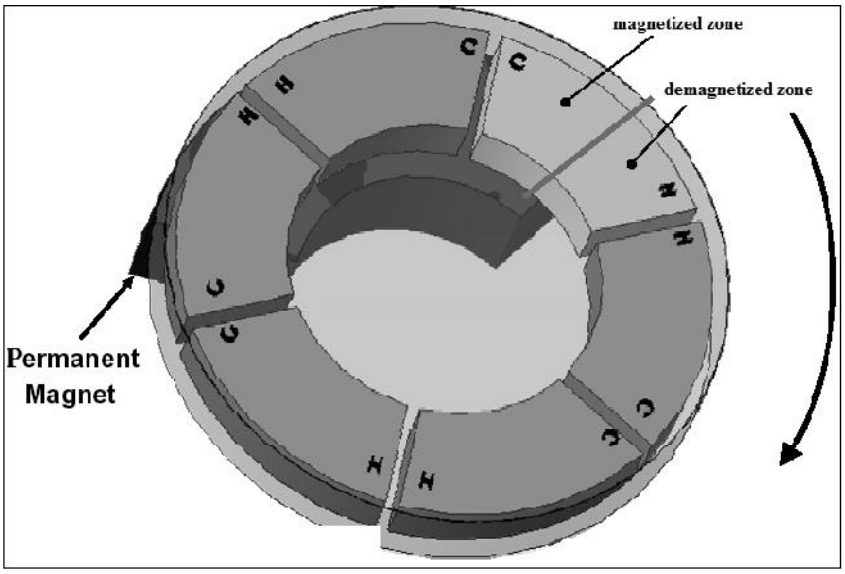

Figure I.22(c) *Third process of AMRR cycle with respect to the "A" regenerator: adiabatic demagnetization.*

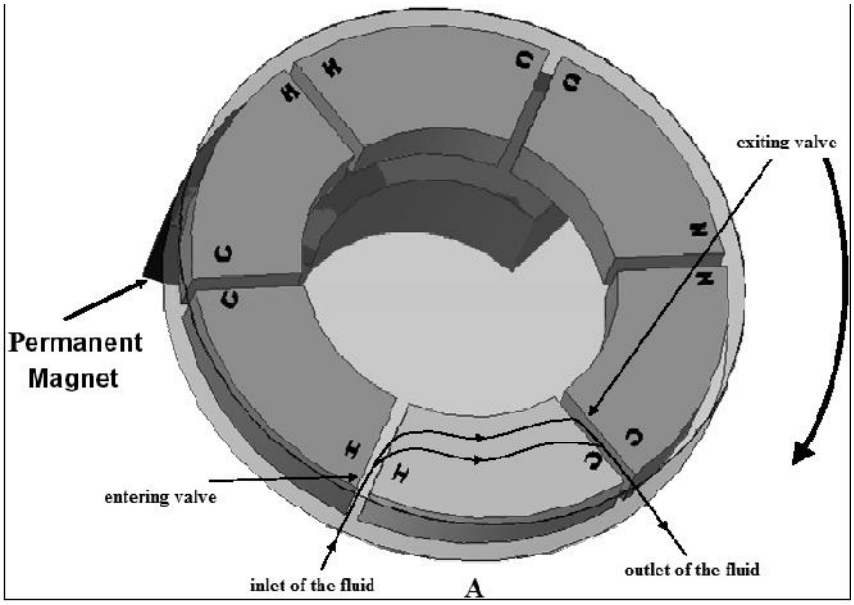

Figure I.22(d) *Fourth process of AMRR cycle with respect to the "A" regenerator: hot-to-cold flow.*

In the A regenerator, in the first process, the hot end of the regenerator enters the magnetic field and therefore the bed is magnetized from the hot to the cold end, as shown in figure 1.22(a). The cold and the hot sides of each regenerator is labeled with C or H, respectively. Flow from cold to hot end

of “A” regenerator is assumed to occur while the entire bed is inside the magnetic field, as figure 1.22(b) exhibits. The demagnetization process causes the A regenerator’s temperature decrease and there is no fluid flow during this process, as shown in figure 1.22(c). Flow from the hot end to cold end is assumed to occur while the entire bed is outside the magnetic field, as visible in figure 1.22(d).

I.6 Magnetocaloric materials

Since Brown first applied ferromagnetic material gadolinium (Gd) in the room temperature magnetic refrigerator in 1976 (Brown, 1976), the research field of magnetic refrigeration working materials has been greatly expanded. At first, some ferromagnets concerning the second order transition were investigated for the large MCE existing in them. Recently the magnetic materials undergoing a first-order magnetic transition become the focus after the giant MCE was discovered in GdSiGe alloys. Nowadays a huge part of researchers is orienting its attention on some new alloys of magnetocaloric materials: as a result, many new materials with large MCEs (and many with lesser values) have been discovered, and a much better understanding of this magneto-thermal property has resulted. A number of new magnetocaloric substances with substantial cooling capacity have been discovered: the lanthanide aluminides; the La manganites, some of which have MCEs comparable to Gd between 220 and 290 K; the tunable giant MCE for room temperature range. The latter two along with the well-established Gd offers considerable promise that practical near room–temperature magnetic refrigeration/cooling is just around the corner.

I.6.1 The criteria for selecting magnetocaloric refrigerant

In terms of the theoretical analyses and the magnetocaloric nature of existing materials, the criteria for selecting magnetic refrigerants for active magnetic refrigerators are given as follows (Phana and Yub, 2007; Aprea et al. 2015b):

- the large magnetic entropy change and the large adiabatic temperature change (i.e., the large MCE) at moderate magnetic field;
- the large density of magnetic entropy (it is an important factor contributing to the working efficiency of materials);
- the small lattice entropy;
- nearly zero magnetic hysteresis (it is related to the working efficiency of a magnetic refrigerant material);
- very small thermal hysteresis (this is related to the reversibility of the MCE of a magnetic refrigerant material);

- small specific heat and large thermal conductivity (these ensure remarkable temperature change and rapid heat exchange);
- large electric resistance (i.e., the lowering eddy current heating or the small eddy current loss);
- high chemical stability and simple sample synthesis route are also required for magnetic refrigerant materials;
- no toxic or too expensive elements;
- corrosion resistance material;
- limited number of elements in the compound in order to facilitate the control of reproducibility;
- synthesis process compatible with large-scale production;
- instantaneous MCE corresponding to a magnetic field variation;
- small volume variation.

I.6.2 Magnetic cooling efficiency

The magnetic cooling efficiency of a magnetocaloric material can be, in simple cases, evaluated by considering the magnitude of ΔS_M or ΔT_{ad} and its full-width at half-maximum (δT_{FWHM}) (Phana and Yub, 2007).

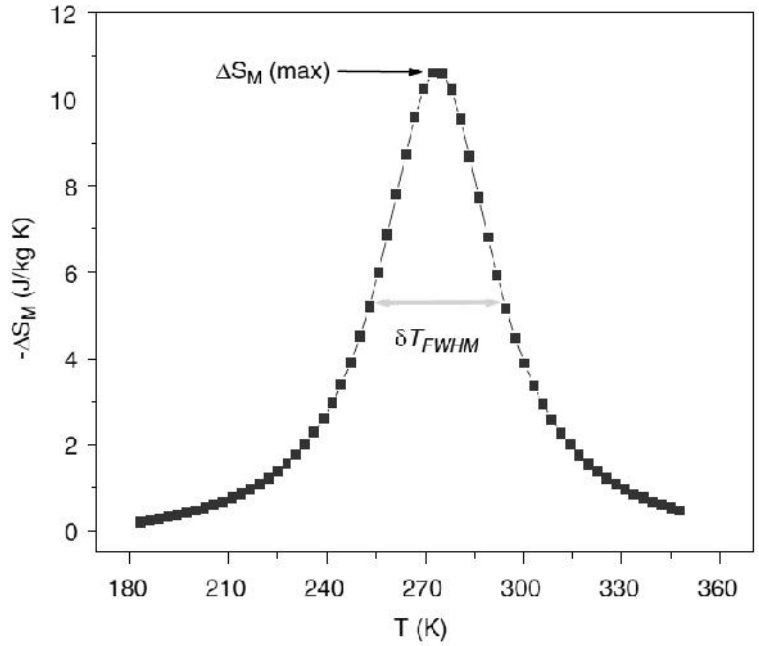

Figure I.23 *An example of the evaluation of relative cooling power based on the temperature dependence of magnetic entropy change, RCP(S).*

It is possible to define the product of the ΔS_M maximum and the full-width at half-maximum:

$$\delta T_{FWHM} = T_2 - T_1 \quad \text{(I.24)}$$

as

$$RCP(S) = -\Delta S_M(T,H) \times \delta T_{FWHM} \quad \text{(I.25)}$$

which stands for the so-called relative cooling power (RCP) based on the magnetic entropy change. An example is reported in figure I.23.

Similarly, the product of the maximum adiabatic temperature change ΔT_{ad} and the full-width at half-maximum δT_{FWHM} is expressed by

$$RCP(T) = \Delta T_{ad}(T,H) \times \delta T_{FWHM} \quad \text{(I.26)}$$

which stands for the so-called RCP based on the adiabatic temperature change.

I.6.3 Classification of magnetocaloric materials

Some promising magnetic materials employable as candidates for magnetic refrigeration in the future are described later.

I.6.3.1 Crystalline materials containing Rare Earth Metals: Gd and its alloys

The most employed material for the refrigeration at room temperature is gadolinium, a rare-earth metal which exhibits a second order paramagnetic to ferromagnetic transition at its Curie temperature (T_c = 294 K) which exhibits excellent magnetocaloric properties. Gadolinium (Gd) is the only rare earth which orders magnetically near room temperature and is often considered to be a simple Heisenberg ferromagnet, i.e., a representative classical ferromagnet. The paramagnetic to ferromagnetic phase transition is a second-order phase transformation.

There are several reasons why Gd is considered a benchmark materials for magnetic cooling applications: since Gd is considered a classical ferromagnet and it orders near room temperature, it is quite easy to carry out experiments to gain a better understanding of the nature of the paramagnetic to ferromagnetic phase transformation. Second, this transformation has a potentially large practical importance, specifically with regard to magnetic cooling and heating near room temperature. Figures I.24, I.25 and I.26 report, respectively, the curves of $-\Delta S_M(H,T)$, $\Delta T_{ad}(H,T)$, $C_P(H,T)$, with respect to temperature (Griffel et al., 1954; Dan'kov et al. 1998).

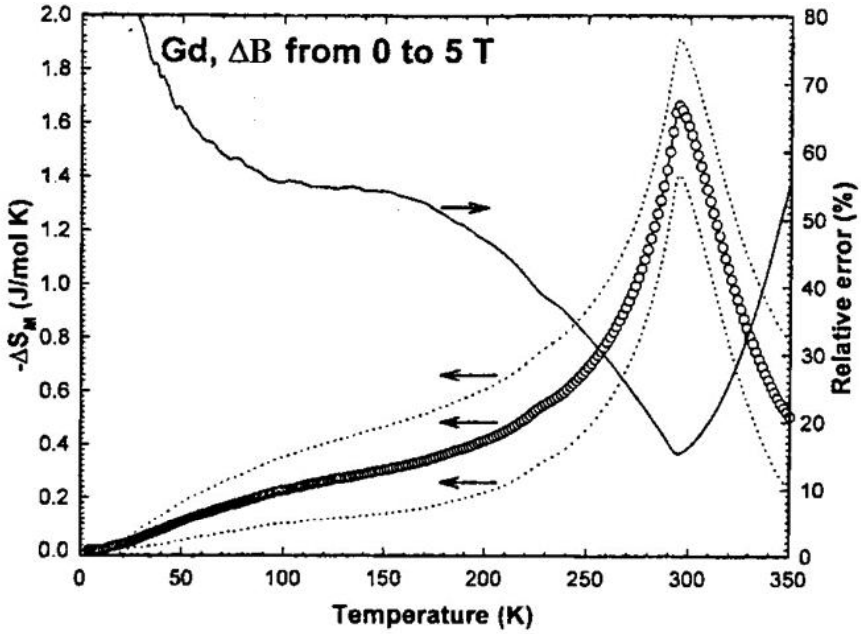

Figure I.24 *$-\Delta S_M$ (T) of single crystal of gadolinium parameterized for various magnetic field induction.*

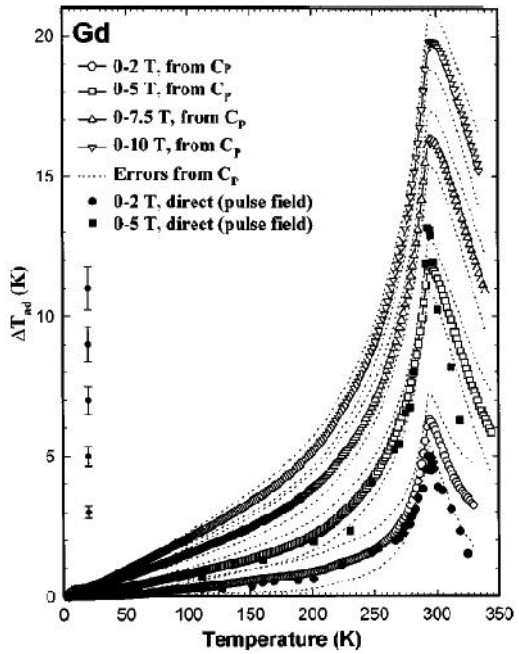

Figure I.25 *ΔT_{ad} (T) of single crystal of gadolinium measured under different values of magnetic field induction.*

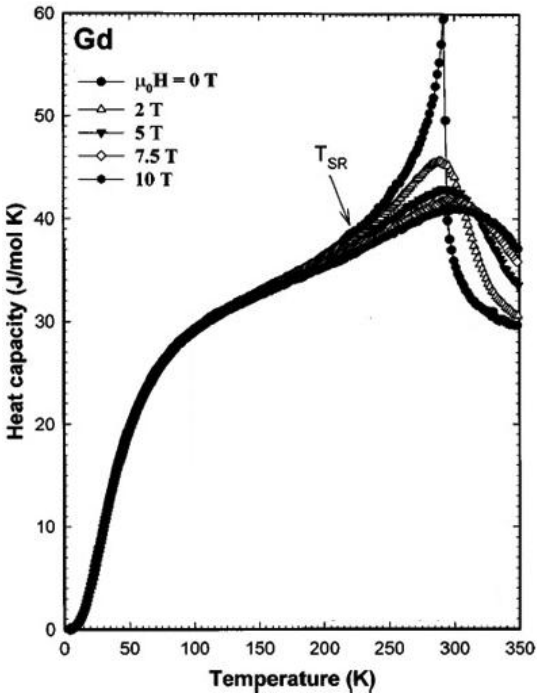

Figure I.26 *Heat capacity of single-crystal of gadolinium measured under different magnetic field induction.*

The heat capacity is a useful tool for studying magnetic phase transitions in the lanthanide metals and their compounds. Theoretical and experimental investigations of the heat-capacity behavior of some Gd-based compounds can be found in the literature (Blanco et al., 1991; Bouvier et al., 1991; Dan'kov et al. 1998). Usually the heat capacity at constant pressure $C_P(T)$ behaves abnormally near the temperature where magnetic phase transitions occur. Hence, the behavior of $C_P(H,T)$ as a function of temperature and magnetic field can be used to examine the nature of the magnetic phase transition.

In figure I.27 is reported $\Delta T_{ad}(H,T)$ of gadolinium measured under a magnetic field induction which varies between 0÷2 T, under both adiabatic magnetization and demagnetization (Aprea and Maiorino, 2010). It is clearly visible that even if they are located around T_C, the temperature where $\Delta T_{ad}(H,T)$ is maximum are slightly different. This is due to a different behavior of the gadolinium magnetization near the Curie temperature, with respect to the magnetic field induction considered, as appreciable in figure I.28. Therefore deriving the function M(B,T), two different functions have been obtained for $\Delta T_{ad}(H,T)$ (equation I.16). Moreover both two other different functions have been founded for $\Delta S_M(H,T)$ through equation I.15.

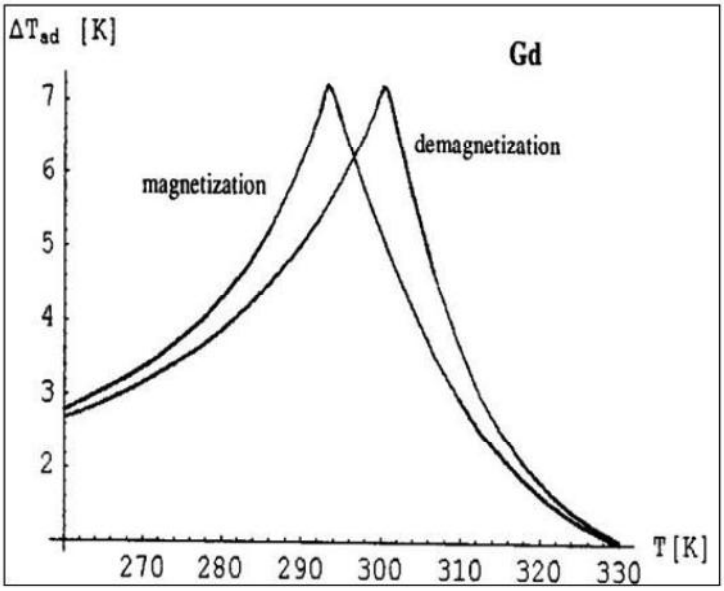

Figure I.27 *ΔT_{ad} (H,T) of in single crystal of gadolinium measured, during adiabatic magnetization and demagnetization, under a magnetic field induction which varies in 0÷1.5 T.*

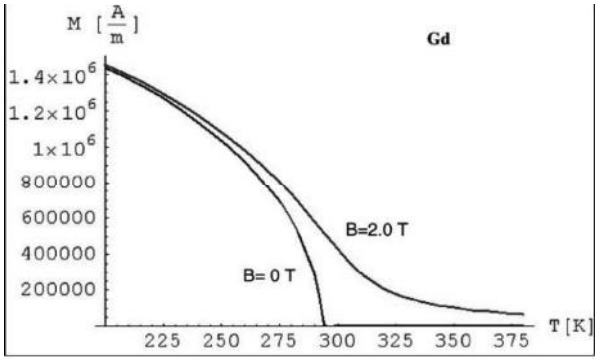

Figure I.28 *M (B,T) of in single crystal of gadolinium.*

In a study of the magnetic properties of Gd-based materials with Curie temperatures between 250 and 350 K, Pecharsky and Gschneidner, Jr. (Pecharsky and Gschneidner Jr., 1997) in 1997 have discovered an extraordinarily large magnetocaloric effect in $Gd_5(Si_2Ge_2)$.

Gd_5Si_4 orders ferromagnetically at 335 K. The related phase Gd_5Ge_4, orders antiferromagnetically at much lower temperature. When Ge substitutes for Si in $Gd_5(SiGe)_4$, the Curie temperature is lowered from 335 to 295 K at the $Gd_5(Si_2Ge_2)$ composition. Further substitution of Ge for Si induces the appearance of a then unidentified intermediate phase and the

beginning of a sharp decrease in the ordering temperature when the Si:Ge ratio is further reduced (Holtzberg et al., 1967). Experimental studies (Pecharsky and Gschneidner Jr., 1997) confirm that the extended solid solution $Gd_5(Si_xGe_{1-x})_4$ exists for $1 \leq x < 0.5$ and that the Curie temperature of Gd_5Si_4 is gradually lowered from 335 to 300 K near the $Gd_5(Si_2Ge_2)$ composition. $Gd_5(Si_xGe_{1-x})_4$ compounds (where $1 \leq x < 0.5$) are among the most promising compounds for magnetic refrigeration. Alloys of gadolinium, silicon and germanium, $Gd_5(Si_xGe_{1-x})_4$ show a First Order Magnetic Transition (FOMT) characterized by a peak of ΔT_{ad} and ΔS_M much greater than gadolinium ones, but the whole function is quite sharper in $Gd_5(Si_xGe_{1-x})_4$ alloys. In particular, $Gd_5(Si_2Ge_2)$, which exhibits the larger MCE among $Gd_5(Si_xGe_{1-x})_4$ compounds and which is named GIANT magnetocaloric effect, presents two different phase transitions. At 276 K one can observe in $Gd_5(Si_2Ge_2)$ a FOMT which constitute the MCE highest temperature peak, whereas at 299 K it is possible to appreciate a Second Order Magnetic Transition (SOMT) where, according to it, the material orders paramagnetically. Nevertheless $Gd5(Si_2Ge_2)$ shows a moderate hysteresis of 2 K (von Moos et al., 2015).

Figures I.29 and I.30 report, respectively, the curves of $-\Delta S_M(H,T)$, $\Delta T_{ad}(H,T)$, with respect to temperature and under various magnetic field inductions (Pecharsky and Gschneidner Jr., 1997). The adiabatic temperature rise for $Gd_5(Si_2Ge_2)$ is quite sharp and extends over a narrow temperature range, just as the ΔS_M. The ΔT_{ad} values of $Gd_5(Si_2Ge_2)$ are larger than the corresponding ΔT_{ad} values for Gd $\geq$ 30%, by comparing the peak values, regardless of the temperature. The magnetic field dependencies of the heat capacities $C_P(H,T)$ of $Gd_5(Si_2Ge_2)$ compared with Gd are shown in figure I.31(a) and I.31(b), respectively. Furthermore, the inset of figure I.31(a) contains the curves of total entropy S(T) of $Gd_5(Si_2Ge_2)$, parameterized for a number of magnetic field inductions. One notices a significant difference in the influence of the magnetic field on the heat capacity of the two materials. For $Gd_5(Si_2Ge_2)$ the low temperature heat capacity peak is quite sharp and it essentially retains the same shape, whereas the peak height falls off and the peak temperature increases more-or-less in a linear fashion with increasing field. In contrast, for Gd the peak is reduced in height by low magnetic fields, becomes rounded off, and is spread out over a wide temperature with increasing field.

This difference is because for $Gd_5(Si_2Ge_2)$ the lower temperature and dominant magnetic ordering [ferromagnetic (I) → ferromagnetic (II)] is a first order phase transformation, while for Gd it is a second order transformation. The field dependence of $Gd_5(Si_2Ge_2)$ entropy, which is shown in the inset of figure I.31(a) indicates that the S(T) discontinuity is shifted to higher temperature by increasing magnetic field and that the

transition remains thermodynamically a first order phase transformation in magnetic fields as high as 7.5 T (and, maybe, even 10 T).

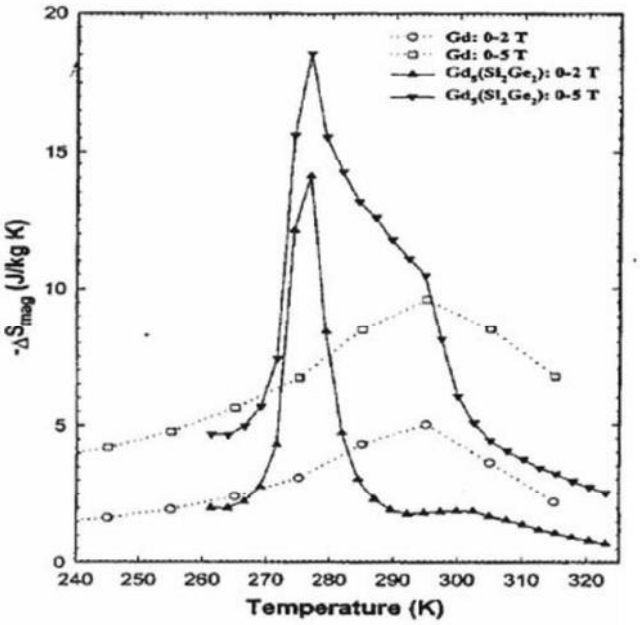

Figure I.29 *$-\Delta S_M$ (H,T) of $Gd_5(Si_2Ge_2)$ parameterized for different magnetic field induction and compared with gadolinium.*

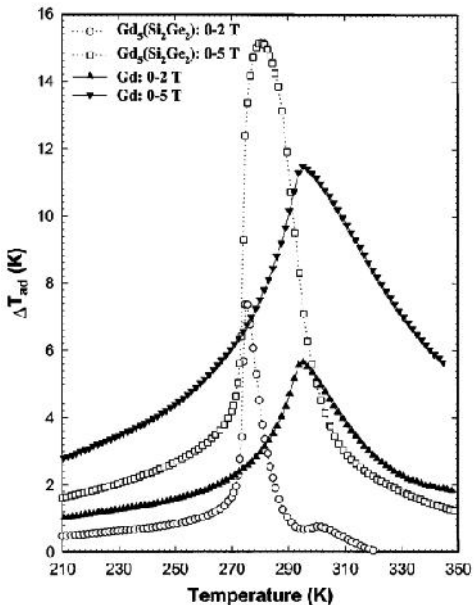

Figure I.30 *ΔT_{ad} (H,T) of $Gd_5(Si_2Ge_2)$, in comparison with Gd, for magnetic field inductions which change from 0 to 2 and from 0 to 5 T.*

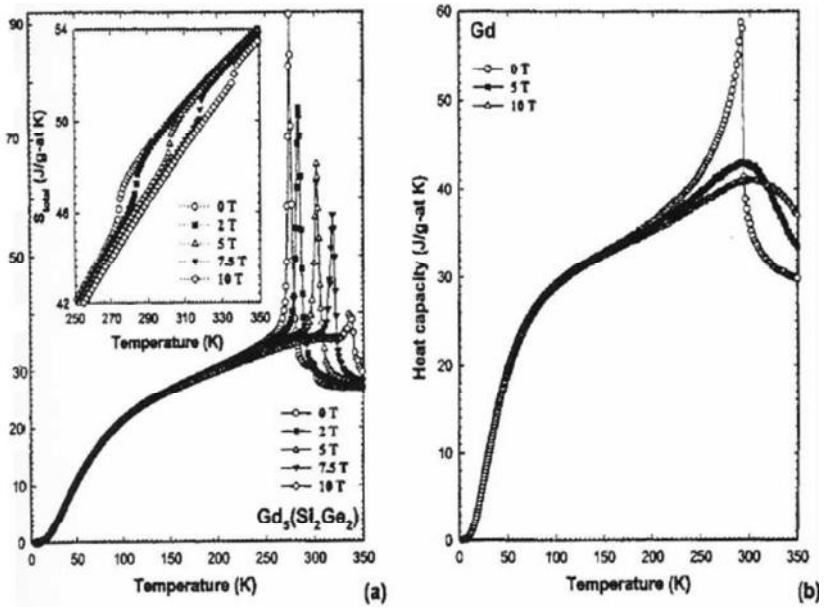

Figure I.31 *The heat capacity of $Gd_5(Si_2Ge_2)$ as a function of temperature and magnetic field (a) in comparison with that of pure Gd (b). The inset in (a) shows total entropy of $Gd_5(Si_2Ge_2)$ as a function of temperature and magnetic field, as determined from the heat capacity.*

I.6.3.2 Crystalline materials containing Rare Earth Metals: $La[Fe(Si,Al)]_{13}$ compounds

The La-Fe binary phase diagram shows an immiscible system, in which no intermetallic compounds form. The addition of small amount of Si or Al allows the formation of a ferromagnetic face-centred-cubic structure; this intermetallic compound exhibits very interesting magnetic behaviour with GMCE for $LaFe_{11.4}Si_{1.6}$ (ΔS_M close to 20 J $kg^{-1}K^{-1}$ at 210 K, for H = 5 T) (Hu et al., 2001). This was ascribed to a first-order itinerant electron metamagnetic transition, where a volume change of approximately 1% does not change the crystal symmetry. The itinerant electron metamagnetic transition can be lost due to compositional effects, leading to SOMT, which reduces MCE but implies negligible hysteresis losses.

Tuning the temperature transition either by changing the Fe/Si ratio or substituting a different Rare Earth metal for La yielded an almost linear relationship between S_M and T_C. Moreover, the FOMT changed to a SOMT as temperature increased. A more efficient way to shift Curie temperature to higher temperatures, however, is by partial Co substitution for Fe, as the magnetic moment of Fe is not seriously affected by Co substitution, but for

$LaFe_{13-x}Si_x$ the average magnetic moment of Fe atoms decreases 0.286 μB per Si atom. Hydrides (H^-) are also known to shift the temperature of the FOMT to higher values, without diminishing $|\Delta S_M|$ values, and with an enhancement of ΔT_{ad} as the heat capacity remains almost unchanged. However, hydrides in this compound are unstable above 423 K.

Single-phase $La(Fe,Si)_{13}$ alloys are very difficult to obtain and generally contain impurities, even after prolonged annealing at high temperature. These impurities must be factored into any comparison of different results, as composition can be inhomogeneous, and thus multiphase, rather than single-phase, behaviour should be expected. The use of Al instead of Si to stabilize the face-centred-cubic structure is less effective with respect to MCE (Franco et al., 2012).

Two interesting compounds among $La(Fe,Si)_{13}$ alloys for magnetic refrigeration at room temperature are: $LaFe_{11.384}Mn_{0.356}Si_{1.26}H_{1.52}$ (Morrison et al., 2012), which has a first order magnetic phase transition at 290 K, and $LaFe_{13-x-y}Co_xSi_y$ (Bjørk et al., 2010a), where the chemical composition of these are $LaFe_{11.06}Co_{0.86}Si_{1.08}$, $LaFe_{11.05}Co_{0.94}Si_{1.01}$ and $LaFe_{10.96}Co_{0.97}Si_{1.07}$, in order to varying the Curie temperature in 275.8÷289.8 K.

In figure I.32 and I.33 are reported $LaFe_{11.384}Mn_{0.356}Si_{1.26}H_{1.52}$ $\Delta S_M(H,T)$ (under a magnetic field induction of B = 1.2T) and $\Delta T_{ad}(H,T)$ a field change of 0.4, 0.8, and 1.2 T where the starting field value was zero.

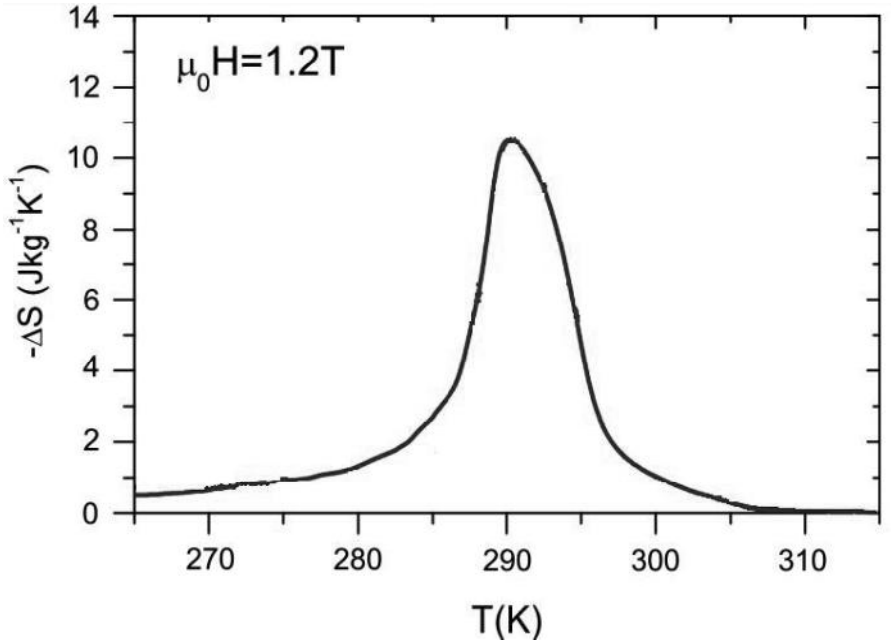

Figure I.32 -ΔS_M (H,T) of $LaFe_{11.384}Mn_{0.356}Si_{1.26}H_{1.52}$ under 1.2T as magnetic field induction.

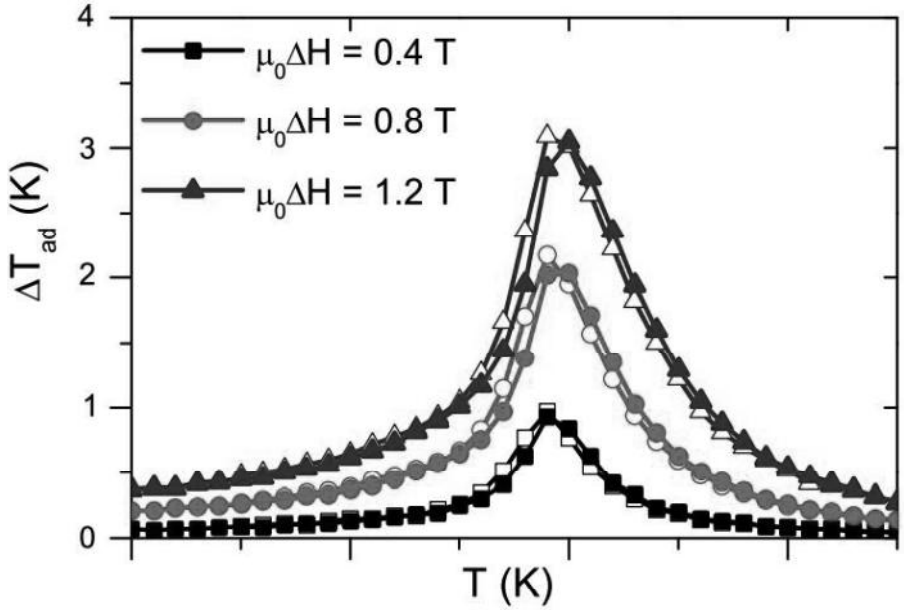

Figure I.33 *ΔT_{ad} (H,T) of $LaFe_{11.384}Mn_{0.356}Si_{1.26}H_{1.52}$, for magnetic field inductions which change from 0 to 0.4 T, 0.8T and 1.2 T.*

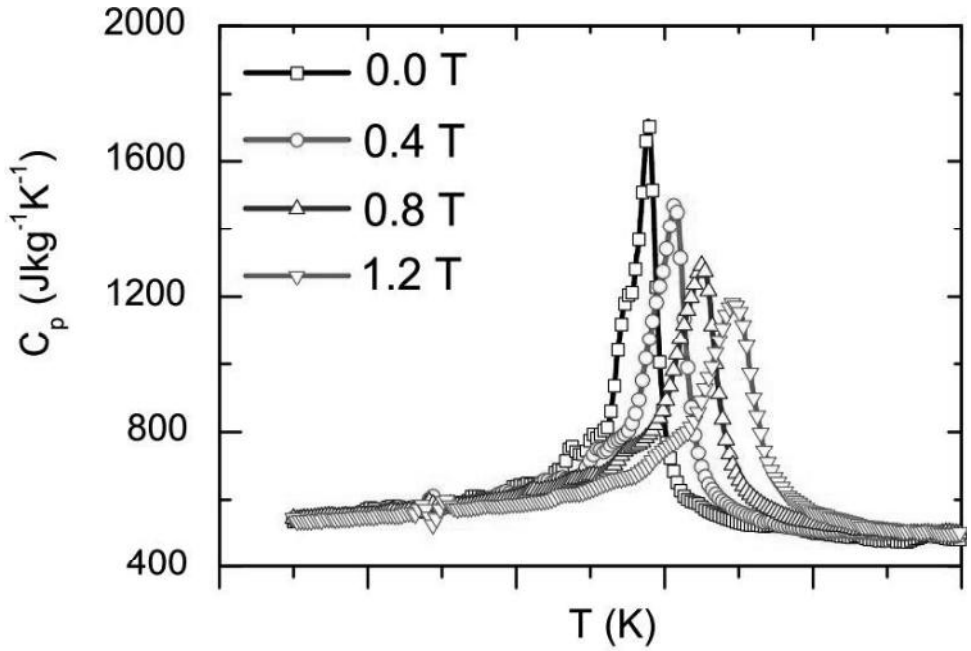

Figure I.34 *The heat capacity of $LaFe_{11.384}Mn_{0.356}Si_{1.26}H_{1.52}$ as a function of temperature and for different magnetic field change.*

Figure I.34 exhibits heat capacity of $LaFe_{11.384}Mn_{0.356}Si_{1.26}H_{1.52}$. One can notice the peak's right-moving, together with magnetic field increasing, whereas the absolute value of the maximum is falling.

The properties of the LaFeCoSi samples are compared with the properties of commercial grade gadolinium, here simply termed Gd. This gadolinium is much cheaper than pure gadolinium, but the purity is also lower. The commercial grade gadolinium contains 99.5% rare earth metal, of which 99.94% are gadolinium. In figure I.35 are shown $\Delta S_M(H,T)$ of the above mentioned LaFeCoSi samples, under a magnetic field whose induction varies in the 0÷1 T range. The peak temperature increases together with x, whereas the highest absolute value of $\Delta S_M(K)$ is registered for $LaFe_{11.06}Co_{0.86}Si_{1.08}$ at its Curie temperature (275.8 K). Figure I.36 displays $\Delta T_{ad}(H,T)$ of LaFeCoSi alloys, under 1T as magnetic field induction, which starts from a zero value. The transition temperatures are 277.1 K, 287.1 K, 289.6 K, respectively for $LaFe_{11.06}Co_{0.86}Si_{1.08}$, $LaFe_{11.05}Co_{0.94}Si_{1.01}$ and $LaFe_{10.96}Co_{0.97}Si_{1.07}$. The specific heat capacity $C_P(H,T)$, reported in figure I.37, was measured at external field values of 0 to 1 T I n a temperature interval from 250 to 310 K; no hysteresis is observed in the LaFeCoSi samples. The position of the peak of both ΔS, C_P and ΔTad changes between the three different composites of LaFeCoSi alloy. Thus, it is clearly seen that the peak position is tuneable in room temperature range.

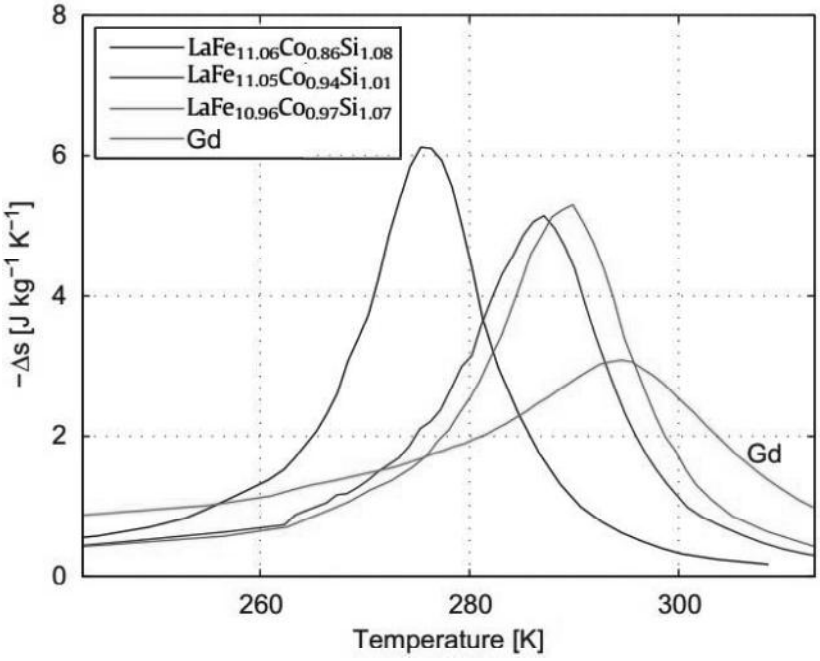

Figure I.35 *-ΔS_M (H,T) of LaFeCoSi compounds under 1T as magnetic field induction, compared with a commercial Gd sample.*

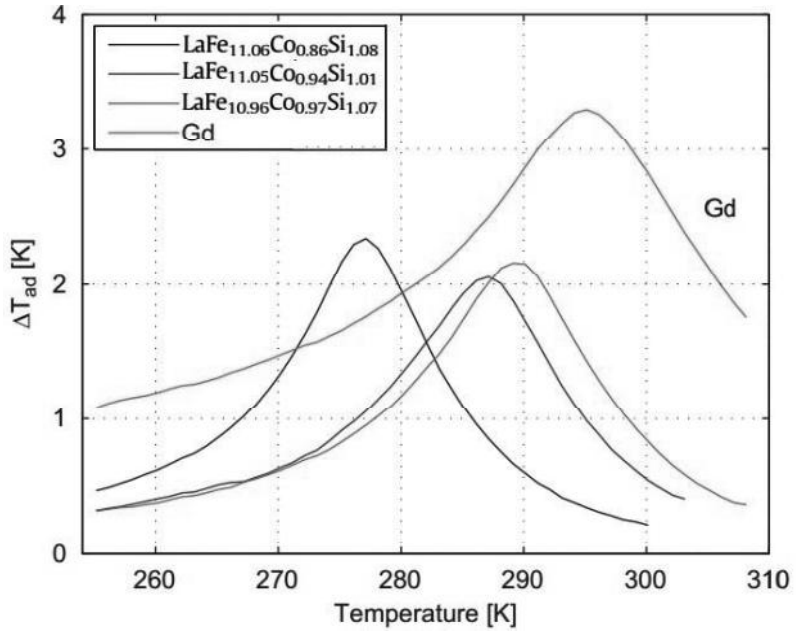

Figure I.36 *ΔT_{ad} (H,T) of LaFeCoSi compounds for magnetic field inductions which change from 0 to 1 T.*

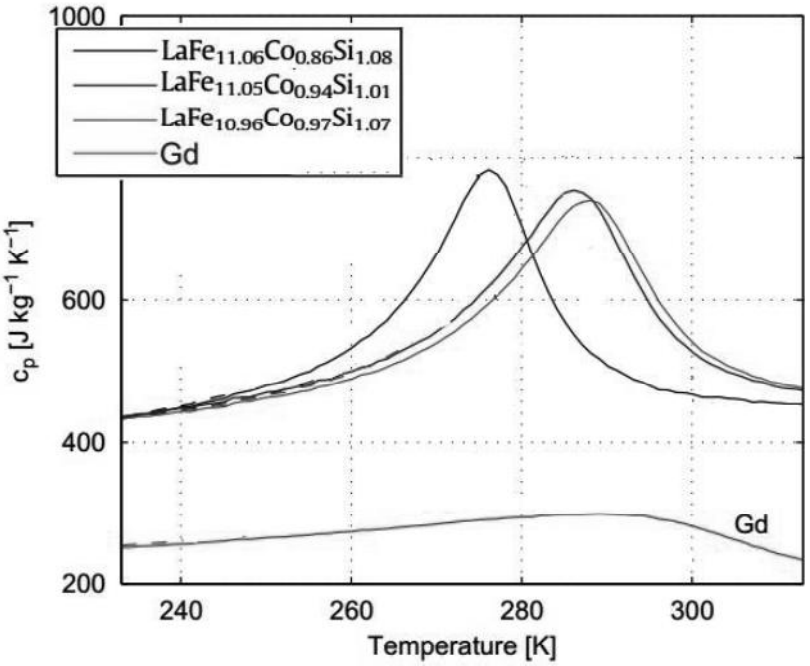

Figure I.37 *The heat capacity of LaFeCoSi compounds as a function of temperature under 1 T, compared with commercial gadolinium.*

I.6.3.3 Rare Earth-Free Crystalline Materials: MnAs alloys

MnAs alloys also assume the role of candidates for new magnetic refrigeration materials at room temperature because those compounds have a giant MCE exhibiting at first order magnetic transition; by varying alloy's composition, the Curie temperature could be switched in the range 220÷318 K. Anyway, MnAs shows also a thermal hysteresis that is bad for practical application. Among Mn-based compounds, $MnFeP_{1-x}As_x$ compounds that are stable for $0.15 < x < 0.66$ and exhibit interesting magnetic properties associated with a first order metamagnetic transition. The Curie temperature of the alloy increases linearly with the As contents. $MnFeP_{1-x}As_x$ shows a large magnetic entropy change with the same magnitude as $Gd_5Si_2Ge_2$.

$MnFeP_{0.45}As_{0.55}$, is an interesting MnAs alloys: it undergoes a FOMT from paramagnetic to ferromagnetic at 307 K (on heating) according to a rapid decrease of the material parameters which changes its Debye temperature and its electronic structure (de Oliveira and von Ranke, 2005). The first order transition occurs at 302.8 K on cooling, and at 306.6 K on heating. This indicates a thermal hysteresis of 3.8 K. The change in volume at the transition temperature is about 2.2%. The adiabatic temperature change for these compounds is relatively low and the thermal conductivity is significantly lower than that of gadolinium and other magnetic materials.

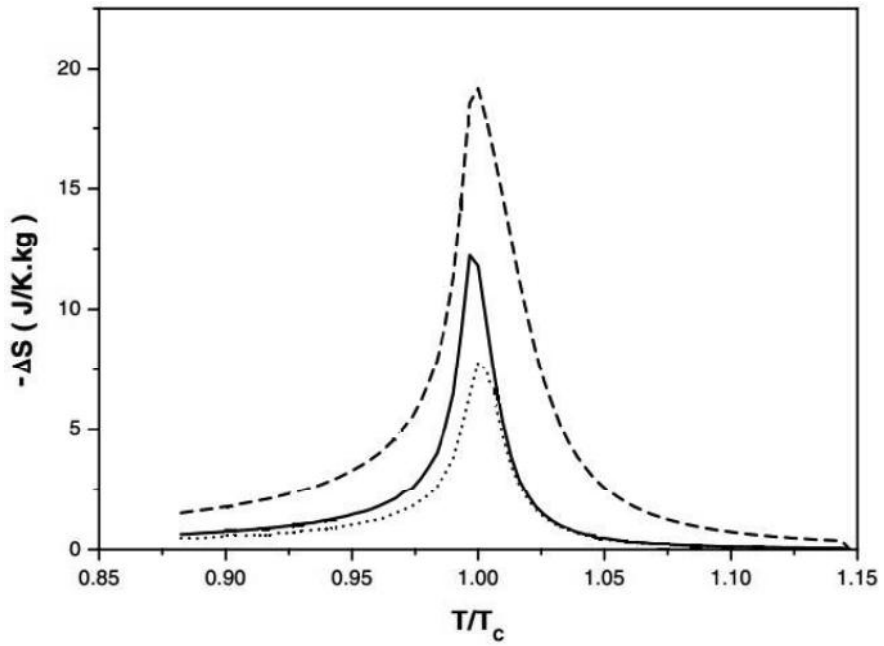

Figure I.38 *Isothermal entropy change Isothermal entropy change (-ΔS) for $MnFeP_{0.45}As_{0.55}$. The dotted, solid and dashed lines correspond to a magnetic field induction from 0 to 1.45 T, from 0 to 2 T and from 0 to 5 T respectively.*

In figure I.38 is shown the isothermal entropy change $\Delta S(H,T)$ of $MnFeP_{0.45}As_{0.55}$, measured under different magnetic field inductions. The large value of the isothermal entropy change in the compound $MnFeP_{0.45}As_{0.55}$ is associated with the first-order magnetic phase transition, which is due to the strong magneto-elastic coupling.

Figure I.39 reports the adiabatic temperature change $\Delta T_{ad}(H,T)$ of $MnFeP_{0.45}As_{0.55}$, measured under different magnetic field inductions. Under a magnetic field induction varying in 0÷5 T range, a maximum $\Delta T_{ad}(H,T)$ of 7.4 K has been registered around the Curie temperature of the compound, whereas for a 0÷2 T variation, the maximum MCE measured corresponds to 3.5 K as adiabatic change of temperature.

Figure I.40 displays the specific heat capacity of $MnFeP_{0.45}As_{0.55}$, evaluated during a magnetic field induction growing from 0 to 1 T. The curve exhibits a peak at 305 K, a slightly lower value than Curie point.

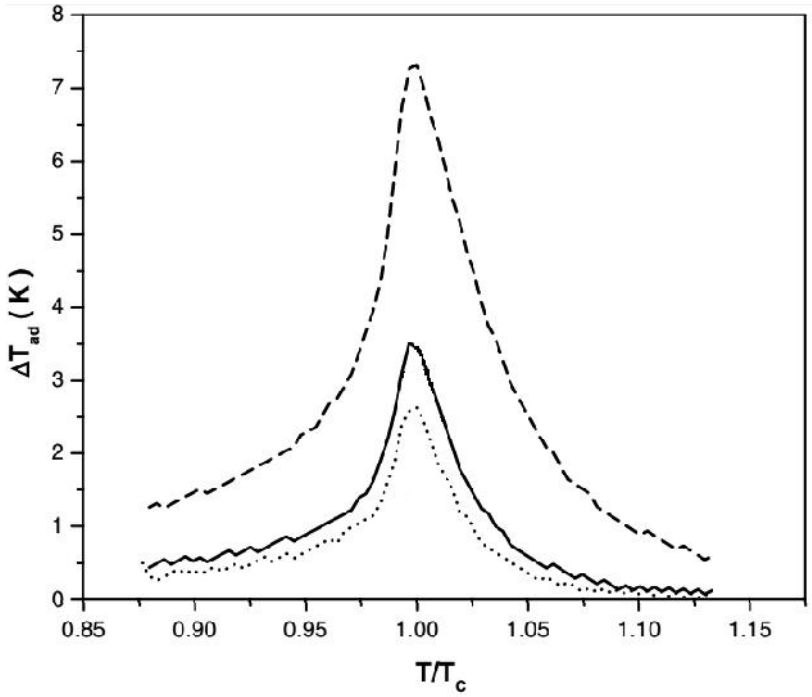

Figure I.39 *Adiabatic temperature change (ΔT_{ad}) for $MnFeP_{0.45}As_{0.55}$ for a magnetic field induction from 0 to 1.45 T (dotted line), from 0 to 2 T (solid line) and from 0 to 5 T (dashed line).*

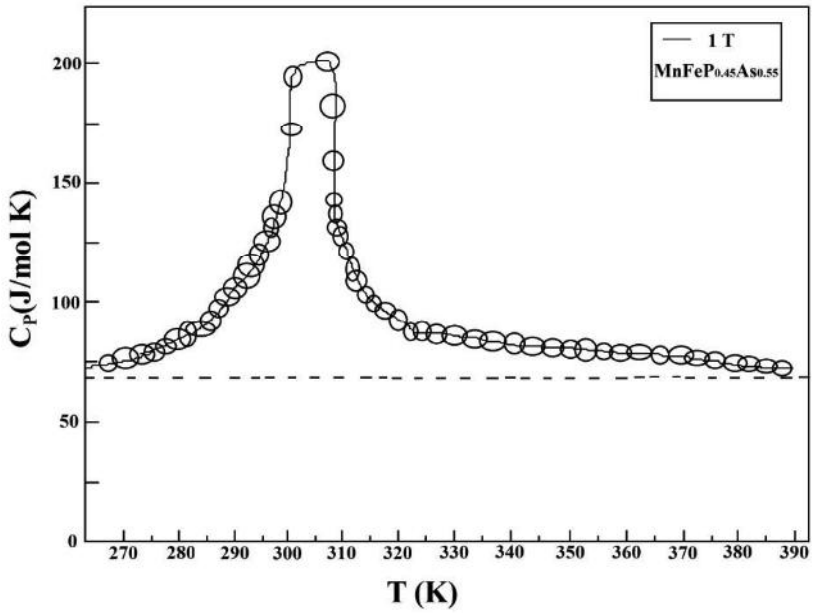

Figure I.40 *$MnFeP_{0.45}As_{0.55}$ heat capacity, evaluated under a magnetic field induction varying from 0 to 1 T.*

I.6.3.4 Oxide Materials: manganese perovskites $Pr_{1-x}Sr_xMnO_3$

The best oxides for MCE around room temperature are manganese perovskites: among them, the series $Pr_{1-x}Sr_xMnO_3$ is noteworthy, since it has the advantage to contain fewer elements, so to have an easier synthesis and a better control of Curie temperature. Since the T_C in $Pr_{1-x}Sr_xMnO_3$ was found to be very sensitive to the substitution level (displacement of about 4 K per % of Sr, in this range of x), several x values could be investigated.

$Pr_{0.65}Sr_{0.35}MnO_3$, investigated by Guillou et al (Guillou et al., 2012), is a SOMT manganese perovskite whose Curie temperature is located at 294 K, where a modest MCE has been observed. Figure I.41 reports the isothermal entropy change $\Delta S(T,H)$ evaluated for $Pr_{0.65}Sr_{0.35}MnO_3$ under a magnetic field induction which rises from 0 to 1 T. The intensity of the peak, located at 295 K, is about -2.3 J/kg K.

Figure I.42 shows the adiabatic change of temperature $\Delta T_{ad}(H,T)$ calculated for $Pr_{0.65}Sr_{0.35}MnO_3$ in case of a field change ΔB=1T. Consistently with the $\Delta S(T)$ curve, the peak is found to be located just below 295 K. Figure I.43 exhibits the specific heat curve $C_P(H,T)$ of $Pr_{0.65}Sr_{0.35}MnO_3$ under a magnetic field induction rising (red line) and falling (black line) in 0÷1 T range.

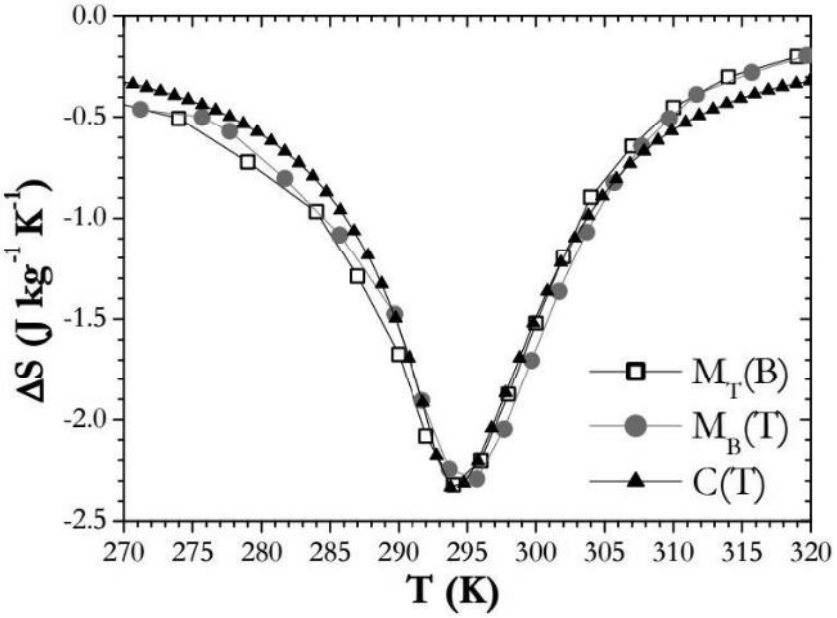

Figure I.41 *Isothermal entropy change Isothermal entropy change (ΔS) for $Pr_{0.65}Sr_{0.35}MnO_3$, resulting from the analysis of magnetization And heat capacity data for a field change of ΔB=1T*

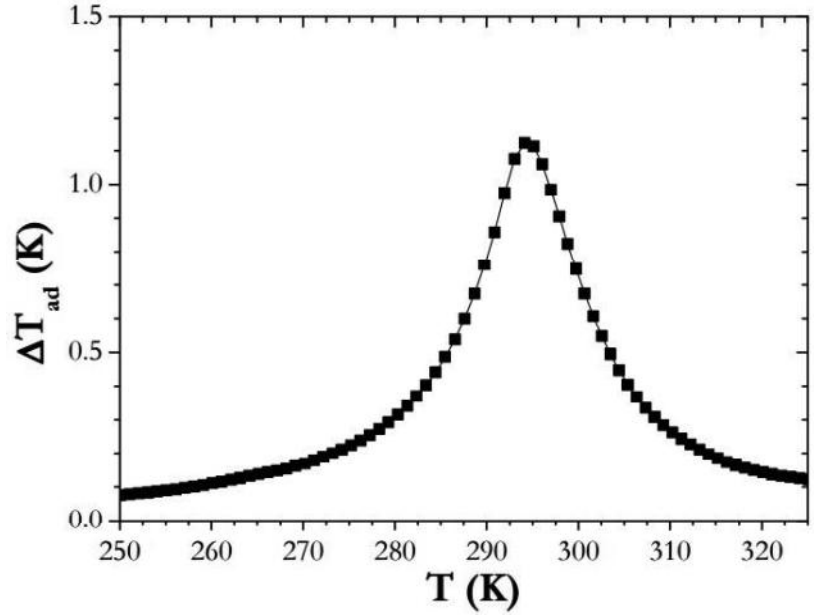

Figure I.42 *Adiabatic temperature change (ΔT_{ad}) for $Pr_{0.65}Sr_{0.35}MnO_3$, measured for a field change of 1T.*

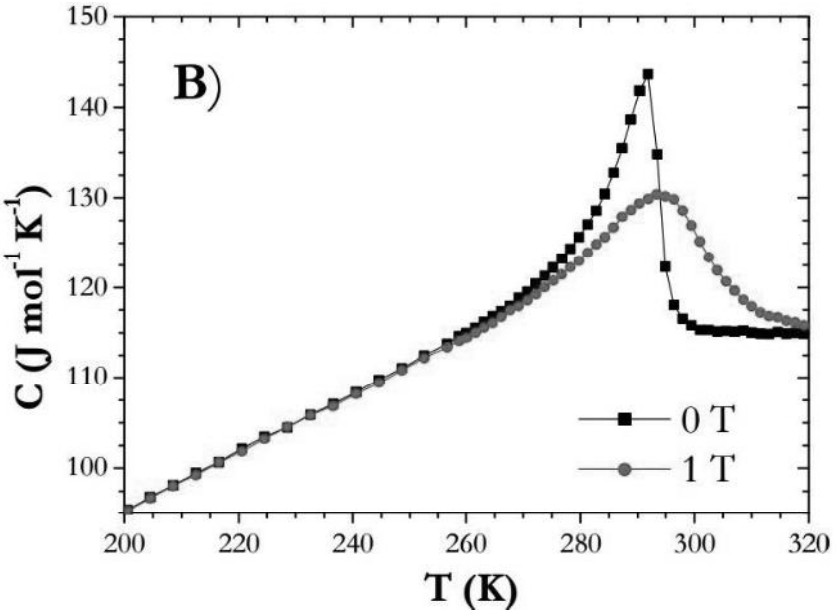

Figure I.43 *$C_P(H,T)$ measured for$Pr_{0.65}Sr_{0.35}MnO_3$, measured for a field induction rising (red line) and falling (black line) in 0÷1 T range.*

I.6.4 General summary of magnetocaloric materials

Table I.1 summarizes the physical and MCE characteristics of the presented magnetocaloric materials in the room temperature range: ΔT_{ad} and ΔS_M reported are the peak value evaluated under a magnetic field induction ΔB of 1.5 T. The FOMT materials have peak values of ΔT_{ad} and ΔS_M always higher than Gd ones. $Gd_5(Si_2Ge_2)$ shows the higher peak value, but at lower temperature with respect to the ones proper of the other materials considered. Gadolinium has the greatest thermal conductivity value, but it is comparable with the ones of $La(FeSi)_{13}$ alloys.

Table I.1 *Physical and MCE characteristics of magnetocaloric materials in the room temperature range.*

Materials	T_c [K]	ΔT_{ad} [K]	ΔS_M [J/kg K]	ρ [kg/m^3]	k [W/mK]
Gd	294	6	5	7900	10.9
$Gd_5(Si_2Ge_2)$	276	7.8	14	7205	5.8
$LaFe_{11.384}Mn_{0.356}Si_{1.26}H_{1.52}$	290	5	10.5	7100	9
$LaFe_{11.05}Co_{0.94}Si_{1.01}$	287	3.17	5.5	7290	8.9
$MnFeP_{0.45}As_{0.55}$	307	4	12	7300	2.5
$Pr_{0.65}Sr_{0.35}MnO_3$	295	1.5	2.5	5800	1.8

Table I.2 reports the main parameters of the different materials in order to compare them in terms of RCP vs. costs. In terms of RCP(T) and RCP(S), Gd is the best material for magnetic refrigeration; $Gd_5(Si_2Ge_2)$ also shows acceptable values. From a commercial point of view, $Gd_5(Si_2Ge_2)$ and Gd are very expensive and the magnetic transition metals are more adequate than the rare earths for industrial production of magnetic cooling engines scopes. The price of $MnFeP_{0.45}As_{0.55}$ is quite low, but processing of As is complicated due to its toxicity.

Table I.2 *A comparison among magnetocaloric materials in terms of relative cooling powers and costs.*

Materials	RCP(T) [K^2]	RCP(S) [J/kg]	Price [€/kg]
Gd	187	240	3000
$Gd_5(Si_2Ge_2)$	117	154	9000
$LaFe_{11.384}Mn_{0.356}Si_{1.26}H_{1.52}$	50	115	1200
$LaFe_{11.05}Co_{0.94}Si_{1.01}$	30	83	1200
$MnFeP_{0.45}As_{0.55}$	40	180	1500
$Pr_{0.65}Sr_{0.35}MnO_3$	27	38	1050

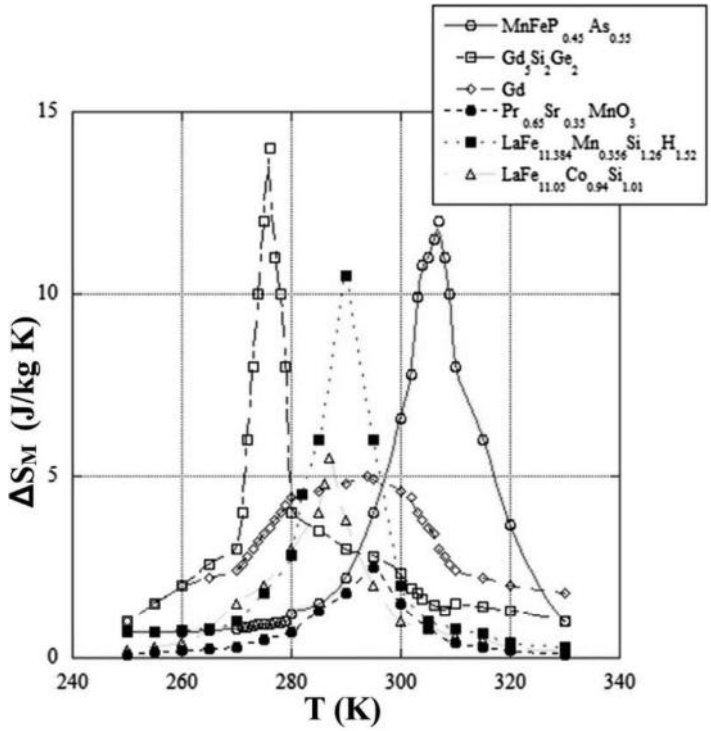

Figure I.44 *-ΔS_M (H,T) temperature's function measured under 1.5T as magnetic field induction, for the presented magnetocaloric materials.*

In Figure I.44 and I.45 are reported ΔS_M and ΔT_{ad} as a function of temperature for the above mentioned magnetic materials, under a magnetic field induction varying in 0÷1.5 T (Aprea, 2015b). Fig. I.44 clearly shows that $Gd_5(Si_2Ge_2)$, $LaFe_{11.384}Mn_{0.356}Si_{1.26}H_{1.52}$ and $MnFeP_{0.45}As_{0.55}$ compounds exhibit the greatest values of ΔS_M. These materials are FOMT and therefore the magnetic entropy variation due to MCE is confined in a quite small temperature range. On the other side Gd shows lower values of ΔS_M but MCE effect spreads over a broad temperature range. $Pr_{0.65}Sr_{0.35}MnO_3$ displays a very low magnetic entropy change in the whole temperature range. Figure 1.45 reveals that $Gd_5(Si_2Ge_2)$ and Gd present higher values of ΔT_{ad}, whereas $MnFeP_{0.45}As_{0.55}$ has the disadvantage that the adiabatic temperature change is not very large due to the reasonably higher heat capacity.

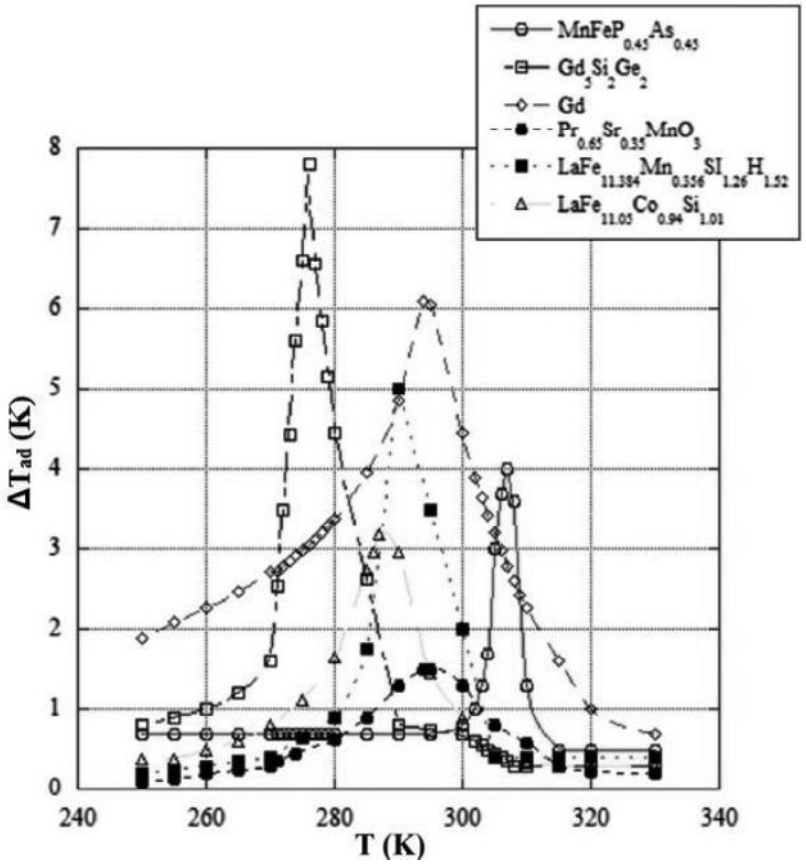

Figure I.45 *ΔT_{ad} (H,T) temperature's function measured under 1.5T as magnetic field induction, for the presented magnetocaloric materials.*

Chapter II
The Rotary Permanent Magnet Magnetic Refrigerator

II.1 Rotary Permanent Magnet Magnetic Refrigerator design

This chapter illustrates a Rotary Permanent Magnet Magnetic Refrigerator (RPMMR) (Aprea et al., 2014a, 2014b, 2016c, 2016d), which is the first Magnetic Refrigerator developed in Italy. The device has been developed at the Refrigeration Lab (LTF) of the University of Salerno in cooperation with the University of Naples "Federico II" and it presents a rotating magnetic group, whereas the magnetocaloric material (MCM), i.e. gadolinium, is stationary. 8Mag is the name of the device, visible in figure II.1, which comes from both the octagonal shape of magnetic system and the total number of regenerators employed. The 8Mag principle of operation is based on the AMR thermodynamical cycle. Below are described the design choices and the technical solutions that led to this final design.

II.1.1 Magnetic system: design and testing

The magnetic system, illustrated in figure II.2 and II.3(a) is composed of four permanent magnet assemblies, which are arranged in a “double U” configuration, as clearly visible in figure II.3(b). The magnets are held by two aluminum supports and mounted on a shaft, so that the axis of symmetry in the U arrangement coincides with the rotational axis of the magnetic group.

Thanks to the “double U” extensions, this configuration provides two high (HMF) and two low magnetic field (LMF) hemicycle regions. Specifically, in the HMF region, the magnetic flux density (B) is greater or equal to 90% of the peak magnetic flux density, whereas in the LMF region, B is less than or equal to 2% of the peak flux density.

Figure II.1 *Picture of 8Mag.*

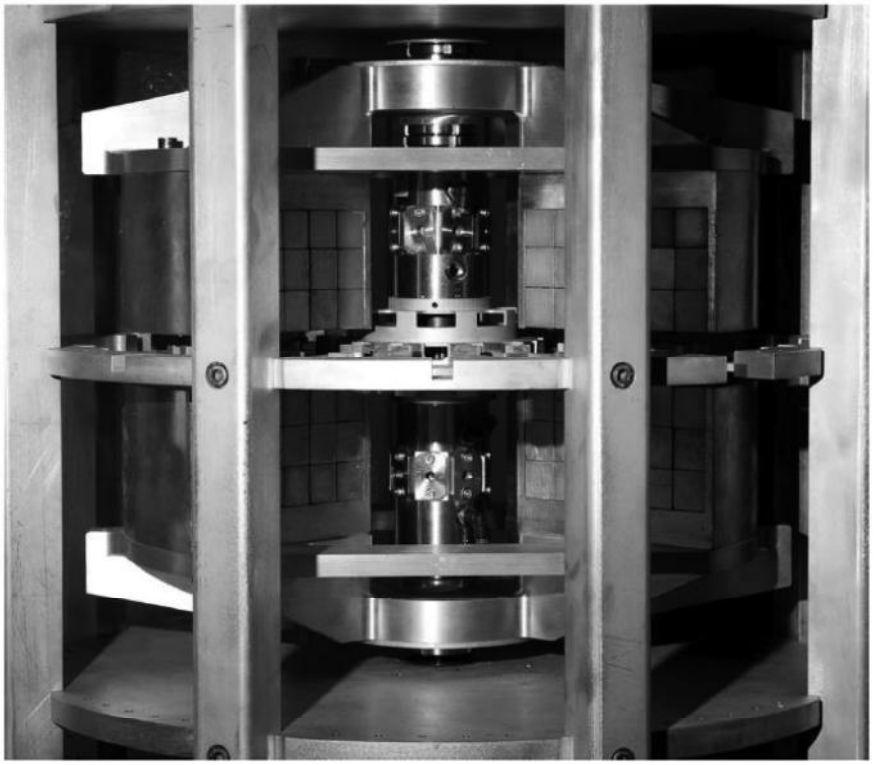

Figure II.2 *Side view of the 8Mag magnetic system.*

.

The design process focused on the following objectives: uniform flux density in the HMF and in the LMF regions, high accessibility to the MCM, and large MCM mass. The price to pay for the regenerator accessibility is the lack of a common iron yoke for the return flux lines, thus reducing the efficiency of the magnet design. A number of configurations were simulated using finite element method, and the final solution resulted in a design based on a Halbach array structure segmented in three differently magnetized components, two horizontally and one vertically oriented, as shown in figure II.4. The magnets are grouped in four sets, two defined as North Poles and two as South Poles. Each assembly is a hemicycle, with an opening angle of 80°, an outer diameter of 520 mm, an inner diameter of 170 mm, and a height of 100 mm. Each assembly consists of 90 magnetized blocks, which are monolithically glued together and encased in a steel yoke. Each segment is made of sintered NdFeB with a residual Br of 1370 mT (as declared by the manufacturer). Two sets of paired ring-nuts, as in fig. II.3(a), lock each magnet assembly on the support shafts and allow for adjusting the distance between the upper and the lower U arrangements, for which the air gap between the magnetic poles can be set between 20 mm and 50 mm.

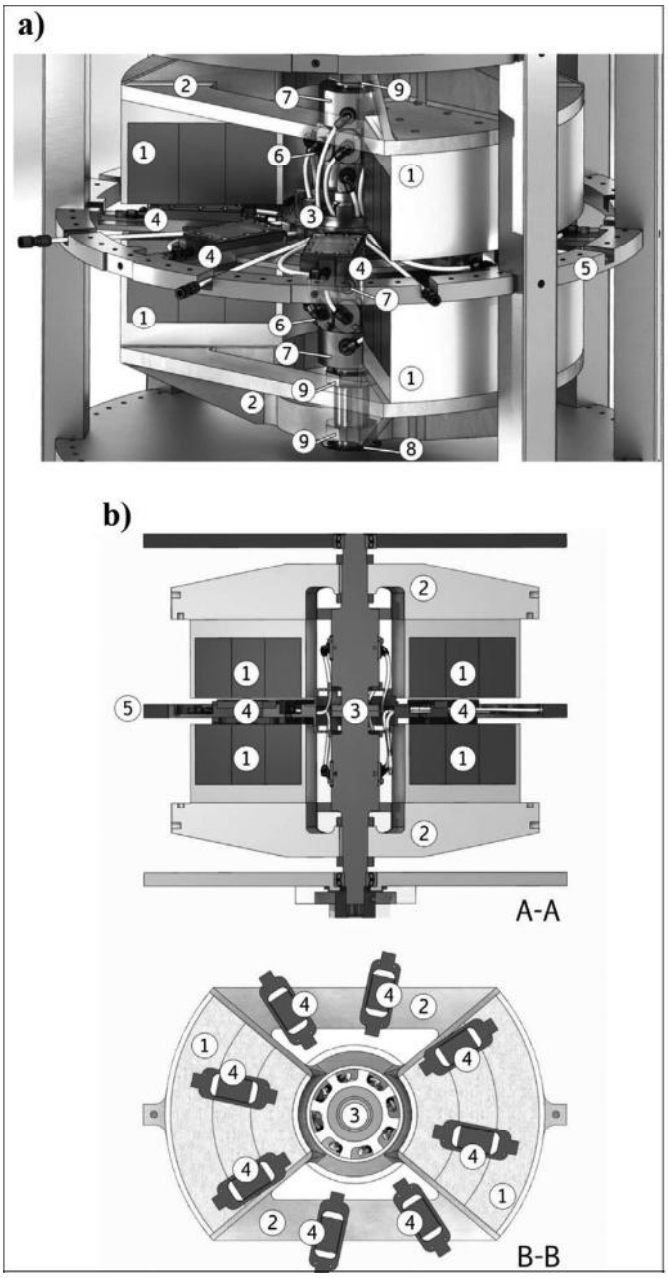

Figure II.3 *(a) 8Mag core details: 1)permanent magnet assembly; 2)mounting support; 3)shaft-rotary valve combination; 4)regenerator; 5)magnetocaloric wheel; 6)fluid manifold to/from regenerators; 7)fluid manifold to/from heat exchanger; 8)bearings; 9)adjustable rings. (b) Longitudinal (A-A) and axial section (B-B) of the device core.*

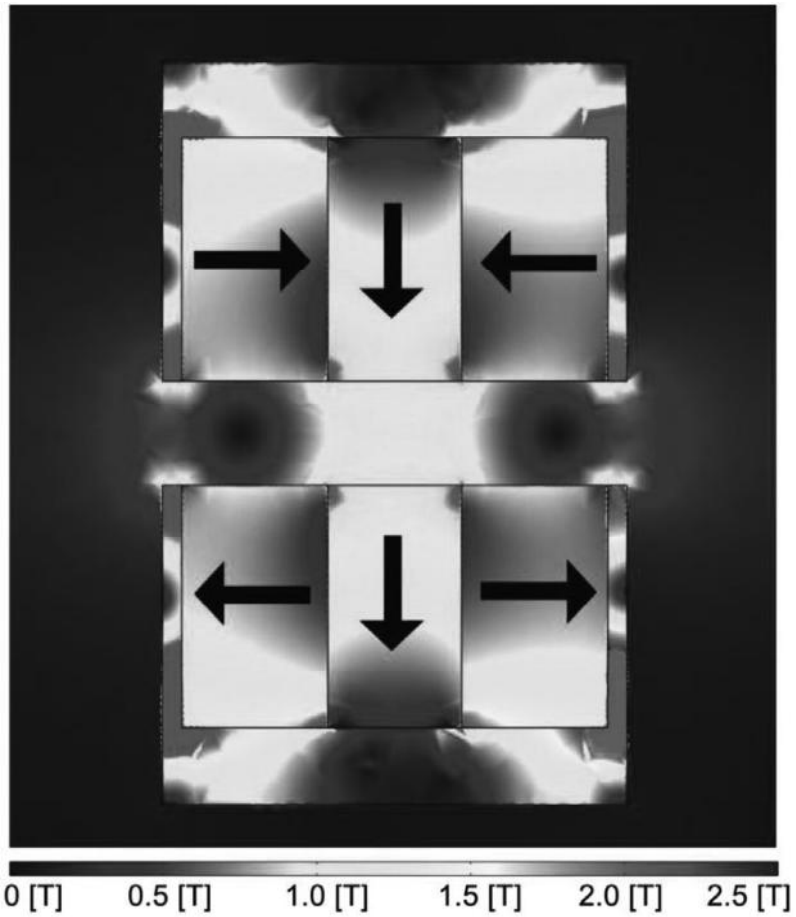

Figure II.4 *Halbach array configuration adopted in 8Mag (longitudinal section).*

The 8Mag design provides two magnetized regions, each shaped as a hemicycle, as figure II.3(B) demonstrates, with an outer diameter of 410 mm and an inner diameter of 280 mm. In the current configuration, the air gap is set to 43 mm. The flux density was measured (with a Hall probe) as a function of the angle, radius, and height. As shown in Fig. II.5(a), the flux density is periodic with a period of 180°, with the peak flux density as high as 1.25 T in the high magnetic field region (HMF) and as low as 0.01 T in the demagnetized region (LMF). Furthermore, as visible in Fig. II.5(a), each HMF region is 60° wide, whereas each LMF is 70°. The remaining width of 50° belongs to the transition regions.

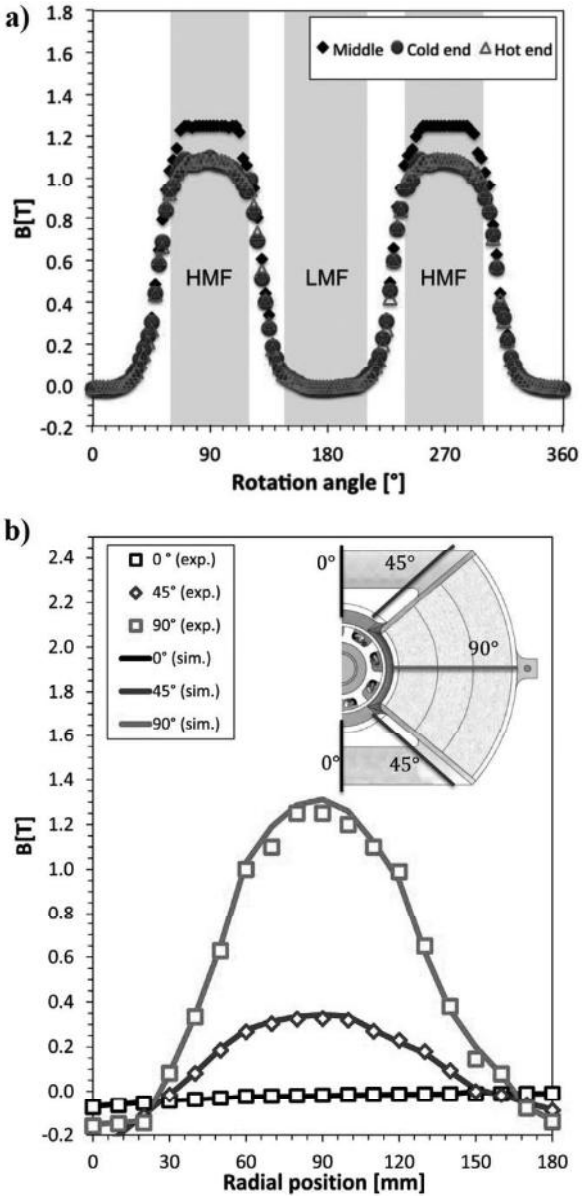

Figure II.5 *(a) Measured flux density as a function of the rotation angle at three radial positions: Hot end (200 mm); middle end (177.5 mm); cold end (155 mm). (b) Flux density as a function of the radial position for three angular positions (0°, 45°, 90°): the markers identify the experimental results (exp.), whereas the lines report the simulated values (sim.). Zero is not the symmetry axis but the inner diameter of the magnetic system. The cold end of the regenerator is located at 65 mm, and the hot end is located at 110 mm.*

It is useful to mention a figure of merit for evaluating magnetic structures in magnetic refrigerators, which has been previously introduced in literature (Bjørk et al., 2010b), defined as:

$$\Lambda_{cool} = \left(\bar{B}_{High}^{2/3} - \bar{B}_{Low}^{2/3}\right)\frac{V_{field}}{V_{mag}}P_{field} \quad \text{(II.1)}$$

where $\bar{B}_{High}$ is the average high magnetic field intensity, $\bar{B}_{Low}$ is the average low magnetic field, V_{mag} is the volume of the magnets, V_{field} is the volume with a high magnetic flux density equal to B_{High}, and P_{field} is the fraction of an AMR cycle for which the field generator is actively used. Due to the fact that the magnets in the 8Mag continuously rotate, always engaging at least one AMR bed, the P_{field} parameter is equal to 1. The magnetic flux distribution, reported in figure II.5(a) shows that:

- there is a volume 80° wide where the average magnetic field intensity is equal to the lower limit of the magnetic flux density in the HMF region (1.12 T);
- in the LMF region, the B is 0.06 T.

Consequently, considering a B_{High} equal to 1.12 T, the V_{mag} is equal to 2.7 l and B_{Low} is 0.06 T, whereas the total volume of the magnetic system is 32.5 l. These values lead to a Λ_{cool} of 0.08. Figure II.5(b) shows that the simulated flux density is in agreement with the experimental measurements with a maximum error of 5%. Table II.1 presents the simulated flux densities for different air gaps and the relative Λ_{cool} parameter.

Table II.1 *Performances of the magnetic system for different height of air gap.*

Air gap	Flux density		Λ_{cool}
[mm]	High $\bar{B}$ [T]	Peak [T]	$[T^{2/3}]$
20	1.60	1.70	0.05
43	1.10	1.25	0.08
50	0.85	0.98	0.09

II.1.2 Hydraulic system design

A pump-rotary valve combination creates an oscillating fluid flow through the regenerators, allowing a unidirectional flow in the system outside the regenerators and the tubing leading to them from the valve. With the purpose of reducing the total dimensions of the device, the valve has been located centrally, as indicated in figure II.3(a), and it also acts as the drive shaft. The valve consists of two main parts: a rotor and a stator. The rotor operates both as a rotary manifold and as a shaft for the magnetic system. For this purpose, a cylindrical shaft made of stainless steel has been drilled to achieve an internal hydraulic circuit. The rotor has been directly linked to the magnetic system; consequently, the rotational frequency of the

magnets is the same as the rotational frequency of the rotor. The stator is rigidly fixed to the support of the regenerators, and it is divided into a hot sub-valve (HV) and a cold sub-valve (CV). Each sub-valve has eight ports to hydraulically connect the regenerators to the rotary manifold and two additional ports to complete the hydraulic circuit with the heat exchangers.

Fig. II.6 illustrates the equivalent hydraulic circuit.

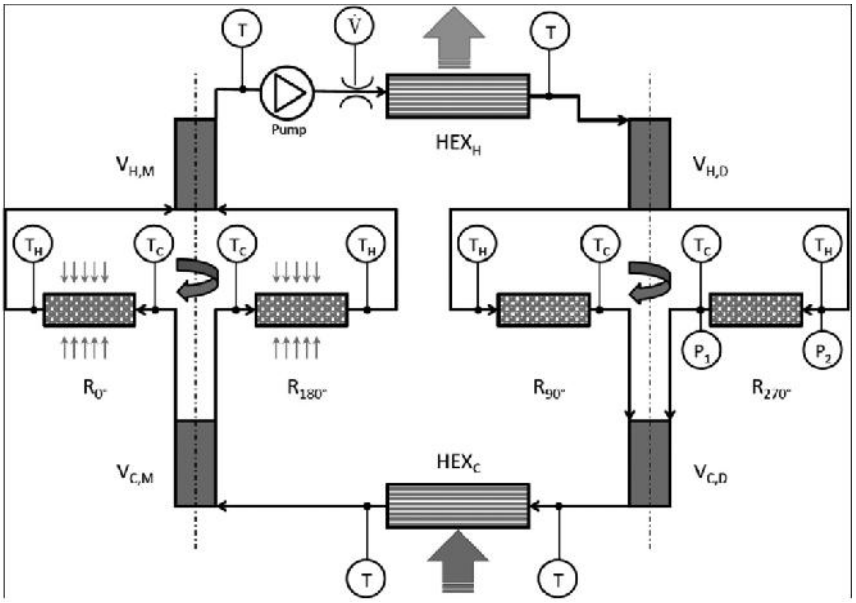

Figure II.6 *Equivalent hydraulic circuit: $V_{H,D}$ is the valve connected with the hot end of the demagnetized regenerators; $V_{C,D}$ is the valve connected with the cold end of the demagnetized regenerators; $V_{H,M}$ is the valve connected with the hot end of the magnetized regenerators; $V_{C,M}$ is the manifold connected with the cold end of the magnetized regenerators. R0° and R180° are the magnetized regenerators, hydraulically in parallel flow; R90° and R270° are the demagnetized regenerators hydraulically coupled to R0° and R180°, also in parallel flow.*

The rotation of the magnets and that of the manifold are synchronized, during the operation of the drive motor.

Demineralized water is used as the regenerating fluid, and a commercial rotary vane pump, able to return a maximum volumetric flow rate of 16 l/min at 1.6 MPa, has been adopted. As suggested by the literature (Lozano et al., 2013; Zamni et al., 2012) the regenerating fluid included corrosion inhibitors to protect the gadolinium. A three-phase ac motor controlled by a frequency inverter drives the pump so that the volumetric flow rate can be varied during operation. The hydraulic circuit tubing is polyethylene, and the

tubes connecting the regenerators to the rotary valve are clear polyamide so that the fluid can be visually inspected during filling. Because the fluid flow in the heat exchangers is unidirectional, they are not constrained to be adjacent to the regenerators. Therefore, the heat exchangers can be conveniently installed, modified and replaced, simplifying the process of testing their performance. During the initial tests, a conventional coaxial heat exchanger was adopted as a hot reservoir, whereas a finned tube heat exchanger was used as a cold reservoir. Air, of which the temperature can be adjusted by an electrical heater managed by a PID controller, is vented externally to the finned tube heat exchanger as the thermal load. A by-pass allows excluding the cold heat exchanger during testing. Additional components are needed for fluid filling, purging, and avoiding pump cavitation. Two automatic air vent valves and a closed expansion vessel have been installed.

II.1.3 Regenerator design and magnetocaloric material employed

The 8 regenerators are supported by an aluminum structure (or magnetocaloric wheel) with 45° spacing. This assembly is constrained to the stator of the rotary valve and to the frame of the device. Each regenerator, visible in figure II.7, consists of a magnetocaloric material (MCM) matrix enclosed in a shell made of PA6-G MO (polyamide and MoS_2). This material is inexpensive and it has low thermal conductivity (0.23 W/mK), good machinability, and good mechanical strength. A stainless steel (AISI 304) lid is fastened on the top of the shell, and an O-ring ensures its sealing.

The final dimensions of the shell-lid combination were obtained with the help of a FEA model built through COMSOL, a finite element method software) and it was designed for a minimum safety factor of 2.5 and a maximum internal operating pressure of 1.5 MPa. Each assembly was tested at 2.0 MPa with no fracture or water leakage. To reduce heat losses, a plate of SB (polystyrene copolymer) with a thermal conductivity of 0.14 W/mK was bonded to the inner side of the stainless-steel lid. Push-to-connect fittings are installed at each end of the regenerator shell to hydraulically connect the regenerator to the rotary valve to the temperature and pressure sensors. Two rapid prototyped diffusers are located at the inner ends of the shell with the objective of homogeneously distributing the flow as the water reaches the regenerator matrix.

Each regenerator has a height of 20 mm, a length of 45 mm, and a width of 35 mm. The aspect ratio is 1.5 and the volume available for the MCM is 31.5 cm^3. The regenerators consist of packed gadolinium spheres with a diameter in the range of 400-500 microns. As declared by the manufacturer, the gadolinium spheres were obtained using a Plasma Rotating Electrode Process (P.R.E.P.), which led to a purity of the gadolinium equal to 99.82%.

Each regenerator housing was filled with 150 g of gadolinium with a mean porosity of 0.35. The total MCM mass in the device was 1.20 kg with only 60% of the total available MCM volume being used.

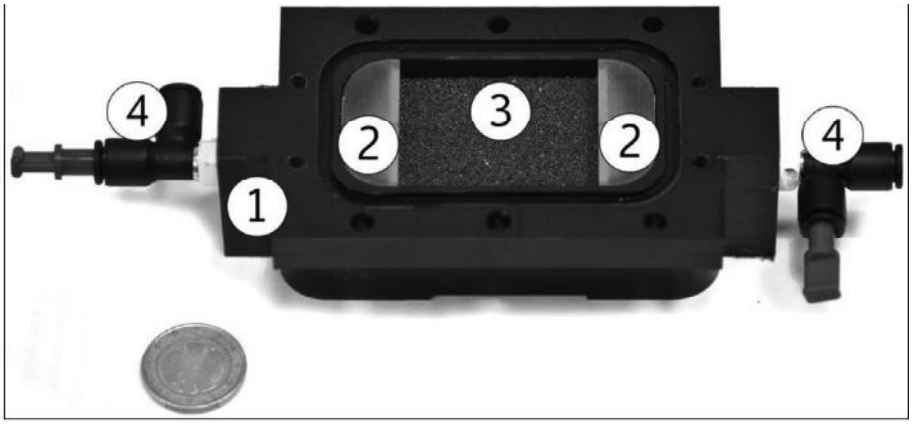

Figure II.7 *Regenerator details: 1) shell, 2) diffuser, 3) magnetocaloric material, 4) push-in fitting.*

II.1.4 Drive system and operating characteristics

The drive system, reported in table II.2, consists of a brushless DC motor rotating the magnets at variable speed between 0.1 and 1 Hz. The motor is coupled to the rotor side of the valve through a planetary gear-head with a reduction ratio of 93:1. A digital encoder and a programmable speed controller complete the drive system. This results in an available maximum continuous torque of 70 Nm at 54 rpm.

Table II.2 *DC Motor and planetary gearhead combination data.*

Brushless DC Motor	
Nominal voltage	48 [V]
Nominal speed	4960 [rpm]
Nominal torque	0.747 [Nm]
Nominal current	0.733 [A]
Maximum efficiency	86%
Planetary gearhead	
Number of stages	3
Reduction	93:1
Maximum efficiency	70%

As previously announced, the rotation ensures the simultaneous operation of the valve and magnets. During the rotation of the magnetic system, the

relative angular position between the rotor and the stator of the rotary valve imparts the fluid flow direction. The diameter of the ports is dimensioned to match the appropriate flow timing during high and low fields. Each regenerator-blowing phase corresponds to 45 degrees of field generator system rotation. A closed expansion vessel avoids pressure spikes during the no flow condition when switching between active ports. As shown in the equivalent hydraulic system of figure II.6, the hydraulics of the regenerators located in the HMF regions are in parallel, as are those located in the LMF. For every full rotation of the magnetic system, each pair of regenerators experiences two AMR cycles; therefore, the AMR frequency is twice the frequency of the magnetic system.

II.2 Experimental investigation

A number of different experimental investigations has been performed on the rotary permanent magnet magnetic refrigerator 8Mag.

Initial tests have been conducted (Aprea et al., 2014a, 2015a) for the characterization of the device performances under no applied thermal load, while the refrigerant employed was gadolinium in packed bed configuration. This typology of is not fully exhaustive for defining the operating limits of 8Mag, which requires further experimental investigation. For this reason, other tests have been scheduled to study the energy performance of 8Mag in terms of refrigeration power, energy losses, and COP. Therefore, in subsequent campaigns of tests (Aprea et al. 2016c, 2016d) the device performances have been explored under the application of different cooling load to carry out the RPMMR's answer in terms of cooling power and coefficient of performance (COP).

II.2.1 Experimental apparatus of the RPMMR

The experimental equipment of measurements of the RPMMR allows measurements of temperature span, pressure drop, AMR frequency, and volumetric flow rate of the regenerating fluid thermal load, electrical power and COP.

Using PT100 thermo-resistances placed between the input and output of each component, the temperature of the regenerating fluid is measured. In particular, referring to figure II.8:

- the temperature span (ΔT_{span}) is the average time between the temperature of the regenerating fluid exiting the hot side (T_{HFo}) and the temperature of the regenerating fluid exiting the cold side (T_{LFo});
- the temperature of heat rejection (T_H) is the average time between the temperature of the water exiting the hot side of the magnetic

refrigerator (T_{HFo}) and the water exiting the geothermal probe (T_{HFi}), both measured under steady state condition.

By using a magnetic flow meter placed between the pump and the hot heat exchanger, the volumetric flow rate of the regenerating fluid is measured. To estimate the pressure drop of the entire device, two piezoelectric pressure sensors placed between the input and the output of the pump are employed. Referring figure II.8, the total pressure loss is evaluated as the average time over the difference between the pressure at the outlet (P_{out}) and the pressure at the inlet of the pump (P_{in}). The pressure measurements are also performed at the ends of the regenerators, with the objective of measuring the blow duration and the pressure drop through the regenerators.

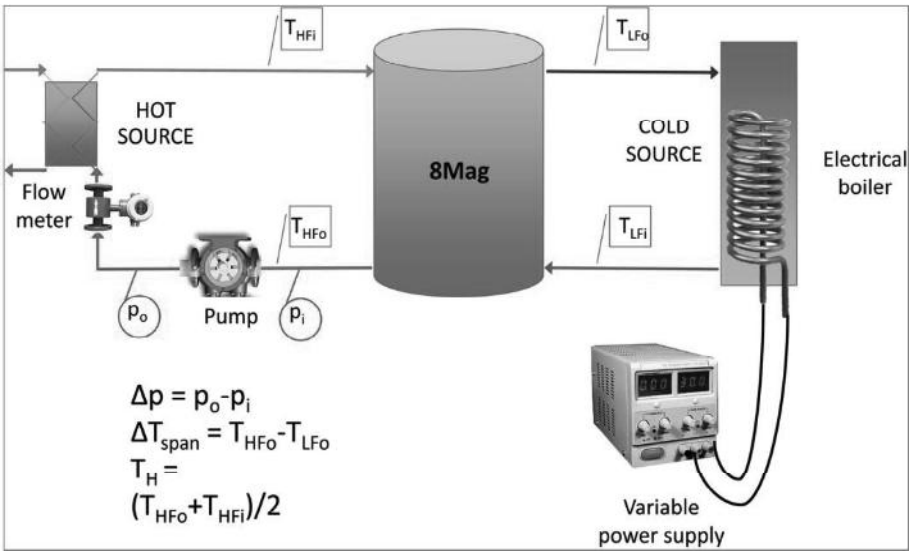

Figure II.8 *A scheme of the experimental apparatus employed for investigating the energy performances of 8Mag.*

Using the digital encoder on the motor, the AMR cycle frequency is also measured. The test apparatus is equipped with 32-bit A/D converter acquisition cards with a sampling rate of up to 10 kHz.

To measure the refrigeration duty provided by 8Mag, a cold heat exchanger has been realized by the combination of electric resistance with a thermally insulated pressure vessel. A variable voltage supply feeds the electrical resistance to provide a thermal load that is variable from 0 to 500W. Water, the temperature of which can be adjusted by an electrical heater managed by a PID controller, is used as a secondary fluid in the hot heat exchanger.

To measure the cooling capacity developed by the device, the outer surface of the cold heat exchanger is thermally isolated. In this way, it is possible to consider the following equation to be valid:

$$\dot{Q}_{ref} = \dot{W}_{el,h} \tag{II.2}$$

where $\dot{W}_{el,h}$, is the electrical power that is absorbed by the electric heater inserted into the exchanger and measured using a watt transducer. Using a PT100, temperature measurements on the outer surface of the insulation coat of the exchanger are performed to verify the quality of the insulation level. Moreover, using a 2 W transducer, the electrical power absorbed by the pump ($\dot{W}_{el,p}$) and the electrical power absorbed by the electric motor used for magnet rotation ($\dot{W}_{el,m}$) are evaluated. For the evaluation of the COP, the following equation is used:

$$COP = \frac{\dot{Q}_{ref}}{\dot{W}_{el,m}+\dot{W}_{el,p}} \tag{II.3}$$

In Table II.3, the accuracies and the characteristics of the sensors, employed for this investigation, are reported.

Table II.3 *Characteristics of the sensors used and the accuracy of the measurements performed.*

Quantity	Characteristic	Accuracy
Temperature	RTD PT100	±0.1 [K]
Pressure	Piezoelectric pressure gauge	±75 [kPa]
Volumetric flow rate	Electromagnetic flow meter	±0.5 %
Frequency/rpm	Optical encoder	±0.01 [°/s]
Mass	Electronic balance	±0.2 [g]
Electrical Power	Electromagnetic wattmeter	±0.2 %
Torque	Torque transducer	±0.5 %
Φ	Procedure introduced in section II.2.2.1	±5.3 %
COP	Eq. II.7 and propagation error	±0.35 %

The utilization factor was estimated from the fluid mass (M_f) over one fluid flow period (Tura and Rowe, 2011):

$$M_f = \int_{\theta_{opening}}^{\theta_{closed}} \rho_f \dot{V}(\theta) d\theta \tag{II.4}$$

where $\dot{V}(\theta)$ is the fluid flow rate reported as a function of the rotation angle θ, θ_{closed} is the rotation angle for which the hole is fully closed and $\theta_{opening}$ is the rotation angle for which the hole is opening. Indeed, the utilization factor is defined as:

$$\Phi = \frac{M_s C_s}{M_f C_f} \tag{II.5}$$

where M_f is the fluid mass blown over one cycle through a single regenerator, C_f is the fluid specific heat, M_s is the mass of a single regenerator and Cs is the refrigerant specific heat in the demagnetized state at the Curie temperature. The Φ values in our experimental tests were evaluated according to the procedure identified in the following section (II.2.2.1).

A Virtual Instrument (VI) application developed in Labview collects the signals from the sensors at fixed intervals. Steady state conditions were assumed to be reached when a change in the recorded temperature span is less than its measurement accuracy over a period of 300 s.

II.2.2 Zero thermal load tests

In this section is reported a number of different experimental tests conducted to explore the 8Mag's behavior when no thermal load is applied; such typology is called "Zero thermal load".

II.2.2.1 Experimental procedure and data analysis

During the tests, the operating conditions were analyzed for different AMR cycle frequencies at different heat rejection temperatures, and the volumetric flow rate of the water was kept constant. As Engelbrecht et al. (2012) suggested, for all experiments, the temperature ambient was controlled and kept in a narrow range, between 293 and 296 K. For the purpose of the tests presented in this section, the cold heat exchanger was excluded from the hydraulic circuit so that the no-load performance could be measured while reducing the thermal losses to the environment.

Following the guidelines present in literature (Tura and Rowe, 2011; Engelbrecht et al., 2012; Romero Gómez et al., 2013), the temperature span was calculated as the average temperature difference between the fluid exiting the hot end of the regenerator and the fluid exiting the cold end of the regenerator (ΔT_{AMR}). Furthermore, as Romero Gómez et al., 2013 suggested, the temperature span between the hot and cold source (at the heat exchangers) is also measured (ΔT_{span}). The pressure drop in the regenerator is evaluated as the pressure difference between the fluid exiting the hot end of the regenerator and the fluid exiting the cold end of the regenerator. Because the fluid flow rate through the regenerator cannot be directly measured, indirect estimates are evaluated using the pressure drop at the ends of a regenerator for a range of fluid flow rates, whose results are reported in figure II.9. As suggested by several authors (Engelbrecht et al., 2012; Scarpa et al., 2012; Aprea et al., 2013), the Ergun equation (Ergun, 1952) was used to predict the pressure drops (Δp_{Ergun}) for the fluid flow rate

values. The estimation was then compared to the measured data. Following the suggestions present in the literature (Macdonald et al., 1979; Yang, 2003), a modified Ergun equation was proposed:

$$\Delta p_{Ergun} + F_{add} = L_{PB}\left[\frac{150\mu}{d_p^2}\frac{(1-\varepsilon)^2}{\varepsilon^3}V_0 + \frac{1.75\rho_f}{d_p}\frac{(1-\varepsilon)^2}{\varepsilon^3}V_0^2\right]10^5 + \\ + (10.86V_0 + 61.98V_0^2) \quad \text{(II.6)}$$

where L_{PB} is the length of the packed bed, d_p is the diameter of the particles, ε is the mean porosity, ρ_f is the density of the regenerating fluid, μ is the fluid viscosity and V_0 is the undisturbed velocity of the fluid calculated using the following equation:

$$V_0 = \frac{\dot{V}}{60A_0}10^{-3} \quad \text{(II.7)}$$

where A_0 is the cross section of the regenerator and $\dot{V}$ is the fluid flow rate.

The additional factor (F_{add}) introduced in Eq. (II.6) accounts for both the actual fluid flow distribution and the contribution of the diffusers and fittings. Consequently, the F_{add} here introduced is valid only for the configuration related to these experimental investigations. Different regenerator designs or fluid distributions require new experimental analysis and a different F_{add} expression. The modified Ergun Eq. (II.6) and Eq. (II.7) lead to a statistical model having a determination coefficient (R2) of 99.7% and an accuracy of 4.3%. The derived expression of the Ergun relation was obtained through an experimental apparatus consisting of a positive displacement pump controlled by an inverter, a regenerator from the 8Mag, a differential pressure reading at the inlet and outlet of the regenerator, and a volumetric flow meter. The pressure drop could be correlated with the volumetric flow rate. The corrective term was obtained from comparing the predicted pressure drop from Ergun using (II.7) with the velocity derived from the measured flow rates to the measured effective pressure drop. Therefore, this procedure led to an indirect measurement of the fluid flow rate by means of direct pressure measurements. Consequently, its accuracy depends on the quality of the pressure sensor data.

To estimate the regenerative performance, the regeneration factor δ_r introduced by Romero Gómez et al. (2013) was evaluated from:

$$\delta_r = \frac{\Delta T_{AMR}}{\Delta T_{ad}} \quad \text{(II.8)}$$

where ΔT_{ad} is the adiabatic temperature change of the MCM due to the maximum magnetic flux density change at the heat rejection temperature of the test.

ΔT_{ad} was estimated from data present in the scientific literature (Aprea and Maiorino, 2010; Bjørk, 2010b; Trevizoli et al., 2012). To define the

uncertainties of the indirectly measured quantities, an error propagation analysis was performed according to Moffat (1985), and the results are reported in Table II.4.

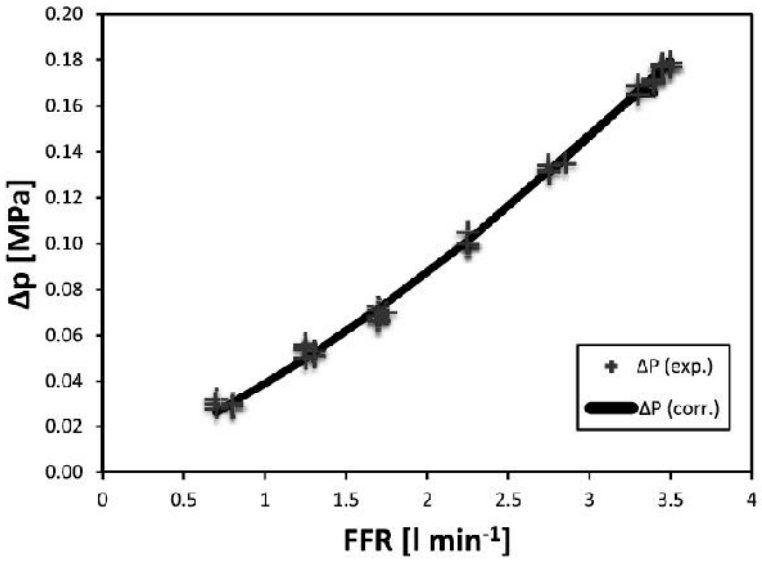

Figure II.9 *The modified Ergun correlation. Comparison between the experimental data (exp.) and predicted data from Eq. (II.6) (corr.).*

Table II.4 *Error propagation analysis. (*) It has been assumed depending both on the accuracy of the pressure gauges and on the accuracy of the correlation presented in Eq. (II.2). (**) The accuracy of ΔTad has been assumed depending both on the accuracy of the tesla meter and on the accuracy of the thermocouple.*

Dimension	Error
ΔT_{AMR}	±0.4 K
ΔT_{span}	±0.4 K
M_f (*)	±5.2 %
Φ	±5.3 %
δ_r	±4.5 %

II.2.2.2 Experimental results

Zero load tests have been conducted for the characterization of the device performances under no applied thermal load, while the refrigerant employed was gadolinium in packed bed configuration. Distilled water was employed as a regenerating fluid.

The tests were performed with the fluid flow rate fixed at 7 l/min, whereas the AMR cycle frequency was varied in the range 0.36 ÷ 1.79 Hz (0.18 ÷ 0.9 Hz shaft frequency) so that the utilization was in the range of 0.50 ÷ 2.72. The T_H was also varied over the range of 287 ÷ 302 K to characterize the performance sensitivity to the heat rejection temperature in the proximity of the refrigerant Curie temperature.

II.2.2.2.1 Pressure drop and utilization factor

Before estimating the pressure drop and utilization, an investigation of the rotary valve sealing was performed through indirect measurement.

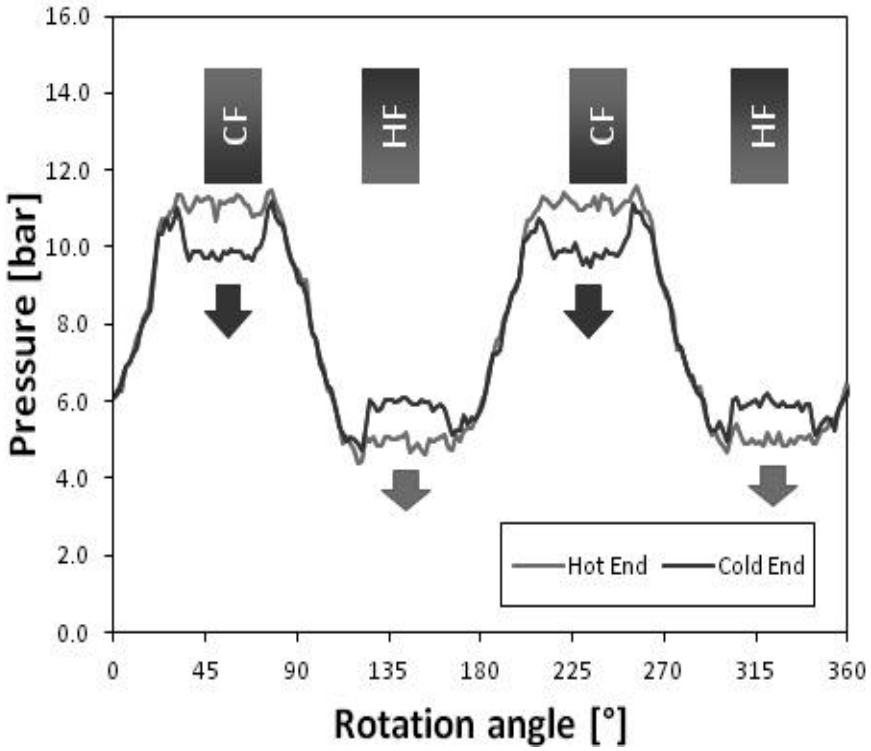

Figure II.10 *Sample of the pressure measurement at the ends of a regenerator as a function of the rotation angle (fluid flow rate = 7 l/ min and f_{AMR} = 0.71 Hz).*

Figure II.10 illustrates the pressure change at the ends of a regenerator during a complete cycle. During the fluid flow phases, a differential pressure is measurable across the regenerator, whereas during the transition phases (flow cut-off time) there is no pressure drop in the regenerators, suggesting that seal leakage, if existing, is sufficiently small that it cannot be detected through an indirect measurement based on pressure readings. As expected from the relatively low aspect ratio of the regenerators, their pressure drop is rather moderate, with a maximum value of 0.17 MPa during the blow phase.

Table II.5 reports the fluid flow rates and utilization for a range of operating frequencies. The maximum utilization of 2.83 was obtained at the minimum rotational speed of 10.8 rpm (0.18 Hz) that the controller was able to maintain without stalling the motor. The lowest utilization tested was 0.56 at 53.8 rpm (0.90 Hz). Because of the large dead volume between the regenerators and the valve ports (up to 130% of the volume of the refrigerant), utilization values well above the range suggested in literature (Tura and Rowe, 2011) are desirable for the characterization of the device performance.

Table II.5 *Utilization factor corresponding to the AMR cycle frequency at different T_H. The specific heat of gadolinium is assumed equal to 381 J/kg K.*

Φ [-]					
f_{AMR} [Hz]	302 [K]	298 [K]	295 [K]	291 [K]	287 [K]
0.36	2.68	2.72	2.64	2.65	2.60
0.54	1.79	1.84	1.73	1.74	1.76
0.72	1.34	1.40	1.31	1.31	1.31
1.08	0.89	0.93	0.90	0.87	0.87
1.79	0.54	0.56	0.55	0.50	0.53

II.2.2.2.2 Temperature span and regeneration factor

During the tests, the device experienced a maximum ΔT_{AMR} of 13.8 K, with the heat rejection temperature T_H set to 298 K, an AMR cycle frequency of 0.72 Hz, and the utilization factor of 1.40. Literature (Tura and Rowe, 2011; Romero Gómez et al., 2013; Lozano et al., 2013; Tagliafico et al., 2013) reports optimal utilization values closer to 0.5; however, as already noted, larger values are expected due to the current configuration being penalized by the large dead volumes. Larger utilizations typically have a negative impact on the temperature span and lower the T_H for which the maximum temperature span is achieved. This observation is in line with what has been observed with other devices, where with a utilization of half of 1.40 or less, the peak temperature span is observed with T_H well above 302 K. Figure II.11(a) illustrates the maximum ΔT_{AMR} detected for each tested AMR cycle frequency and T_H between 287 and 302 K, and Figure II.11(b) presents the same data with the ΔT_{AMR} as a function of utilization, ranging from 0.50 to 2.72.

Fig. II.12 shows the regeneration factor δ_r for each T_H as a function of the utilization. Whereas it is almost constant with utilizations up to 1.80, it decreases rapidly thereafter. This result is in accordance with the literature (Tura and Rowe, 2011; Engelbrecht et al., 2012; Gómez et al., 2013), confirming that best regeneration is obtained for lower utilizations. An appreciable difference between the ΔT_{AMR} and ΔT_{span} (ΔT_{loss}) is found with low utilizations, as illustrated in Fig. II.13.

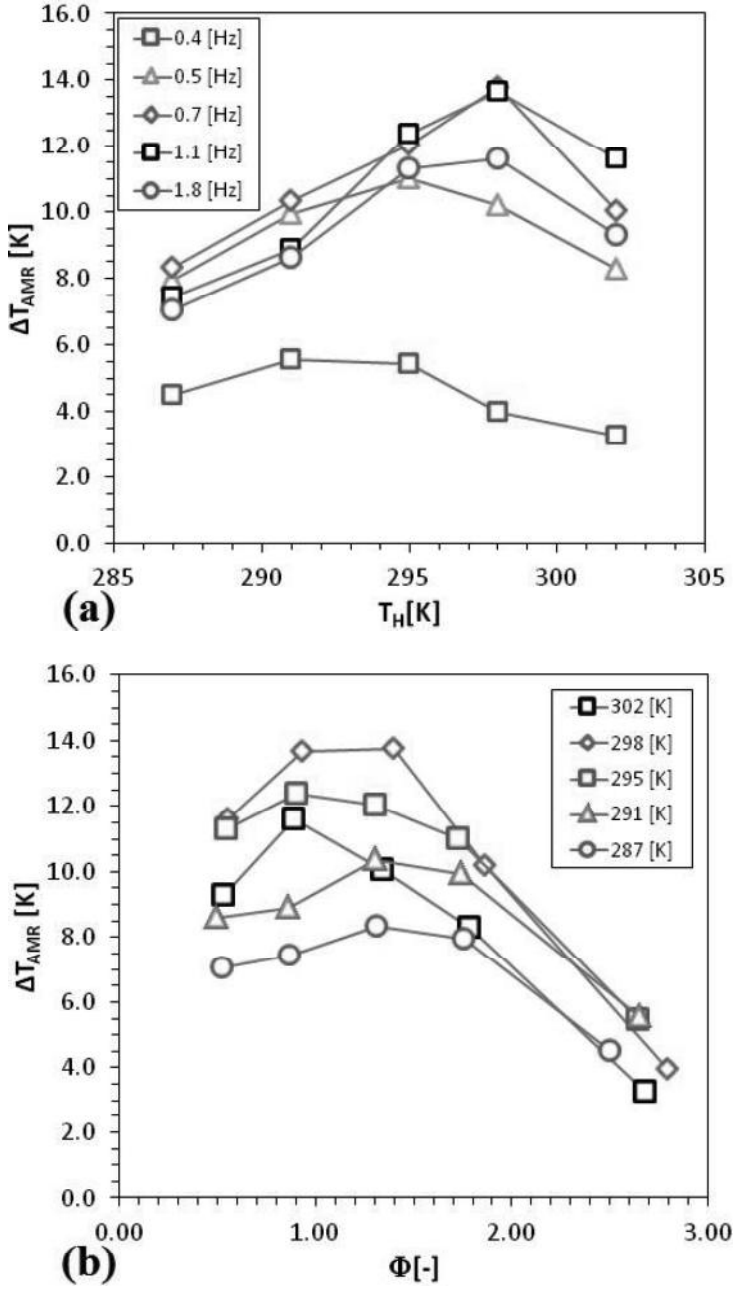

Figure II.11 *(a)ΔT_{AMR} as a function of the heat rejection temperature for different AMR cycle frequencies. (b)ΔT_{AMR} as a function of the utilization factor for different heat rejection temperatures.*

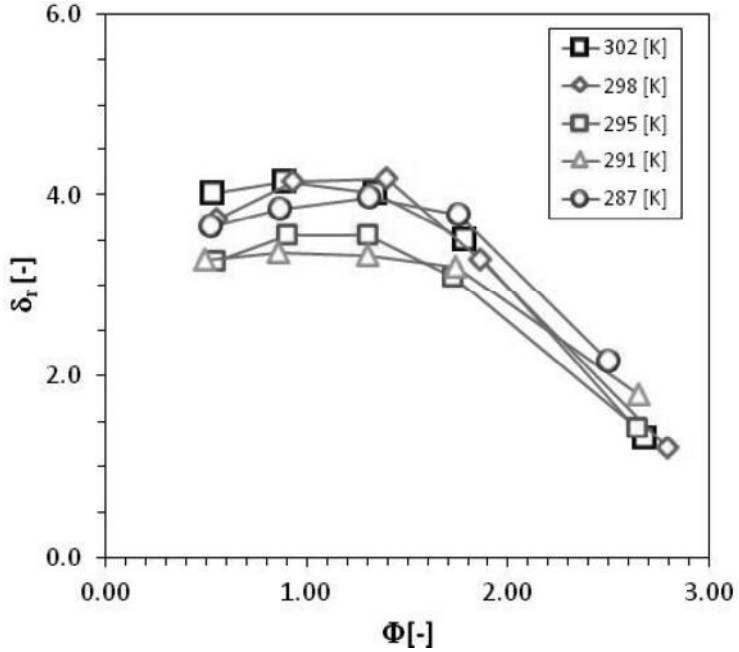

Figure II.12 *Regeneration factor as a function of the utilization factor for different heat rejection temperatures.*

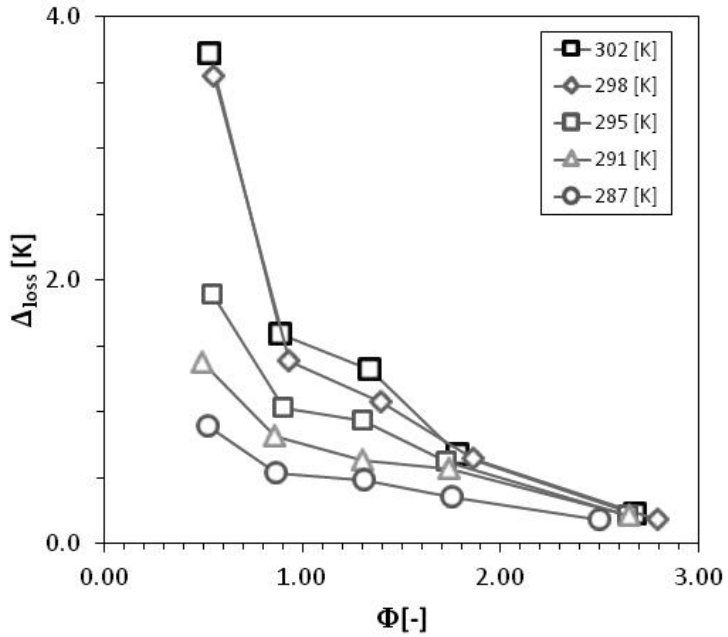

Figure II.13 *ΔT_{loss} as a function of the utilization factor for different heat rejection temperatures.*

In figure II.13, the results are related to T_H set to 298 K. For utilizations lower than 1.40, ΔT_{loss} increases to 3.5 K, whereas for larger utilizations, it tends toward 0. This shows that when the fluid flow rate is kept constant and the operating frequency is high, the dead volumes could have an influence on the performance of the device because a larger portion of the displaced fluid volume is trapped in the volume between the regenerators and the rotary valve.

II.2.2.3 Considerations

The device produces a maximum ΔT_{span} under no thermal load of 13.5 K with a heat rejection temperature T_H of 298 K and utilization of 1.40. Some efficiency loss was observed at low utilization when the difference between ΔT_{AMR} and ΔT_{span} becomes appreciable, whereas for larger utilizations, it tends toward 0. Although the performance is low, largely due to thermal losses, the device operates as planned. In particular, the magnetic assembly provides an intense magnetic flux density in a large volume, and the rotary valve has been demonstrated to work effectively as a fluid manifold and field generator drive shaft.

II.2.3 The energy performances investigation

For defining the operating limits of 8Mag, which requires further experimental investigation, other tests have been scheduled to study the energy performance of 8Mag in terms of refrigeration power, energy losses, and COP. Therefore, in this section are reported the device performances under the application of different cooling load, in order to carry out the RPMMR's answer in terms of cooling power and coefficient of performance (COP).

II.2.3.1 Experimental results: campaign 1

A number of tests were conducted (Aprea et al., 2016c) for the characterization of the device performances. All of them were performed using gadolinium spheres as the refrigerant and distilled water as an auxiliary regenerating fluid. To reduce the influence of the temperature of the air surrounding the device, the connecting pipes between the heat exchangers and the magnetic refrigerator were insulated. Moreover, as suggested by Engelbrecht et al. (2012), during all of the tests, the magnetic refrigerator was introduced into a climatic room, where the air temperature was maintained in a small range between 293 and 298 K and the relative humidity was equal to 50% ± 5%. As noticed by Tušek et al. (2013), the fluid flow rate affects the performance of a magnetic refrigerator; consequently, the 8Mag performances have been carried out at three different fluid flow rates: 5.0, 6.0 and 7.0 l/min. In accordance with the

literature (Eriksen et al., 2015; Lozano et al., 2014), all the tests were performed while keeping the hot side temperature at approximately the Curie temperature. In particular, T_H was fixed at 296 K. Consequently, for each fluid flow rate, a series of tests were conducted while varying the AMR cycle frequency (f_{AMR}) and the thermal load.

The Φ values, related the experimental tests reported in this section, were evaluated according to the procedure identified in section II.2.2.1. Starting from a condition of no load applied, for each AMR cycle frequency, the thermal load was increased step by step. For each test, the following expected steady-state conditions were achieved: the temperature span change was less than the measurement accuracy for a time longer than 300 s.

The experimental pressure losses through the overall device were almost constant for each fluid flow rate value, as reported in Table II.6.

Table II.6 *Pressure drops at different fluid flow rates.*

Fluid flow rate [l/min]	Pressure drop [kPa]
5	530÷548
6	603÷617
7	941÷956

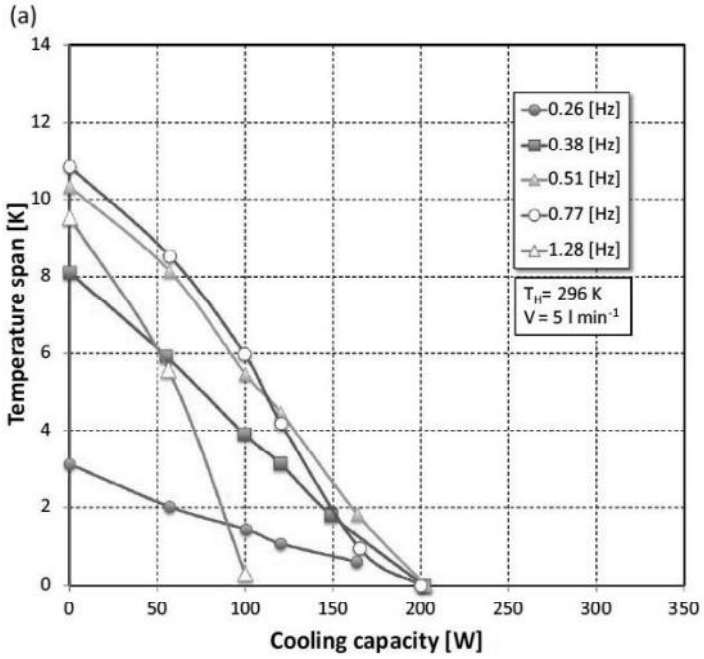

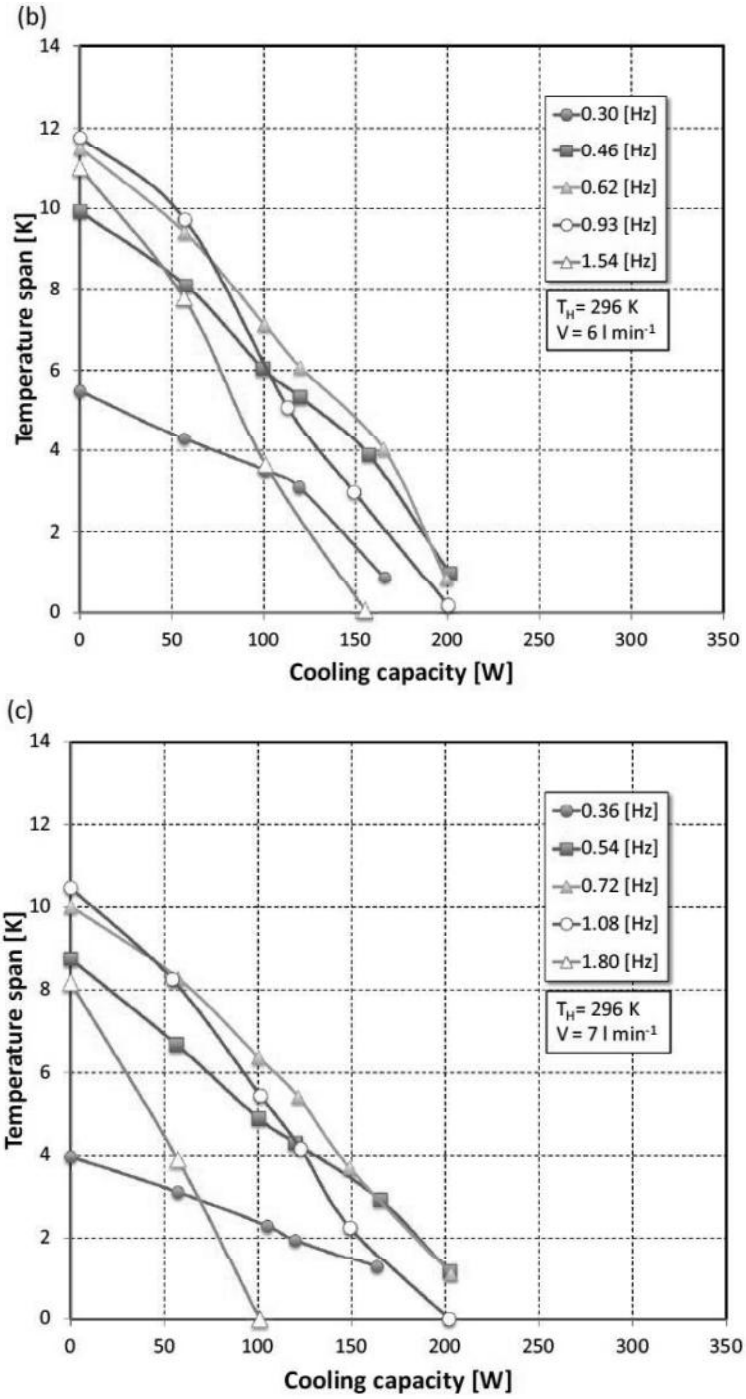

Figure II.14 *(a,b,c)* ΔT_{span} *as a function of the thermal load for different frequencies and different fluid flow rates.*

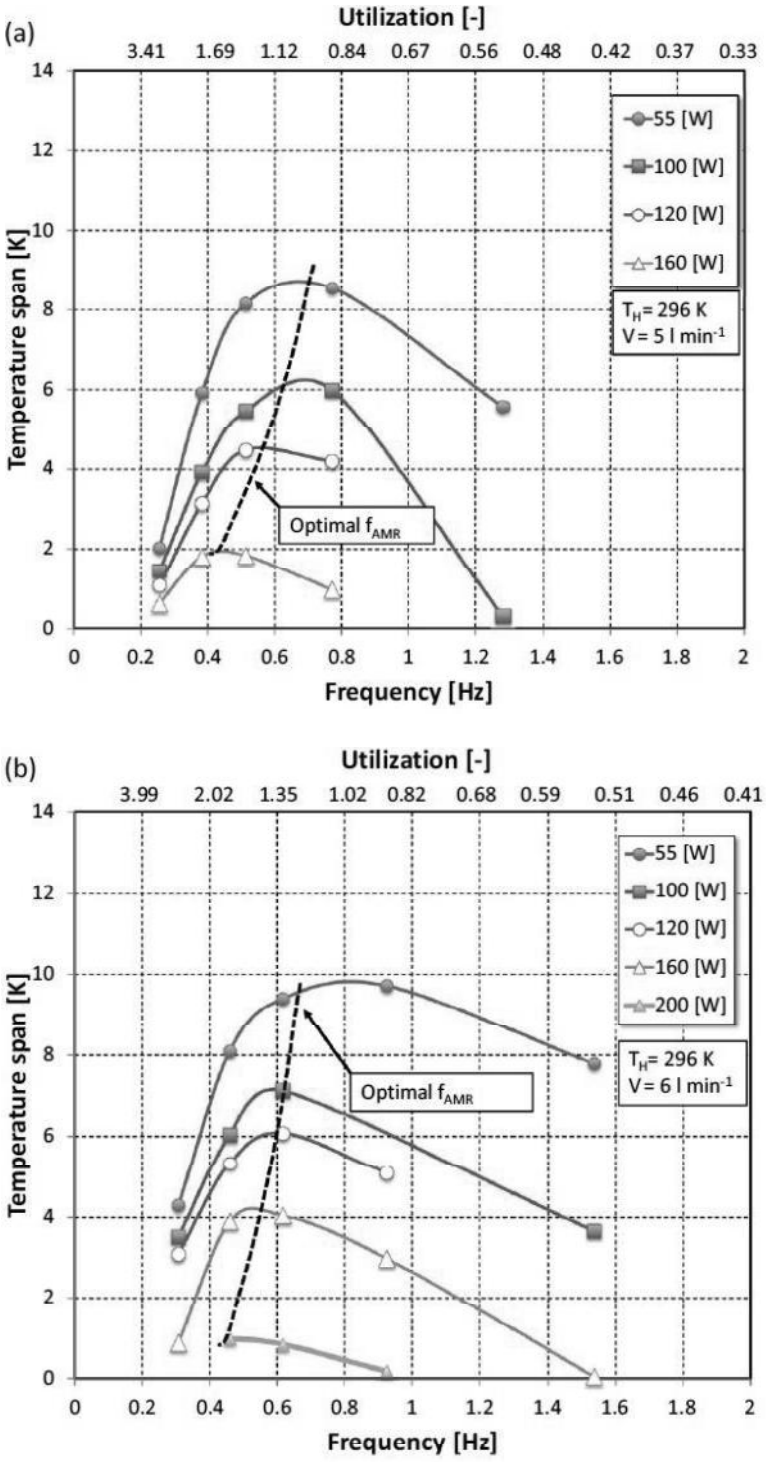
(a)
Utilization [-]
3.41 1.69 1.12 0.84 0.67 0.56 0.48 0.42 0.37 0.33
Temperature span [K]
Frequency [Hz]
55 [W]
100 [W]
120 [W]
160 [W]
T_H= 296 K
V= 5 l min-1
Optimal f_AMR
(b)
Utilization [-]
3.99 2.02 1.35 1.02 0.82 0.68 0.59 0.51 0.46 0.41
Temperature span [K]
Frequency [Hz]
55 [W]
100 [W]
120 [W]
160 [W]
200 [W]
T_H= 296 K
V= 6 l min-1
Optimal f_AMR

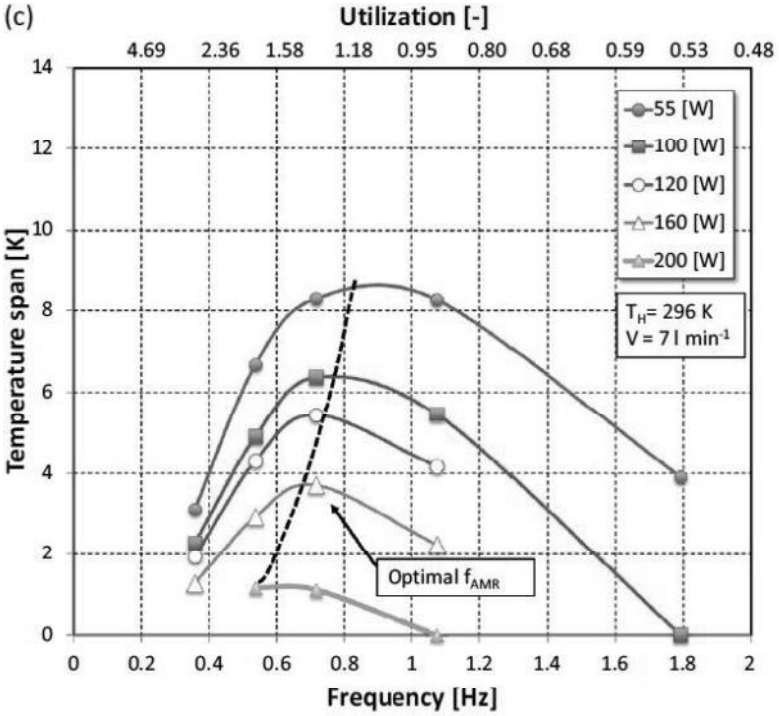

Figure II.15 *(a,b,c) ΔT_{span} as a function of f_{AMR} for different thermal loads and different fluid flow rates.*

From figure II.14, which shows ΔT_{span} as a function of the thermal load for different frequencies f_{AMR} at fluid flow rates of 5.0, 6.0 and 7.0 l/min at T_H equal to 296 K, it is appreciable that at a fixed frequency, ΔT_{span} decreases as the cooling capacity increases. This behaviour, which is in accordance with some works (Lozano et al., 2014; Tura and Rowe, 2011; Tušek et al., 2013), is due to the thermal load supplied at the cold side of the regenerator. The maximum temperature span corresponds to the zero load tests and is 10.9 °C (at f_{AMR} = 0.77 Hz and $\dot{V}$ = 5.0 l/min), 11.9 °C (at f_{AMR} = 0.93 Hz and $\dot{V}$ = 6.0 l/min) and 10.5 °C (at f_{AMR} = 1.08 Hz and $\dot{V}$ = 7.0 l/min). The maximum refrigeration power reached by 8Mag corresponds to a ΔT_{span} close to 0 K and is approximately 200W. Furthermore, in figure II.14, is possible to note that the iso-frequency lines cross over each other at a certain point. This behaviour is better shown in figure II.15, where we have reported the temperature span for different thermal load values as a function of cycle frequency. The top axis of the graphs gives the corresponding Φ. It is easy to appreciate that for each thermal load value, there is an optimal cycle frequency for which ΔT_{span} is maximized.

As noticed by Lozano et al. (2014), this phenomenon happens because at low frequencies, there is a large influence of the longitudinal thermal conduction and the regenerator utilization factor becomes too high.

However, at lower frequencies, the temperature span increases with increasing frequency until a certain optimum frequency, at which the irreversible losses (friction inner to the rotary valve, bad fluid distribution inside the regenerators) and the dead volumes become significant and the heat transfer is affected; thus, the regenerator is not capable of maintaining a high temperature span. At a higher cycle frequency, the fluid is not capable of utilizing all the energy available from the magnetocaloric effect, thus lowering the maximum temperature span. Meanwhile, at an excessive cycle frequency, the fluid is not able to utilize all the energy available from the magnetocaloric effect, thus lowering ΔT_{span}.

In addition, during our experimentation we have observed that for each fluid flow rate the optimal cycle frequency decreases as the thermal load increases. We can explain this phenomenon considering that keeping constant the fluid flow rate a decrease of cycle frequency leads to an increase of the total mass flowing through the regenerators. This involves an increase of the utilization and then the device can absorb a greater thermal load. Consequently, to maximize the temperature span, similarly to other devices (Bahl et al., 2014; Russek et al., 2010; Tura and Rowe, 2011) 8Mag must work at the optimal cycle frequency. For all the experimental tests, the optimal frequency falls in the range between 0.4 and 0.8 Hz, corresponding to an optimal utilization factor between 2.36 and 1.18.

Figure II.14 and figure II.15 also show that at fixed thermal load and frequency, the best ΔT_{span} is achieved for a fluid flow rate of 6.0 l/min. Therefore, there is an optimum fluid mass flow rate that leads to the largest temperature span at each operating frequency. If the regenerating fluid flow rate is small, only part of the energy generated by the magnetocaloric effect can be utilized. With a greater value of fluid flow rate, the fluid can utilize the entire energy available. Further fluid flow perturbs the temperature profile of the AMR, decreasing the temperature difference between the fluid and the bed. The bed quickly becomes overwhelmed by the fluid flow and the efficiency of the heat transfer decreases.

Figure II.16 reports the cooling capacity as a function of temperature span at a fixed T_H (296 K) and Φ (1.76) for the three different fluid flow rates and corresponding cycle frequencies (5.0 l/ min at 0.38 Hz, 6.0 l/min at 0.46 Hz and 7.0 l/min at 0.54 Hz). The figure II.16 clearly shows that the cooling capacity decreases when the temperature span increases. In addition, it is notable that for a fixed ΔT_{span} an increase of the water mass flow rate improves the cooling capacity due to the increase of the heat transfer coefficient. The refrigeration power ranges between 200W (at an almost zero ΔT_{span}) and 50W (at a ΔT_{span} between 6 and 6.7 K).

Fig. II.17 presents the torque as a function of the temperature span at a fixed T_H (296 K) and Φ (1.76) for the three different fluid flow rates and corresponding cycle frequencies (5.0 l/min at 0.38 Hz, 6.0 l/min at 0.46 Hz and 7.0 l/min at 0.54 Hz). The mechanical torque due to the rotation of the

magnetic system is measured directly at the shaft of the drive system and considers the mechanical power required to rotate the magnets and the magnetic work. Figure II.17 clearly shows that the torque increases with the temperature span together with the magnetic work at a fixed frequency and fluid flow rate. In particular, a maximum value of 29 N m was measured at the maximum temperature span of 6.7 K. It is possible to attribute the increase of the mechanical torque with the temperature span to the second order transition phase of the gadolinium. A high temperature span causes a greater mass of magnetocaloric material to have a ferromagnetic behaviour; consequently, the magnetic work and then the mechanical torque increase.

The torque, at a fixed temperature span, increases as the fluid flow rate and frequency increase. Indeed, increasing the fluid flow rate also increases the cycle frequency to make a comparison at fixed Φ. The rotating magnetic field induces eddy currents in the regenerator that generate forces that oppose the changing magnetic field, thus increasing the magnetic work.

The strength of this term increases with frequency. Furthermore, mechanical frictions also increase with the frequency. Moreover, as underlined in section II.2.2.2.1, a significant dead volume between the regenerators and the valve ports affects the performance of 8Mag. The negative effect of dead volume increases with the frequency.

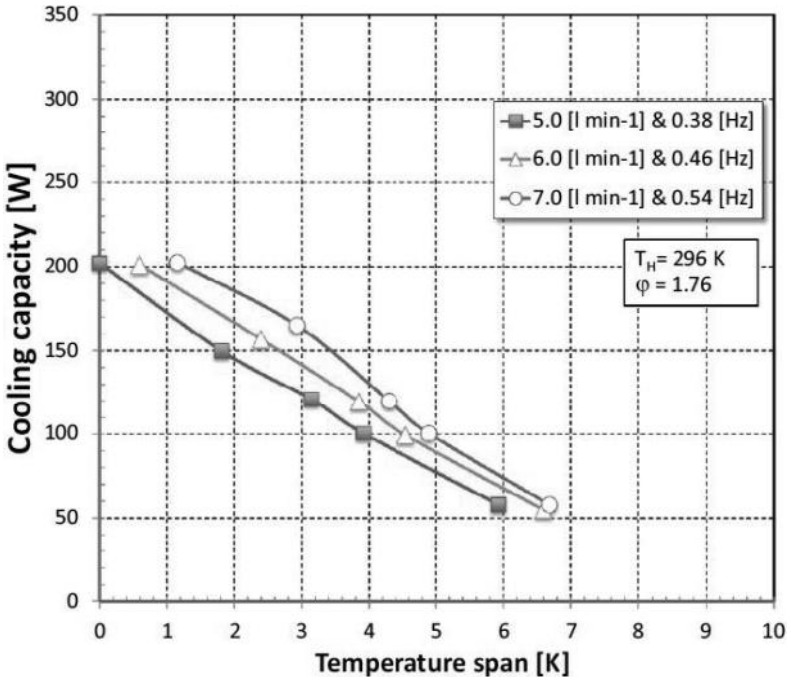

Figure II.16 *$\dot{Q}_{ref}$ as a function of ΔT_{span} for three different couples of fluid flow rate and f_{AMR} corresponding to the same utilization factor.*

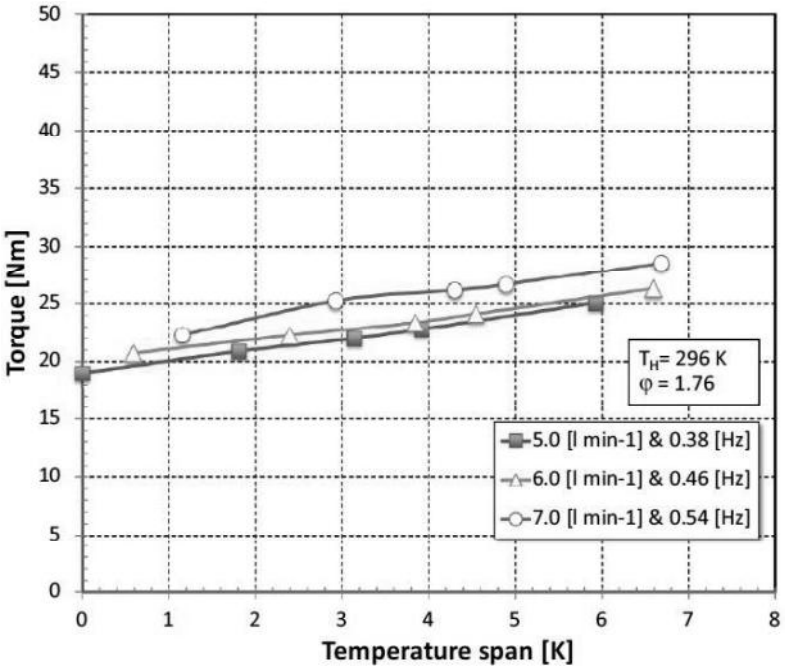

Figure II.17 *The mechanical torque as a function of ΔT_{span} for three different couples of fluid flow rate and f_{AMR} corresponding to the same utilization factor.*

Figure II.18 presents COP as a function of ΔT_{span} at fixed T_H (296 K) and Φ (1.76). At a fixed frequency and fluid flow rate, COP decreases with the temperature span. Indeed, as ΔT_{span} increases, the cooling power decreases and the torque increases. At a fixed temperature span, the COP increases as the fluid flow rate and cycle frequency decrease, reaching the maximum value of 2.5 at 0 ΔT_{span}. The reason for this increase is related to both the decrease of the fluid flow and the concurrent decrease of the cycle frequency. The first effect leads to a decrease of the pressure drops and therefore of the work of the pump. The second effect leads to a decrease of both mechanical and eddy current losses.

Figure II.19 reports COP as a function of the cooling power at fixed T_H (296 K) and Φ (1.76). Here, it is clearly shown that COP increases with the cooling capacity. Indeed, as shown in Eq. II.7, the COP is directly proportional to the cooling capacity and inversely proportional to the electrical power absorbed by the pump and by the electrical motor. Indeed, increasing the thermal load at a fixed fluid flow rate does not change $\dot{W}_{el,p}$. Since Fig. II.17 shows that the torque decreases with the temperature span, therefore, since increasing the thermal load decreases the temperature span, $\dot{W}_{el,m}$ decreases. The best value of the COP is 2.5, corresponding to a thermal load of 200 W.

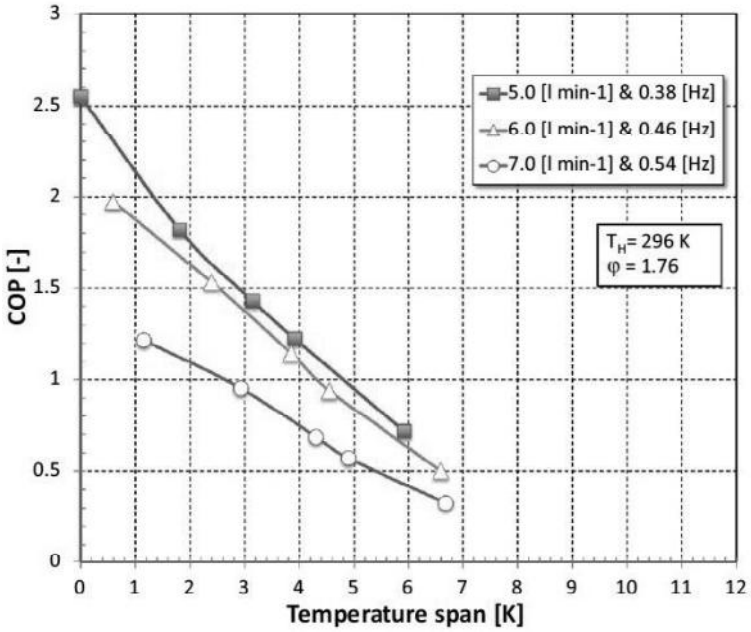

Figure II.18 *COP as a function of ΔT_{span} for three different couples of fluid flow rate and f_{AMR} corresponding to the same utilization factor.*

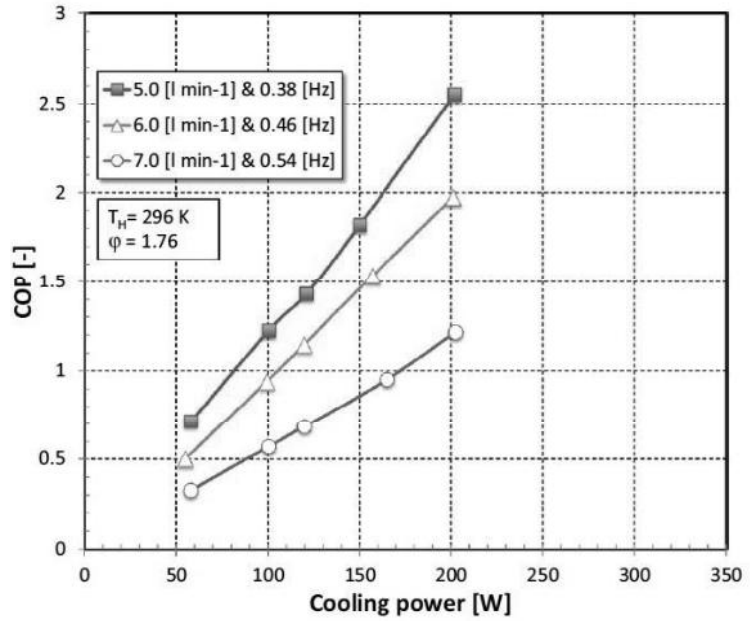

Figure II.19 *COP as a function of $\dot{Q}_{ref}$ for three different couples of fluid flow rate and f_{AMR} corresponding to the same utilization factor.*

II.2.3.2 Experimental results: campaign 2

To obtain additional data characterizing the energy performances of 8Mag, another campaign of tests (campaign 2), has been conducted (Aprea et al., 2016d), working in the optimal frequency with respect to the hot reservoir temperatures considered. A number of tests were carried out for further characterization of the energy performances of 8Mag. All the them were performed employing, as in campaign 1, gadolinium in packed-bed configuration as refrigerant and distilled water as auxiliary regenerating fluid. The RPMMR performances with variable cooling load have been tested by the application of different cooling power at fixed fluid flow rate (0.083 kg/s, i.e. 5 l/min) and at a fixed cycle frequency of 0.5 Hz, which is the optimal value for T_H = 22°C. The hot temperature reservoir T_H was kept constant at two different temperatures of 22 °C and 32 °C. Figure II.20 clearly shows that at fixed T_H, the thermal load decreases increasing ΔT_{span}. This behavior, which is in accordance with other works (Lozano et al., 2014; Tušek et al., 2013), is due to the thermal load supplied at the cold side of the regenerator. The maximum temperature span corresponds to zero load tested, and it has an amount of 8.75 °C for T_H = 32 °C and 11.3 °C for T_H = 22 °C. At fixed thermal load, the temperature span at T_H = 22 °C is always higher than that at T_H = 32 °C. Indeed, corresponding to T_H = 22 °C tests, the average temperature of the regenerator is closer, than the other item, to the Curie temperature of Gd where the magnetocaloric effect is maximum.

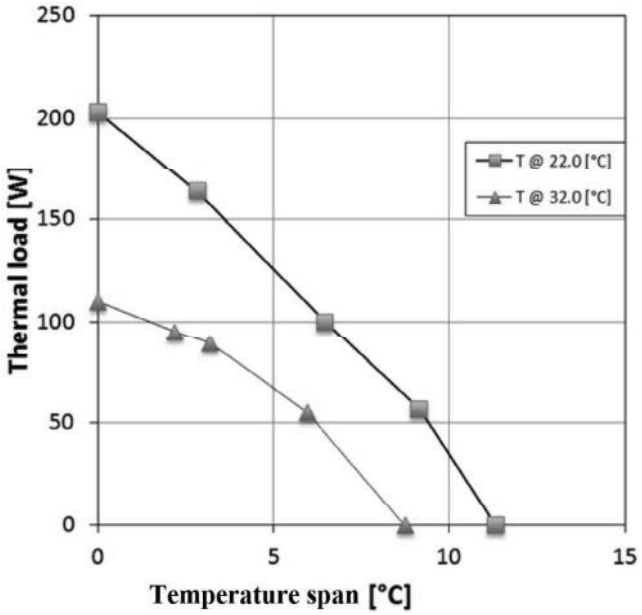

Figure II.20 *Cooling power as a function of temperature span for two different hot reservoir temperatures.*

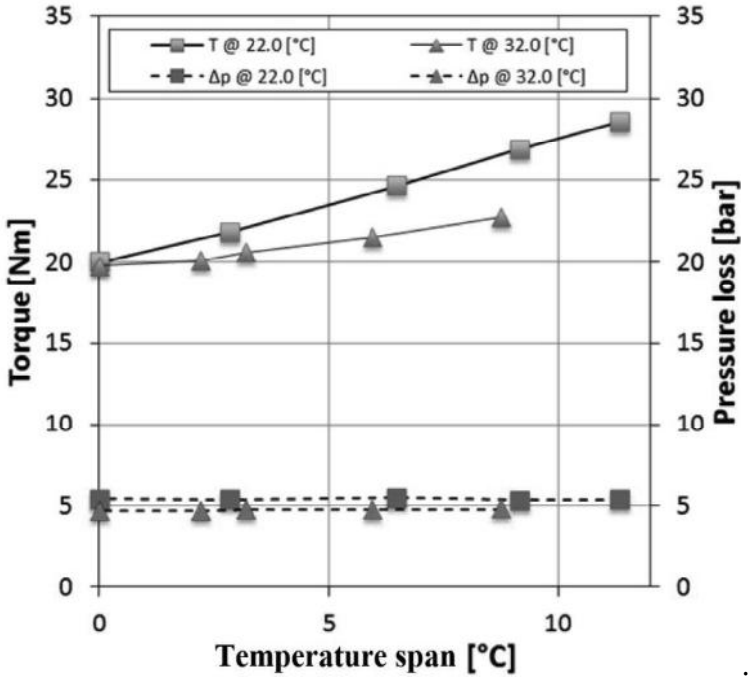

Figure II.21 *Torque and pressure loss as a function of temperature span.*

In figure II.21, the torque and the pressure losses through the overall device as a function of the temperature span are reported. The mechanical torque, due to the rotation of the magnetic group, is measured directly at the shaft of the drive system, and it takes into account the magnetic work and the mechanical power required to rotate the magnets. Figure II.21 clearly shows that the torque increases with the temperature span. A maximum peak-to-peak value of 28 Nm has been measured at the maximum temperature span of 11.3 °C. The increase of the mechanical torque with ΔT_{span} is easily attributable to the second order transition phase of gadolinium. A high temperature span causes a greater mass of magnetocaloric material to have a ferromagnetic behavior; consequently, the magnetic work and then the mechanical torque increases. The pressure losses are rather moderate, with an almost constant value of 5 bar. The reason why pressure losses are quite constant is probably to be found in the detail that the flow rate of the fluid is constant in both the reported tests.

Fig. II.22 reports the COP as a function of the thermal load. The COP increases with the thermal load, reaching a maximum value of 1.8 under a thermal load of 163 W for T_H = 22 °C and 1.18 under 95 W for T_H = 32 °C. Indeed, since the COP is directly proportional to the cooling capacity and inversely proportional to the work absorbed by the pump and by the motor, increasing the thermal load at a fixed fluid flow rate does not change $\dot{W}_{el,p}$.

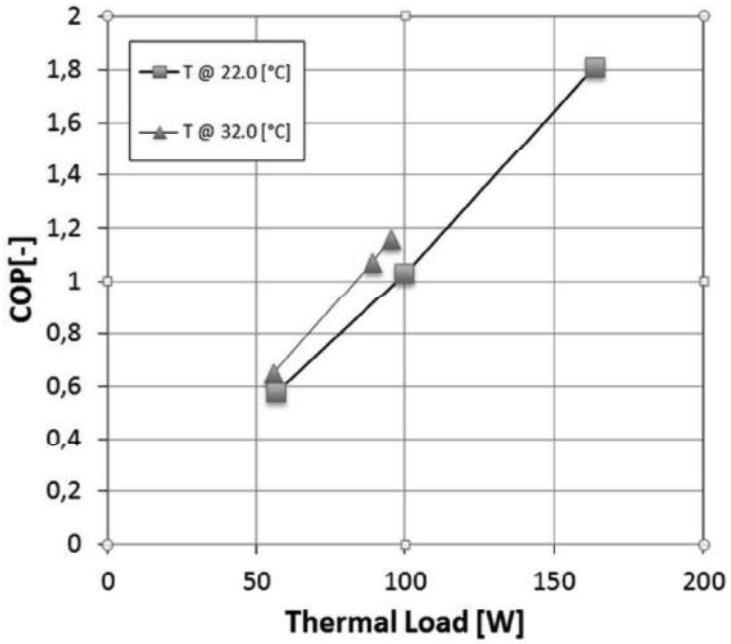

Figure II.22 *COP as a function of thermal load for two different hot reservoir temperature.*

II.2.3.3 Considerations about the energy performances investigations

To characterize the energy performances of 8Mag, it has been performed various tests under different operating conditions.

In campaign 1, it has been tested the behavior of 8Mag by changing both the cycle frequency and the fluid flow rate while the hot side temperature was fixed at 296 K. For each test, it has been measured ΔT_{span}, the cooling capacity, the mechanical torque and the COP. Regarding ΔT_{span}, it is worth noting that it has been reported a pessimistic measurement. Indeed, it has been measured the actual ΔT_{span} available at the ends of the device, including the thermal losses typical of the RPMMR. The tests have shown, at 296 K, a maximum temperature span at the zero load tests of 11.9 °C (at f_{AMR} = 0.93 Hz and $\dot{V}$ = 6.0 l/min) and a maximum COP of 2.5 corresponding to a thermal load of 200 W (at f_{AMR} = 0.38 Hz and $\dot{V}$ = 5.0 l/min). Moreover, for each condition, 8Mag exhibits an optimal f_{AMR}, for which it is possible to maximize ΔT_{span}.

In campaign 2, the device works under a variable cooling load, at fixed fluid flow rate of 0.083 kg/s and AMR cycle frequency of 0.5 Hz, which is the optimal frequency. The device produces a maximum temperature span under zero thermal load of 11.3 °C and 9.15 °C under 57 W. The maximum

COP is 1.8 with a heat load of 163 W for T_H = 22 °C, whereas it is 1.18 under 95 W for T_H = 32 °C.

As a result of the experimental analysis, it has been observed that the behavior of 8Mag is in accordance with those of other devices built (Dikeos and Rowe, 2013; Russek et al., 2010; Gao et al., 2006; Eriksen et al., 2015; Balli et al., 2012) around the world. Furthermore, considering that 8Mag offers a reduction of thermal losses, it is possible to assert conclude that the tests presented here show promising performances. Although it is clearly visible that these results can be easily overcome by vapor compression systems, the device met the objectives of (1) continuous cooling, (2) simple operation mode, (3) compact design of the machine, (4) wide range of operating conditions, (5) high operation frequencies and (6) intense magnetic flux. To improve the prototype, new experimental tests focused on the identification of the worst causes of energy losses have been scheduled.

Chapter III
A two-dimensional model of an active magnetic regenerator

III.1 Introduction

This chapter introduces a two-dimensional model of an active magnetic regenerator operating at room temperature. The model has been developed, as a primary purpose, to be able to reproduce the behavior of one of the regenerator of the RPMMR, described in chapter 2. To this aim, the model has been experimentally validated (Aprea et al., 2015a) with experimental results provided by the prototype. This model is used to optimize the experimental device and to identify significant areas of device improvement. Thus, it has been used to explore the critical aspects of 8Mag and to outline the way to improve performance.

Anyway, the model can be easily generalized to consider different device geometries, temperature spans, secondary fluids, and magnetic materials. To this aim, the model has been tested when employing new magnetocaloric materials (Aprea et al., 2015b), whose performance have been also compared (Aprea et al., 2015c), from an environmental point of view, with the ones of a commercial vapor-compression refrigerator working with R134a. Moreover, additional investigations have been conducted to explore the behavior of the regenerator with a parallel-plate configuration (Aprea et al., 2016b), employing a number of different magnetocaloric materials.

III.2 Model description

III.2.1 Regenerator geometry

The geometry of the regenerator presented in the model corresponds to one of the eight beds of the 8Mag along the x and y directions. The 8Mag regenerators are all packed bed operating at room temperature and composed

of spherical gadolinium particles, while the regenerating fluid is demineralized water.

As clearly visible in figure III.1, the regenerator has a rectangular shape with a height of 20mm and a length of 45mm. The area of the regenerator is filled with a regular matrix of 3600 circles that constitute the packed bed; every circle has a diameter of 0.45mm and the amount of the area occupied by all of the circles is 63% of the total rectangular area. Stacking particles in the regenerator area form a group of channels: the fluid flows through these interstitial channels.

The fluid flows in a positive x direction during the isofield cooling process and in the opposite direction during the isofield heating process.

The assumptions for the porous region of the AMR are as follows:

- the magnetic material is isotropic and the magnetic particles are rigid spheres of the same diameter;
- the thermal radiation is neglected;
- the void fraction within the packed bed is uniform;
- the external surface of the packed bed is perfectly insulated.

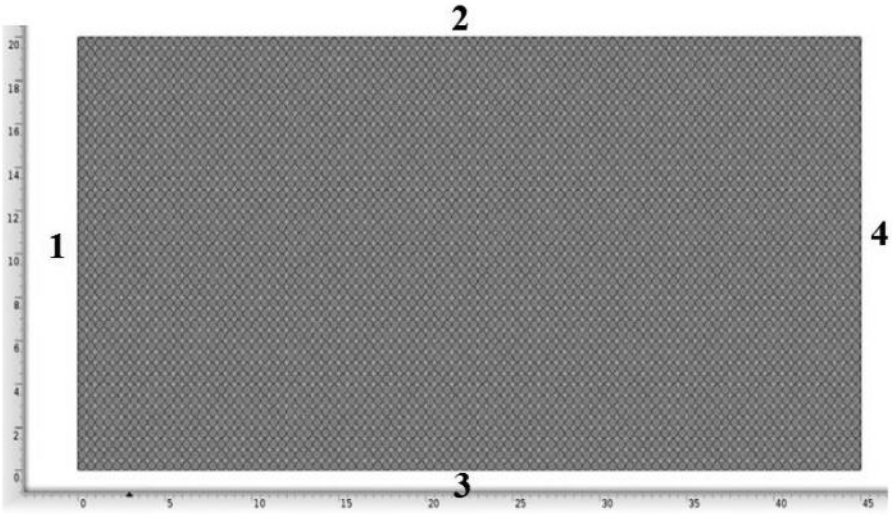

Figure III.1 *The packed bed AMR regenerator geometry: a 20x45mm^2 wrapper contains 3600 spheres.*

III.2.2 Mathematical formulation

Following the mathematical background in literature (Oliveira et al., 2012; Velazquez et al., 2014; Lionte et al., 2015), the mathematical formulation that describes the AMR cycle includes several distinct groups of equations according to the different processes of the AMR cycle that the regenerator experiences.

A two-dimensional model of an active magnetic regenerator

The equations that rule the regenerative fluid flow processes in both directions are the Navier-Stokes equations for the fluid flow and the energy equations for both the fluid and the solid particles.

Assuming the fluid incompressible, the viscous dissipation is neglected due to low mass flow; the above equations can be written as follows:

$$\begin{cases} \dfrac{\partial u}{\partial x}+\dfrac{\partial v}{\partial y}=0 \\ \dfrac{\partial u}{\partial t}+u\dfrac{\partial u}{\partial x}+v\dfrac{\partial u}{\partial y}=-\dfrac{1}{\rho_f}\dfrac{\partial p}{\partial x}+\nu\left(\dfrac{\partial^2 u}{\partial x^2}+\dfrac{\partial^2 u}{\partial y^2}\right) \\ \dfrac{\partial v}{\partial t}+u\dfrac{\partial v}{\partial x}+v\dfrac{\partial v}{\partial y}=-\dfrac{1}{\rho_f}\dfrac{\partial p}{\partial y}+\nu\left(\dfrac{\partial^2 v}{\partial x^2}+\dfrac{\partial^2 v}{\partial y^2}\right) \\ \dfrac{\partial T_f}{\partial t}+u\dfrac{\partial T_f}{\partial x}+v\dfrac{\partial T_f}{\partial y}=\dfrac{k_f}{\rho_f C_{f,p}}\left(\dfrac{\partial^2 T_f}{\partial x^2}+\dfrac{\partial^2 T_f}{\partial y^2}\right) \\ \dfrac{\partial T_s}{\partial t}=\dfrac{k_s}{\rho_s C_{s,p}}\left(\dfrac{\partial^2 T_s}{\partial x^2}+\dfrac{\partial^2 T_s}{\partial y^2}\right) \end{cases} \quad \text{(III.1)}$$

where ρ_f and ρ_s are respectively the fluid and the solid density; u and v are the fluid velocities along the x and the y directions; p and μ_f are the pressure and the dynamic viscosity of the fluid; $C_{f,p}$ and $C_{s,p}$ are respectively the fluid and the solid heat capacity at constant pressure; k_f and k_s the thermal conductivity of the fluid and the solid; T_f and T_s the fluid and the solid temperatures.

The fluid has sufficiently low speed to be considered laminar, so turbulent flow equations are not required. The flow is single phased and there is no surface tension because the fluid, even when not flowing always surrounds the solid particles. The solid and the fluid temperature are strictly related and constantly evolving during the entire AMR cycle.

The equations that model the magnetization and demagnetization process of the cycle must account for the MCE that elevates or reduces the temperature of the solid by the variation of the external magnetic field applied to the regenerator. Therefore, the MCE temperature variation ΔT_{ad} is converted into a heat source term (Bouchard et al., 2005; Bouchard et al., 2009):

$$Q = Q(B,T_S) = \frac{\rho_s C_{s,p}(B,T_s)\Delta T_{ad}(B,T_s)}{\Delta t} \quad \text{(III.2)}$$

where Δt is the time period of magnetization/demagnetization process.

This term has the dimensions of power density [W/m^3] and it is included in the energy equation of solid, for magnetization and the demagnetization phases, as follows:

$$\rho_s C_{s,p} \frac{\partial T_s}{\partial t} = k_s \left(\frac{\partial^2 T_s}{\partial x^2} + \frac{\partial^2 T_s}{\partial y^2} \right) + Q \tag{III.3}$$

The term Q is positive during magnetization and negative during demagnetization. Therefore, the equations that govern the magnetization and the demagnetization phases are:

$$\begin{cases} \rho_f C_{f,p} \frac{\partial T_f}{\partial t} = k_f \left(\frac{\partial^2 T_f}{\partial x^2} + \frac{\partial^2 T_f}{\partial y^2} \right) \\ \rho_s C_{s,p} \frac{\partial T_s}{\partial t} = k_s \left(\frac{\partial^2 T_s}{\partial x^2} + \frac{\partial^2 T_s}{\partial y^2} \right) + Q \end{cases} \tag{III.4}$$

III.2.3 Boundary conditions

The boundary conditions are not consistent during the entire AMR cycle; some of them change according to the different phases of the cycle. In the following, the boundary conditions for each process are described in detail and illustrated with reference to figure III.1.

III.2.3.1 Adiabatic magnetization/demagnetization

During the adiabatic magnetization and demagnetization processes, the fluid is stationary; thus, thermal insulation is applied on all the regenerator walls (boundary 1,2,3,4):

$$-\hat{\boldsymbol{n}} \cdot (-k \boldsymbol{\nabla} T) = 0 \tag{III.5}$$

III.2.3.2 Cold-to-hot fluid flow

The boundary condition for modeling fluid velocity and direction requires the construction of a velocity vector **u** that is positive during the cold-to-hot fluid flow process and negative when fluid flows in hot-to-cold direction.

Thermal insulation is imposed on the boundaries 2,3,4 of the regenerator whereas on the left one (boundary 1) the presence of the cold heat exchanger is modeled by the imposition of its temperature:

$$T = T_C \tag{III.6}$$

III.2.3.3 Hot-to-cold fluid flow

The boundary condition for modeling fluid velocity and direction requires that **u** vector is negative with respect to the cold-to-hot direction.

Thermal insulation is imposed on the boundaries 1,2,3 of the regenerator, whereas at the right one (boundary) the presence of the hot heat exchanger is modeled by the imposition of its temperature:

$$T = T_H \tag{III.7}$$

III.2.4 Modeling the magnetocaloric refrigerant and its MCE

To reproduce the behavior of the magnetocaloric refrigerant it is required to implement its magnetocaloric effect in the model. To do that, as mentioned before, a Q term is introduced in the energy equation of the solid, whom represent a heat source (positive) during magnetization and a sink (negative) during demagnetization. The Q, which has the dimensions of a power density [W/m^3], is proportional to the MCE temperature variation ΔT_{ad} and the specific heat at a constant pressure, which are both dependent on the initial solid temperature T_S and the magnetic flux density B. Therefore, a mathematical expression for Q and C_p is required, as the final solution to be implemented in the model.

As first step, the magnetic properties of the magnetocaloric refrigerant have been evaluated by interpolating experimental data available from existing literature. Based on the construction of a table function that describes C_p and Q as a range of temperature and magnetic field intensity, and with the help of a mathematical function finder software, the corresponding mathematical expression can be found for both the magnetization and demagnetization processes.

III.2.5 Numerical procedure

The coupled equations that govern the AMR cycle, described in section III.2.2, are solved by means of the Finite Element Method through the software COMSOL Multiphysics, whom is able to solve problems by coupling different physics. In particular, equations (III.1) and (III.4) are solved for each thermodynamic step of the AMR cycle. With the aim to carry out the entire thermodynamic cycle, the steps have been simulated in accordance with the order defined for the AMR cycle. First, the magnetization: the magnetic field is applied on the regenerator and it generates the MCE which elevates the temperature of the magnetocaloric refrigerant. Second, fluid flows in the cold-to-hot direction with the magnetic field still effective. Third, the demagnetization: the magnetic field is removed from the regenerator and the consequent variation of field intensity generates the MCE which reduces the temperature of the solid refrigerant. Four, fluid flows in the hot-to-cold heat exchanger in zero magnetic field. For this purpose, the initial condition of each thermodynamic step is the last condition of the preceding one, so that a time-based sequential

condition can be applied. The same time step, Δt, is chosen for the resolution during all four periods of the cycle. The cycle is repeated several times at a constant frequency until the regenerator reaches steady-state operation.

III.3 Experimental validation of the model

The model, introduced in section *III.2*, has been experimentally validated with experimental results carried out from the 8Mag prototype, whom is described in chapter *II*. The device employs gadolinium in packed-bed configuration and, therefore the model, which presents the geometry illustrated in section *III.2.1*, requires that MCE of gadolinium has to be modeled and implemented, following the guidelines of section *III.2.4*.

III.3.1 Modeling the magnetocaloric behavior of gadolinium

The magnetic properties of gadolinium have been evaluated by interpolating experimental data of $\Delta T_{ad}(B,T)$ and $C_{sp}(B,T)$ available from existing literature (Griffel et al., 1954; Dan'kov et al., 1998) and reported in section *I.6.3.1* (figures I.25, I.26, I.27).

In accordance with the operating conditions of 8Mag [28], a mathematical formulation has to be obtained in this section that considers the intensity of the magnetic flux density variable from 0 to the maximum value of 1.2 T during magnetization and from 1.2 T to 0 during demagnetization. The properties density and thermal conductivity have been considered constant with respect to temperature and magnetic field variations. Their value, already reported in Table I.1, are 7900 kg/m^3 and 10.9 W/m K, respectively.

As a first step, it have been obtained the tabled functions of ΔT_{ad}, C_{sp} from extrapolation of experimental data, describing the gadolinium behavior during 0÷1.2 T magnetization and 1.2÷0 T demagnetization, with respect to such parameters. Then it has been built the table functions of Q*Δt obtained from the formula (III.2), as:

$$Q(B,T_S) * \Delta t = \rho_s C_{s,p}(B,T_s)\Delta T_{ad}(B,T_s) \qquad \text{(III.8)}$$

The choice of not fixing the value of Δt into the tabled functions has suggested by the need to obtain a greater degree of freedom with respect to AMR cycle frequency. In this way, the period of magnetization-demagnetization Δt is defined directly in the operating conditions of the two-dimensional model and therefore the frequency of the AMR cycle could be varied without changing the $Q(B,T_S) * \Delta t$ mathematical expression.

Then, by the help of a mathematical function finder software, Nutonian Formulize, it have been found the corresponding mathematical expression to the $C_{s,p}$ and $Q^*\Delta t$ tabled functions, for both the magnetization and demagnetization processes:

$$C_{s,p,magn} = 248.5 + 0.0429T_s + 0.000787T_s^2 \cos(0.0461T_s) + \\ -22.2\cos(6.21 + 0.922\cos(0.0471T_s + 0.313\cos(0.0429T_s)) + \\ -0.0985T_s) \tag{III.9}$$

$$C_{s,p,demagn} = 8.401T_s + 0.1051T_s \sin(\sin(\sin 0.07199T_s)) - 837.3 + \\ -0.0157T_s^2 - 0.0001386T_s^2 \sin(0.124T_s + \sin(\sin(\sin 0.07199T_s)) + \\ -\sin(0.07199T_s)) - 5.541\sin(0.07199T_s)\sin(0.124T_s + \\ \sin(\sin(\sin 0.07199T_s)) - \sin 0.07199T_s) \tag{III.10}$$

$$Q_{magn*}\Delta t \\ = 10^6\left\{0.4261 + 2.222\cos(2.145 + 0.03856\,T_s) + \right. \\ \left. + \frac{2.848}{\cos[5.711 - 0.3543\cos(-0.1063\,T_s) - 0.4261\cos(-0.06519\,T_s)] + \cos(-0.06519\,T_s)}\right\} \tag{III.11}$$

$$Q_{demagn} * \Delta t = \\ 10^6\left\{\frac{\cos(0.06204\ T_s)+[4.28+3.083\sin(-0.04417\,T_s)]}{1.172+\sin[6.241-0.04708\,T_s-0.2223\sin(0.01193\,T_s)\sin(-0.1716\,T_s)]}\right\} \tag{III.12}$$

Figures III.2 and III.3 show the interpolated function of $C_{s,p,magn}(B,T_s)$ and $C_{s,p,demagn}(B,T_s)$, corresponding to the mathematical expressions (III.9) and (III.10), respectively. Figures III.4 and III.5 exhibit the $Q_{magn}*\Delta t(B,T_s)$ and the $Q_{demagn}*\Delta t(B,T_s)$, corresponding to the mathematical expressions (III.10) and (III.11), respectively. Circles represent experimental data, whereas the continuous line is the curve fitting. In all the above mentioned figures it is possible to appreciate a peak around the Curie temperature of gadolinium (294K), where the magnetocaloric effect is maximum. Moreover $C_{s,p,magn}(B,T_s)$ has a peak higher than $C_{s,p,demagn}(B,T_s)$, whereas $Q_{magn}*\Delta t(B,T_s)$ and $Q_{demagn}*\Delta t(B,T_s)$ seem to present the same intensity around the highest points. Furthermore, it is clearly visible that the MCE of gadolinium spread over a quite large range of temperature (approximately 200÷400 K).

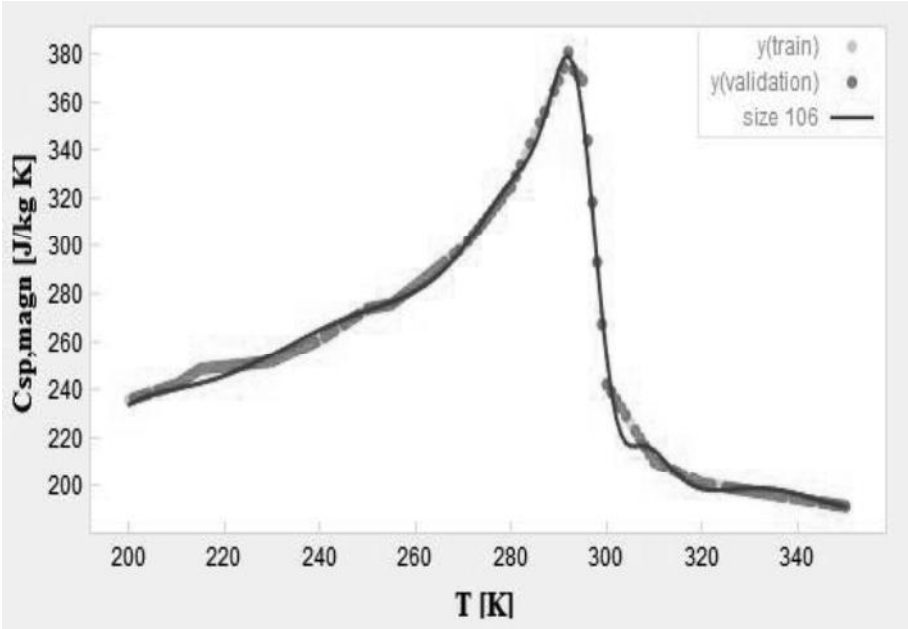

Figure III.2 *The function $C_{sp,magn}(B,T_s)$ for gadolinium during magnetization under a 0÷1.2 T magnetic field induction.*

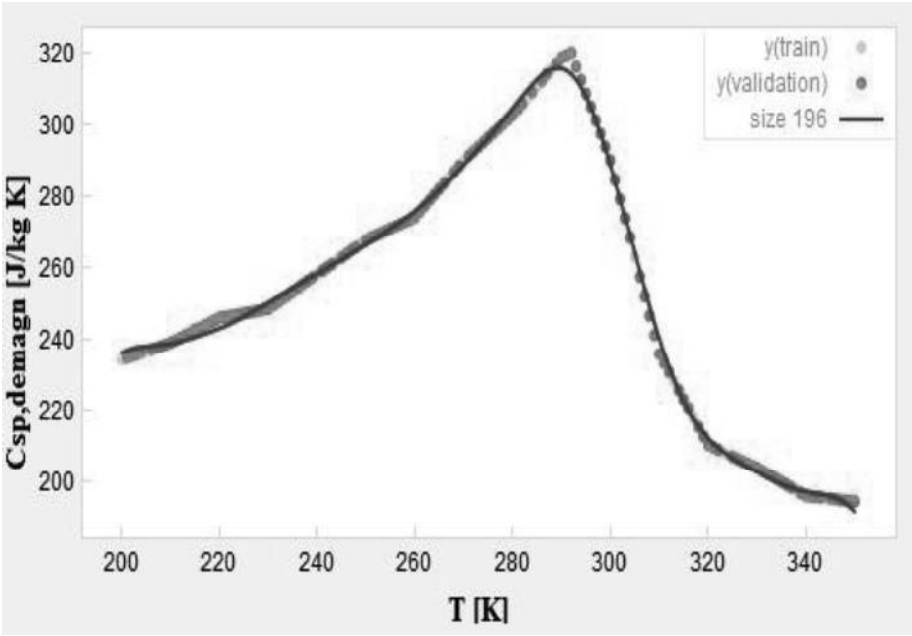

Figure III.3 *The function $C_{sp,demagn}(B,T_s)$ for gadolinium during demagnetization under a 1.2÷0 T magnetic field induction.*

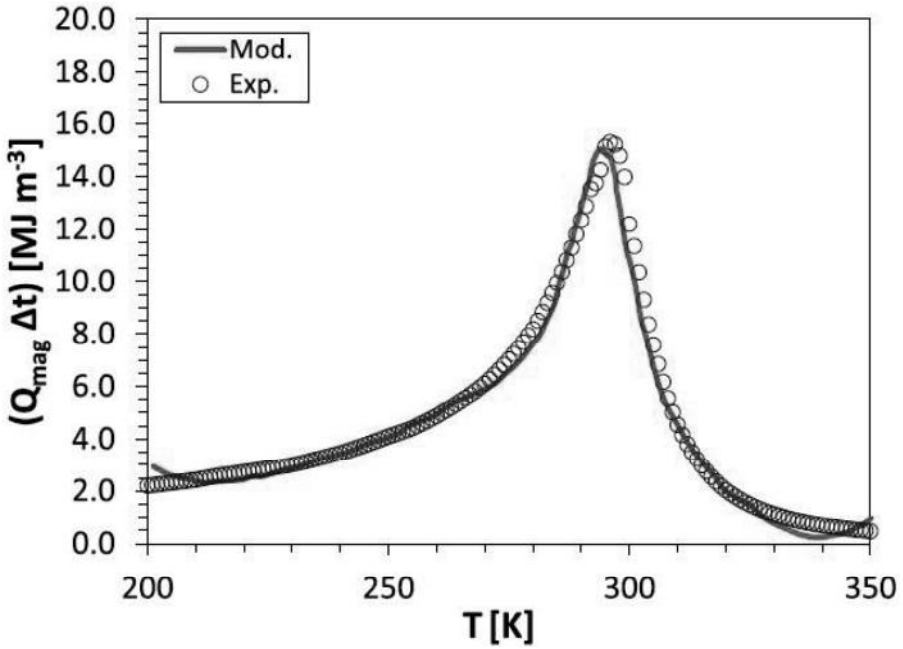

Figure III.4 *The function $Q_{magn}*\Delta t(B,T_s)$ for gadolinium during magnetization under a 0÷1.2 T magnetic field induction.*

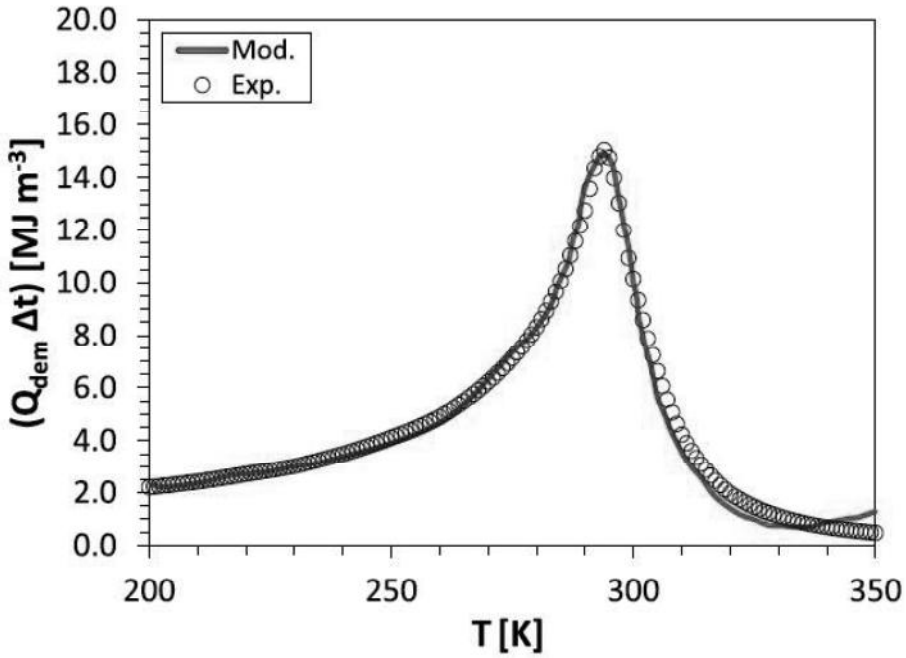

Figure III.5 *The function $Q_{demagn}*\Delta t(B,T_s)$ for gadolinium during demagnetization under a 1.2÷0 T magnetic field induction.*

III.3.2 Operating conditions

To validate the model several AMR cycles were simulated under a zero-load condition (see section *II.2.2*) and applied to the presented model. In all simulations, the fluid is pure water and the solid is pure gadolinium. The simulations are performed to operate under the same conditions of the experimental prototype 8Mag, so that a comparison between the model and the RPMMR can be performed.

Both the model simulations and the experimental tests were performed with a fluid flow rate fixed at 7.0 l/min (normal velocity speed fixed at 0.08335 m/s), whereas the AMR cycle frequency (f_{AMR}) was varied in the range 1.08÷1.79 Hz. The heat rejection temperature, T_H, was also varied over the range of 289÷302 K in order to characterize the performance sensitivity to the heat rejection temperature in the proximity of the refrigerant Curie temperature.

III.3.3 Model results

Velocity, pressure, and temperature fields have been calculated for the aforementioned AMR cycle operating conditions. In figure III.6 is clearly visible a typical velocity field of a water flow in a matrix composed of gadolinium spheres. The operating conditions embraced an AMR cycle frequency of 1.79 Hz and a T_H of 298 K.

According to Kaviany (Kaviany, 1995), the boundary layers are very close to the particle surface for the mass flow under consideration. The flow at the interface changes because both inertial and viscous forces are important in the boundary layer.

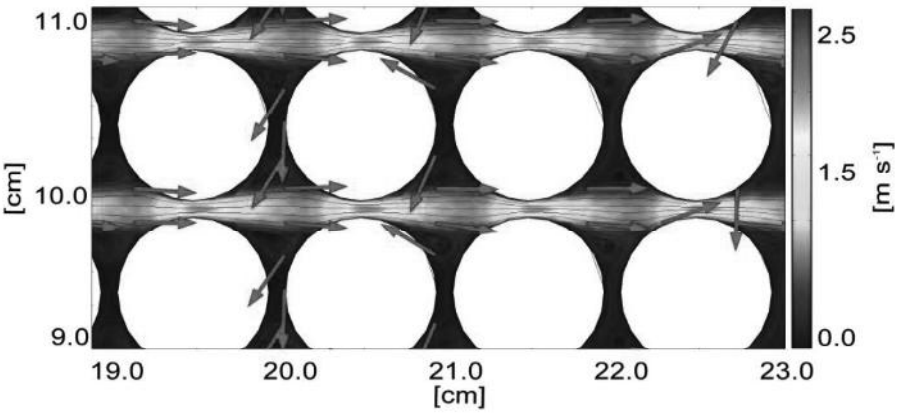

Figure III.6 *Fluid velocity field in the regenerator: velocity field x component [m/s]. Phase of the cycle: fluid flow toward hot heat exchanger (from left to right side). Condition of operation: f_{AMR} =1.79 Hz. T_H = 298 K.*

Figure III.7 shows the temperature distribution in the regenerator, valuated during the magnetization process of the aforementioned test. It is interesting to note the presence of a magnetocaloric effect as heat adduction into the gadolinium spheres during the magnetization phase. Temperature gradients within particles are visible.

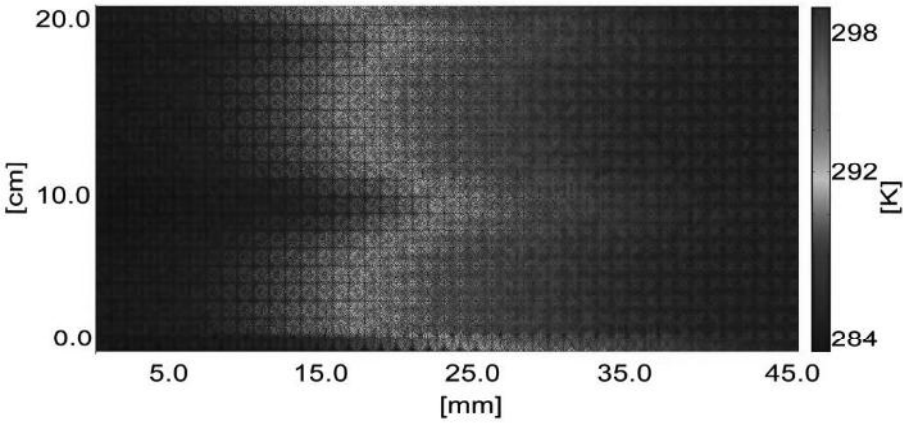

Figure III.7 *Temperature field in the regenerator during magnetization. Condition of operation:* f_{AMR} *= 1.79 Hz.* T_H *= 298 K.*

Figure III.8 exhibits the temperature field in the regenerator during isofield heating, when the steady-state regime has been reached. The fluid is blown from the hot heat exchanger at a temperature of T_H (298 K), expelling heat to the particles of the bed and decreasing the temperature of the fluid. It is possible to determine ΔT_{AMR} by measuring the temperature difference at the left and right ends of the regenerator.

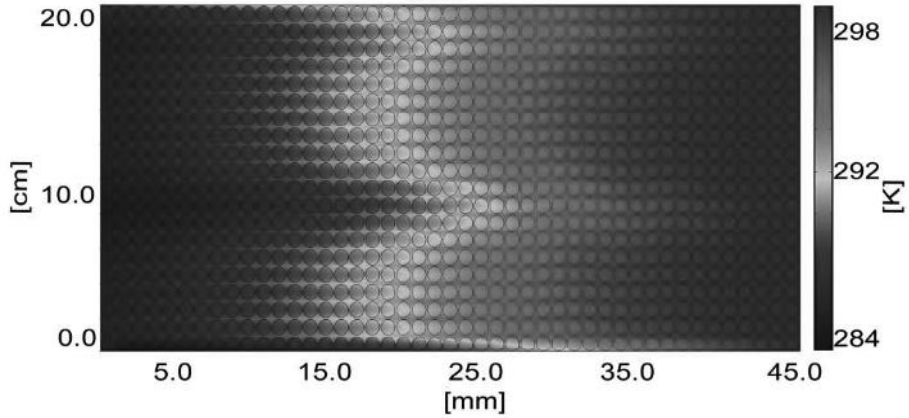

Figure III.8 *Temperature field in the regenerator during isofield heating. Condition of operation:* f_{AMR} *= 1.79 Hz.* T_H *= 298 K.*

Figure III.9 illustrates the pressure field during the isofield heating. The pressure drop evaluated along the regenerator in this step is approximately 0.17 MPa.

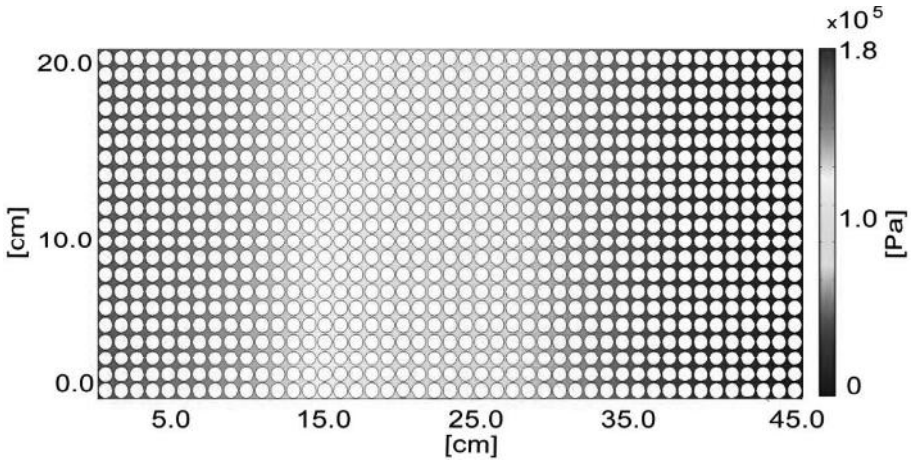

Figure III.9 *Pressure field in the regenerator during the blow phase. Fluid flows toward hot heat exchanger (from left to right side).*

The pressure drop has been evaluated at the ends of the regenerator during an entire AMR cycle, as figure III.10 reports. During the fluid flow phases, a differential pressure is measured across the regenerator at approximately 0.17 MPa; during the magnetization and demagnetization processes there is no pressure drop because fluid does not flow.

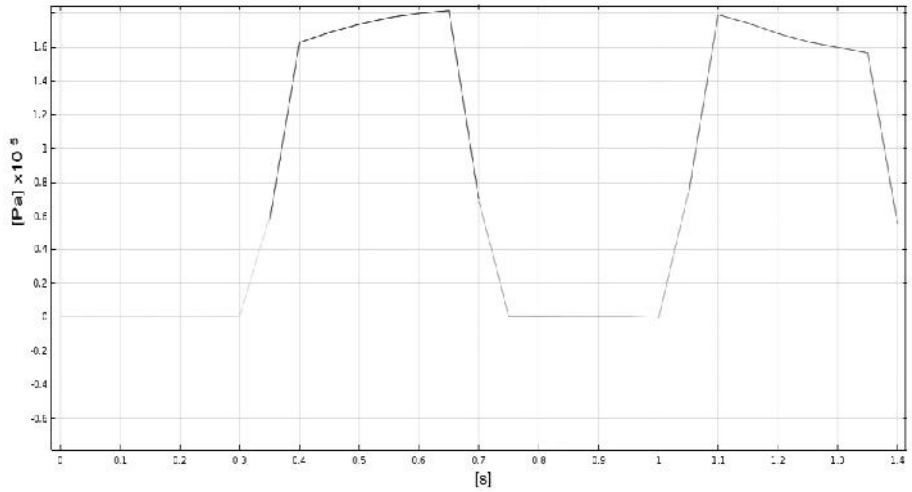

Figure III.10 *Pressure drop estimated across the regenerator during an entire AMR cycle.*

III.3.4 Comparison between experimental and numerical tests

A comparison of the results between the 2D model described in this paper and the RPMMR is presented below. In the experimental tests, the RPMMR device ran at AMR cycle frequencies of 1.08, 1.25, 1.61, and 1.79 Hz. The hot side temperature varied between 289÷302 K.

The experimental and model results are plotted in figures III.11 (a), (b), (c), (d). The general trend shows that the zero-load temperature span increased with the increasing hot-side temperature, reaching a maximum and decreasing afterward. The maximum for both the experimental and model results corresponded to a hot side temperature of approximately 298 K. Corresponding to this hot side temperature, the average temperature of the bed was near the Curie temperature of gadolinium, where the magnetocaloric effect was at its maximum.

Furthermore, the simulation results, in accordance with the experimental results and with the results declared by other researchers (Vuarnoz and Kawanami, 2012; Lozano et al., 2013), show that for each hot side temperature an optimal cycle frequency occurs. As noticed by Lozano et al. (Lozano et al., 2014) this phenomenon happens because at lower frequencies there is a large influence of the longitudinal thermal conduction and the regenerator utilization becomes too high seen that at lower frequencies the temperature span increases with increasing frequency until a certain optimum frequency from which the irreversible losses become significant and the heat transfer is affected, so the regenerator is not capable to maintain a high temperature span.

However, at a higher cycle frequency the fluid was not capable to utilize all the energy available from the magnetocaloric effect, thus lowering the maximum temperature span. The general trend of the model is to overestimate the experimental data. In particular, the overestimating is slight for low hot side temperatures and, overall, for low cycle frequencies. The differences between the experimental and model results increase with increasing cycle frequency. The differences vary between a minimum value of +2% (at 1.25 Hz) and a maximum value of +40% (at 1.79 Hz), with a mean value of approximately +7%. This phenomenon may exist because the model does not account for heat losses due to effects external to the regenerator. These effects may include eddy currents in the surrounding materials and heat leaks from or to the ambient environment due to imperfect insulation. The rotating magnetic field induces eddy currents in the regenerator, which then act as a thermal source in the solid energy balance. The strength of this term increases with frequency. In addition, as well as reported in section *II.2.2* a significant dead volume between the regenerators and the valve ports affects the performance of 8Mag.

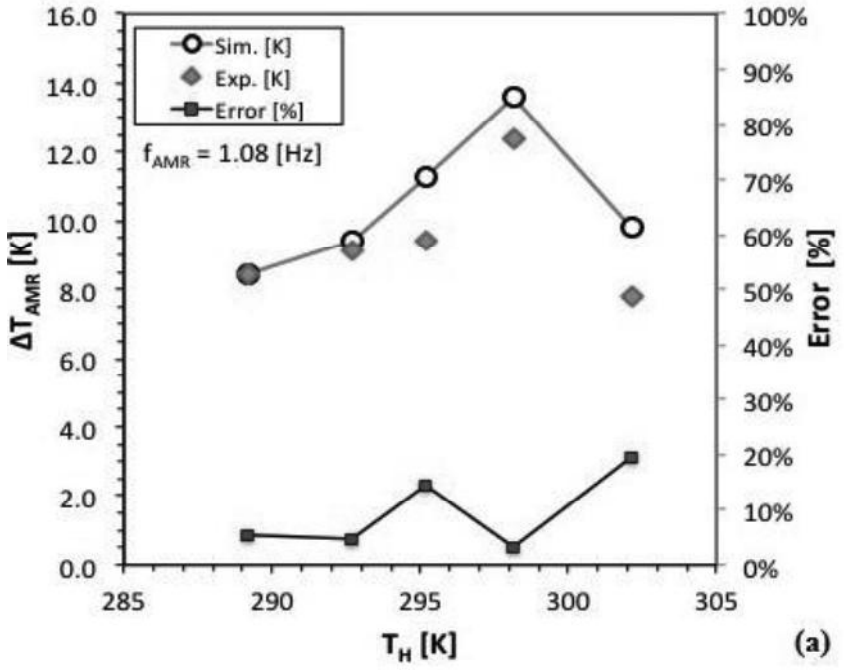
Sim. [K]
Exp. [K]
Error [%]
f_{AMR} = 1.08 [Hz]
ΔT_{AMR} [K]
Error [%]
T_H [K]
(a)

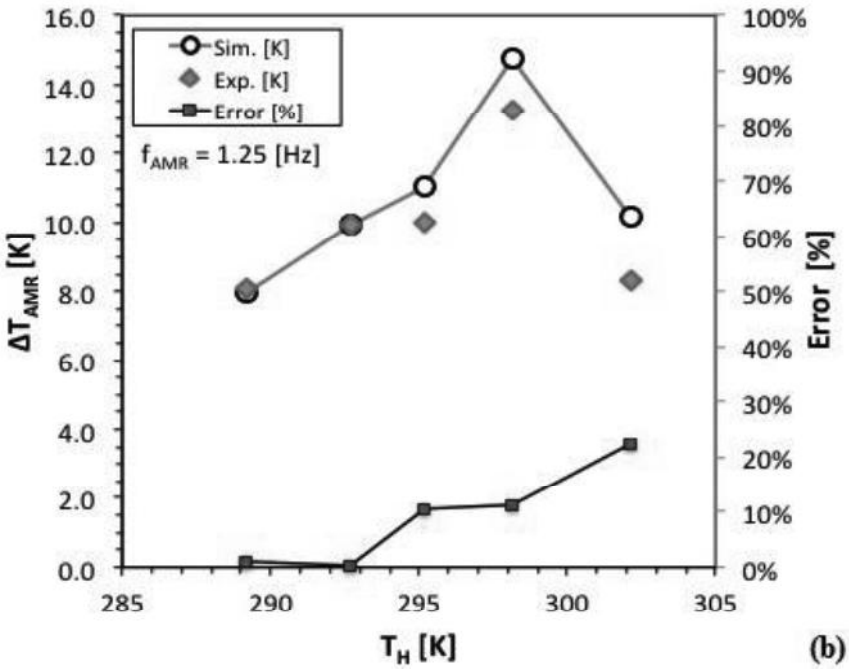
Sim. [K]
Exp. [K]
Error [%]
f_{AMR} = 1.25 [Hz]
ΔT_{AMR} [K]
Error [%]
T_H [K]
(b)

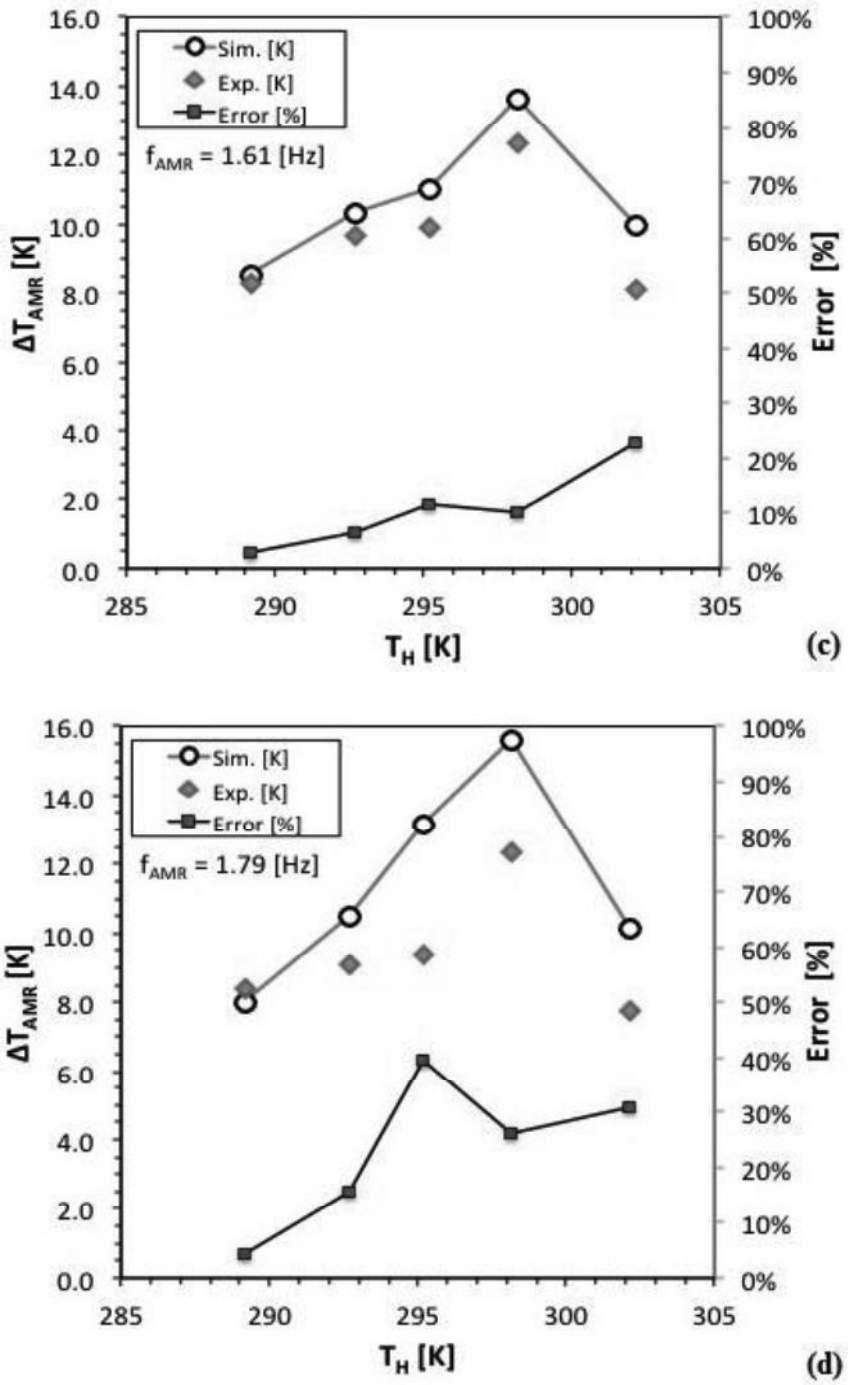

Figure III.11 *Comparison between experimental and simulation results in terms of temperature span ΔT_{AMR} as a function of T_H at f_{AMR} of (a)1.08, (b)1.25, (c)1.61 and (d)1.79 Hz.*

III.3.5 Considerations

The major conclusions arising from this study are as follows:

- the simulation results show good agreement with experimental data;
- the measured pressure drops across the regenerator in the fluid flow phases are almost equal to the model results (approximately 0.17 MPa).
- the zero-load temperature span increases with the increasing hot-side temperature, reaching a peak for both the numerical and experimental data. There exists an optimum temperature that maximizes the magnetocaloric effect. The model predicted this optimum value.
- for each hot side temperature there is an optimal cycle frequency that maximizes the temperature span of the magnetocaloric material.
- in experimental tests conducted at low to moderate frequencies (from 0.72 to 1.25 Hz), the model predicts the experimental data with a maximum deviation of less than +11%;
- in experimental tests at high frequencies, the deviation reaches a maximum value of +40% (with a mean value of +13%). Therefore, the eddy currents inducted in the regenerator cannot be neglected at higher frequencies.

III.4 A rare-earth and transition metal investigation

Once validated the two-dimensional multiphysics model an investigation on new materials has been conducted (Aprea et al., 2015b) in order to identify new magnetocaloric materials candidates to be employed in the 8Mag prototype. Different materials, among the rare-earth and transition metals, previously described in chapter I, have been tested with the model as refrigerants: pure gadolinium, second order phase magnetic transition $Pr_{0.45}Sr_{0.35}MnO_3$ and first order phase magnetic transition alloys $Gd_5(Si_2Ge_2)$, $LaFe_{11.384}Mn_{0.356}Si_{1.26}H_{1.52}$, $LaFe_{11.05}Co_{0.94}Si_{1.10}$ and $MnFeP_{0.45}As_{0.55}$. The main goal of this investigation is to explore the effect of the different magnetocaloric materials on the refrigeration capacity and on the efficiency of the AMR cycle.

III.4.1 Modeling the magnetocaloric behavior of the materials

To employ the materials in the model it is required to obtained the mathematical expression for all the candidates. To do that the magnetic properties of the materials have been evaluated by experimental data of

$\Delta T_{ad}(B,T)$ (see figure I.45) and $C_{s,p}(B,T)$ available from existing literature (Pecharsky and Gschneidner Jr. 1997; Morrison et al., 2012; Bjørk et al., 2010a; de Oliveira and von Ranke, 2005; Guillou et al., 2012) and reported in sections *I.6.3.1-I.6.3.4*. Interpolating the experimental data, the model takes into account the hysteresis effect. As a consequence of hysteresis, the adiabatic transformations are not parallel to the one computed with reversible processes and the irreversibility makes the cycle asymmetrical. As a result of the thermal hysteresis the transition temperature is shifted increasing the magnetic field.

From the construction of tabled functions describing $\Delta T_{ad}(B,T)$, $C_{s,p}(B,T_s)$ and $Q(B,T_s)*\Delta t$ in a range of temperature and magnetic field intensity, and by the help of the already mentioned mathematical finder software, mathematical expressions for $C_{s,p}(B,T_s)$ and $Q*\Delta t$ have been found both for magnetization and demagnetization processes (see section *III.2.4*). In accordance with the operating conditions of 8Mag, the intensity of the magnetic field varies from 0 to the maximum value of 1.5 T during magnetization and from 1.5 T to 0 during demagnetization.

In Table III.1 are listed all the mathematical expressions for the $C_{s,p}(B,T_s)$ terms during magnetizations and demagnetization found for the different magnetocaloric materials tested: $Gd_5(Si_2Ge_2)$, $LaFe_{11.384}Mn_{0.356}Si_{1.26}H_{1.52}$, $LaFe_{11.05}Co_{0.94}Si_{1.01}$, $MnFeP_{0.45}As_{0.55}$, $Pr_{0.65}Sr_{0.35}MnO_3$.

Figures III.12-III.16 show the interpolated functions of $C_{s,p,magn}(B,T_s)$ and $C_{s,p,demagn}(B,T_s)$, corresponding to the mathematical expressions of Table III.1, for all the tested materials. From the above mentioned figures one can observe that $LaFe_{11.384}Mn_{0.356}Si_{1.26}H_{1.52}$ exhibits the highest value of both $C_{s,p,magn}$ and $C_{s,p,demagn}$, around its Curie point. Moreover $Gd_5(Si_2Ge_2)$ is characterized by the narrowest heat capacity curves, with more than doubled values around its FOMT temperature (276 K). On the other side $Pr_{0.65}Sr_{0.35}MnO_3$ shows the broadest $C_{s,p,magn}$ where the influence of MCE on heat capacity spreads in a wide range of temperatures. The properties density and thermal conductivity have been considered constant with respect to temperature and magnetic field variations. Their value are reported in Table I.1.

In Table III.2 are reported the mathematical expressions for the $Q*\Delta t$ terms during magnetization and demagnetization obtained for the different magnetic materials.

Figures III.17-III.21 show the interpolated functions of $Q_{magn}*\Delta t$ and $Q_{demagn}*\Delta t$ corresponding to the mathematical expressions of Table III.2. As one can observe, the highest peak value is registered in $Gd_5(Si_2Ge_2)$ according to its Giant MCE detected by Pecharsky and Gschneidner. LaFeSi compounds show quite better MCE behavior than gadolinium; also in MnFePAs alloys the $Q_{magn}*\Delta t$ peak is higher than gadolinium but manganite composites present very tight MCE curves.

Table III.1 *Mathematical expression of $C_{s,p}$ found for the presented materials during magnetization ($C_{s,p,magn}$) and demagnetization ($C_{s,p,demagn}$).*

Material	Characteristic
$Gd_5(Si_2Ge_2)$	$C_{s,p,magn} = 1.18 \cdot 10^3 + \frac{-1.11 \cdot 10^5}{T_s} + \frac{20.6T_s - 6.1 \cdot 10^3}{T_s\, sin(-0.0174T_s) - 278} - 1.75T_s$ $C_{s,p,demagn} = 370 - 0.457T_s + 18.1 \sin(0.0597T_s) * * \frac{3.05 \cdot 10^4 - 370 \sin(T_s) - 18.1T_s \sin(370.9T_s)}{7.61 \cdot 10^4 + T_s^2 - 551T_s}$
$LaFe_{11.384}Mn_{0.356}Si_{1.26}H_{1.52}$	$C_{s,p,magn} = 578 + \frac{T_s - 307}{cos(-0.0846T_s) - 1.02}$ $C_{s,p,demagn} = 573 + \frac{76200 \sin(0.138T_s)}{479 - 424 \sin(0.18T_s)}$
$LaFe_{11.05}Co_{0.94}Si_{1.01}$	$C_{s,p,magn} = 216.4 + 0.758T_s - \frac{0.75T_s - 265}{1.16 + \sin(-0.0489T_s)} - \sin(0.109T_s)$ $C_{s,p,demagn} = 398 + \frac{93.6T_s}{344.4 + T_s \sin(0.06194T_s + 0.2469 \cos(0.1485T_s))}$
$MnFeP_{0.45}As_{0.55}$	$C_{s,p,magn} = 108 + 1.29T_s + \frac{164}{12.5 + 12.3 \cos(-0.0736T_s)}$ $C_{s,p,demagn} = 1.66T_s + \frac{116}{4.2 + 4.07 \sin(-0.112T_s)}$
$Pr_{0.65}Sr_{0.35}MnO_3$	$C_{s,p,magn} = 1602 - \frac{166400}{T_s} + 0.037T \cos(18.74T_s) - 1.71T_s - 25.77 \cos(-18.8T_s)$ $C_{s,p,demagn} = 553 - 0.136T_s \sin(-0.1808T_s)$

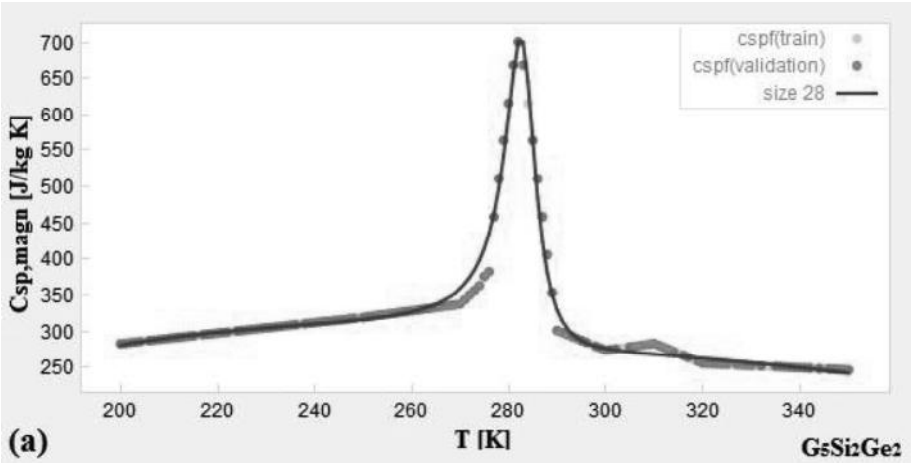

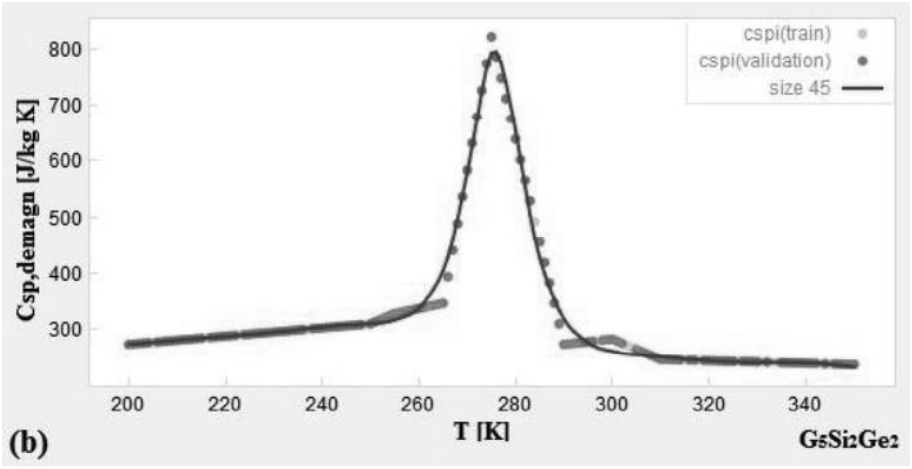

Figure III.12 *(a) $C_{s,p,magn}$ and (b) $C_{s,p,demagn}$ of $Gd_5(Si_2Ge_2)$.*

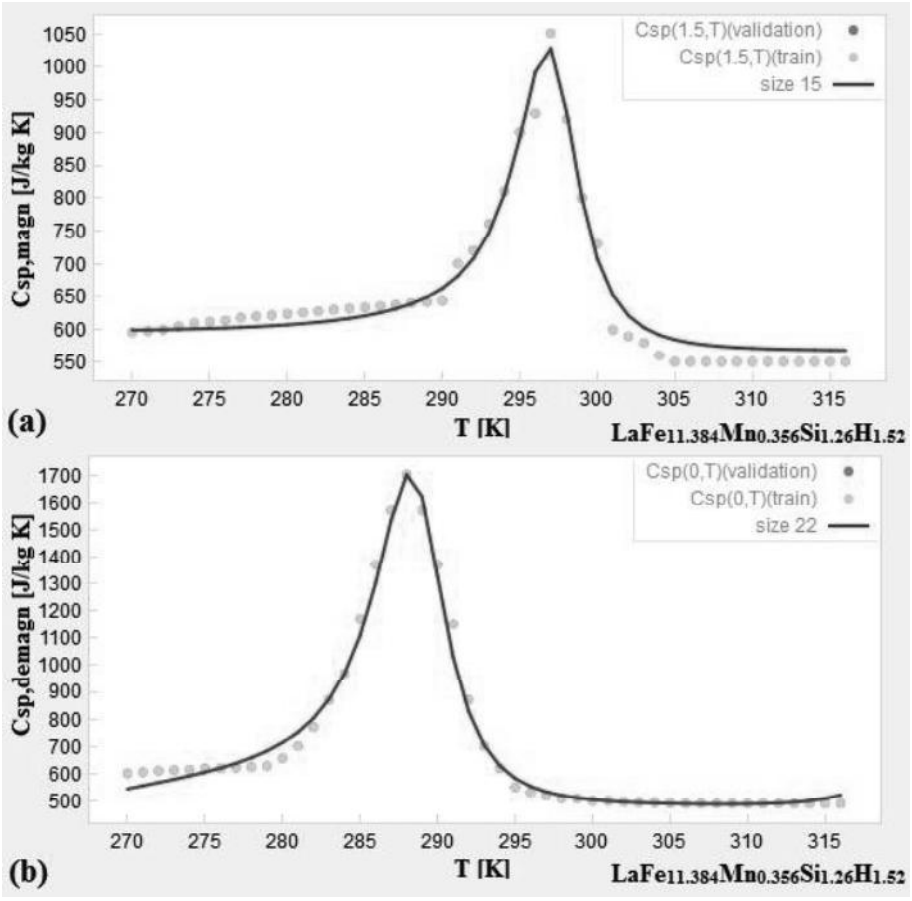

Figure III.13 *(a) $C_{s,p,magn}$ and (b) $C_{s,p,demagn}$ of $LaFe_{11.384}Mn_{0.356}Si_{1.26}H_{1.52}$.*

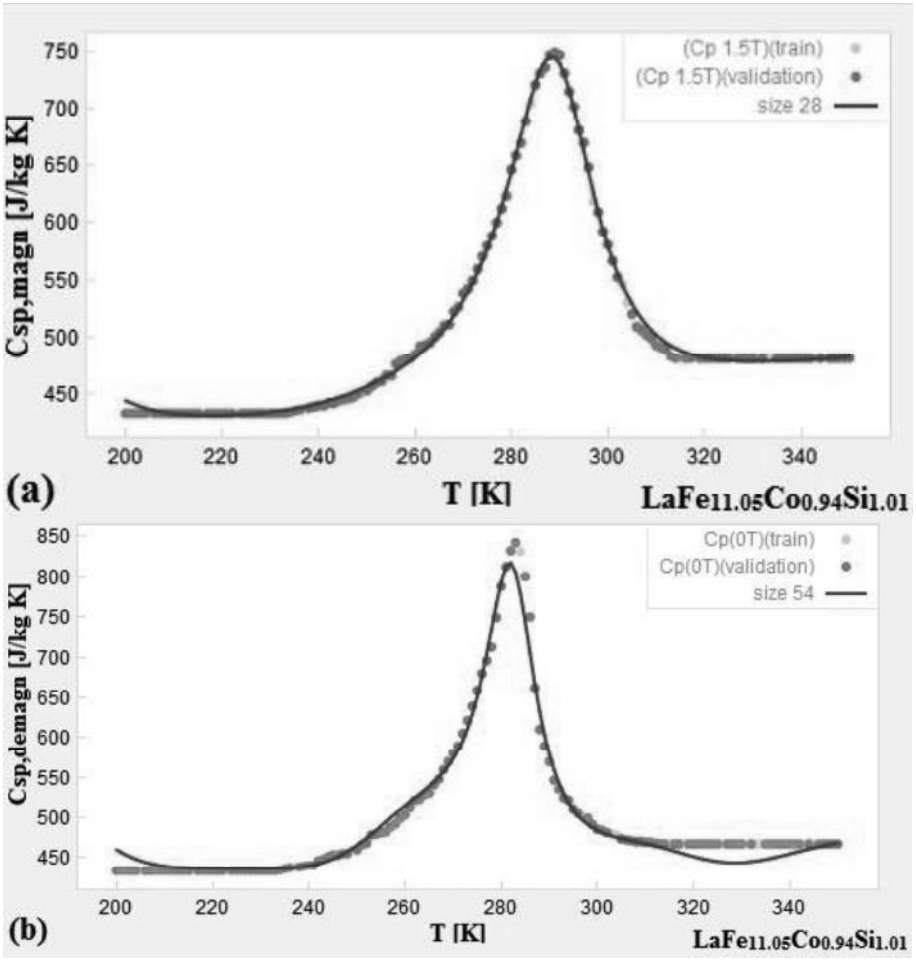

Figure III.14 *(a)* $C_{s,p,magn}$ *and (b)* $C_{s,p,demagn}$ *of* $LaFe_{11.05}Co_{0.94}Si_{1.01}$.

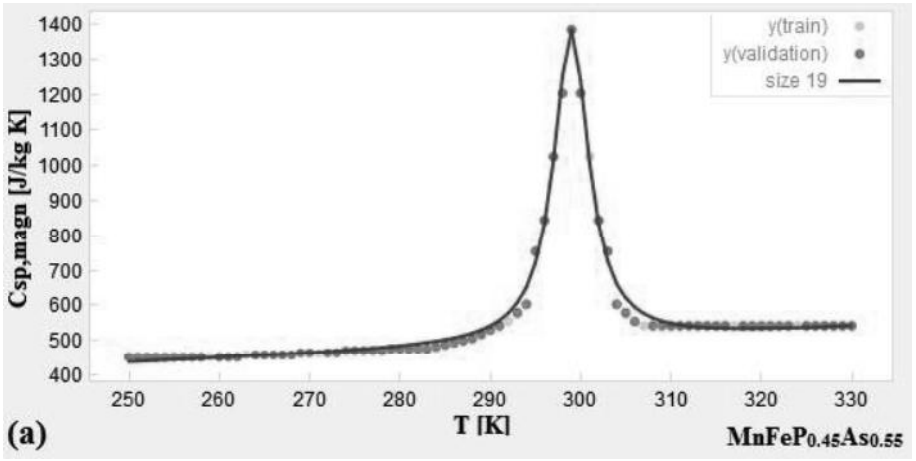

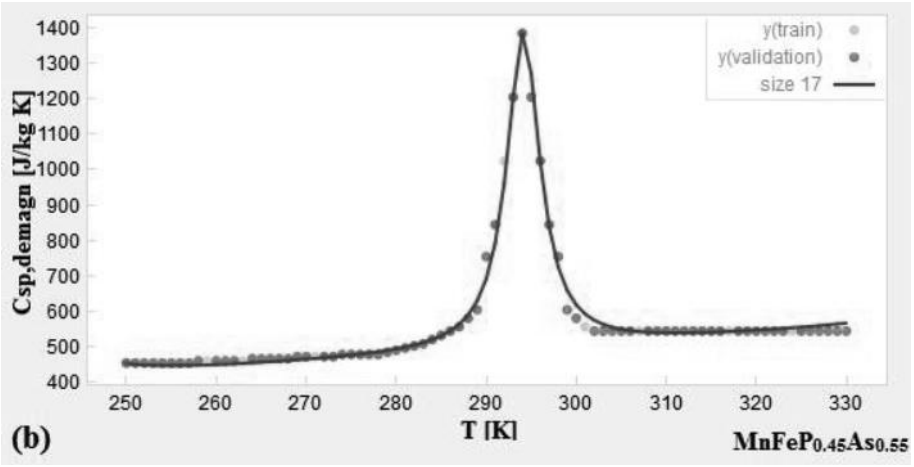

Figure III.15 *(a) $C_{s,p,magn}$ and (b) $C_{s,p,demagn}$ of $MnFeP_{0.45}As_{0.55}$.*

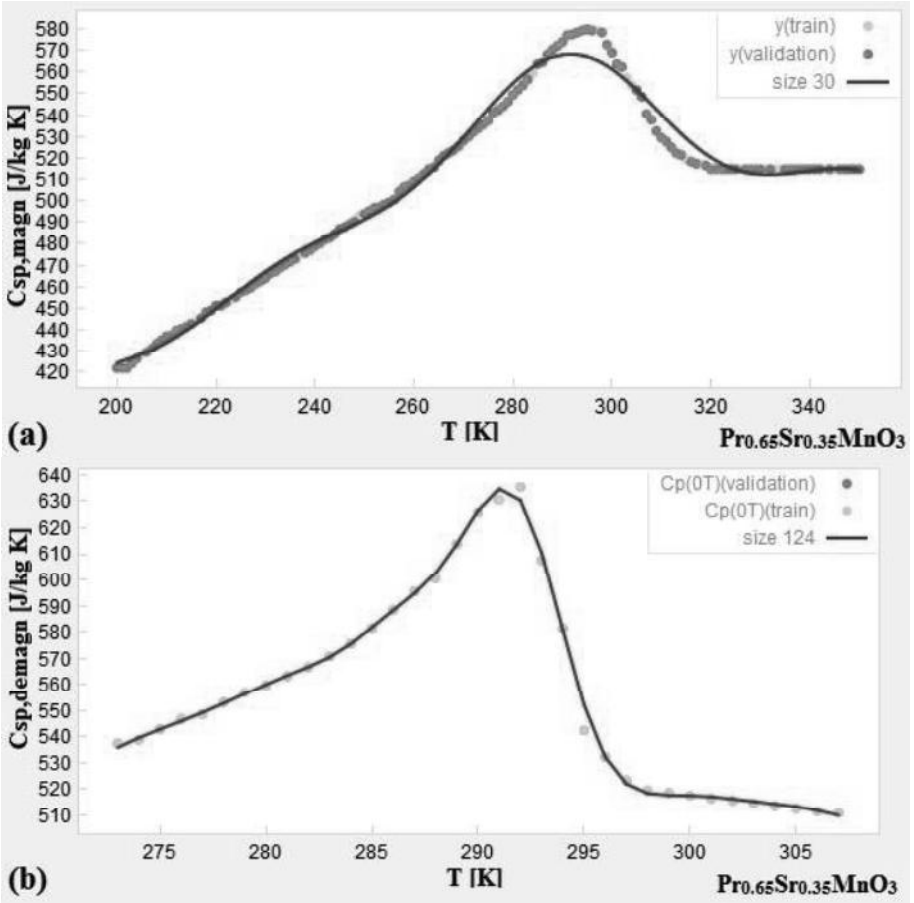

Figure III.16 *(a) $C_{s,p,magn}$ and (b) $C_{s,p,demagn}$ of $Pr_{0.65}Sr_{0.35}MnO_3$.*

Table III.2 *Mathematical expression of Q*Δt found for the presented materials during magnetization (Q_{magn}*Δt) and demagnetization (Q_{demagn}*Δt).*

Material	Characteristic
$Gd_5(Si_2Ge_2)$	$Q_{magn} * \Delta t = 0.877 + \frac{142 - 0.439T_s}{5.15 - 4.82 * \sin(37.9T_s)}$ $Q_{demagn} * \Delta t = \frac{-4.66}{\cos(1.69 - 0.1T_s) - 1.07} + \sin(0.116T_s)$
$LaFe_{11.384}Mn_{0.356}Si_{1.26}H_{1.52}$	$Q_{magn} * \Delta t = 9.85 + 0.0376T_s \cos(-31.2T_s) + \cos(5.52T_s)\cos(-31.2T_s) + \cos(5.52T_s) - 3.35 * \sin(-0.349T_s)$ $Q_{demagn} * \Delta t = 12.4 + \frac{25.2 - \cos(25.7T_s)}{2.05 + \sin(0.121T_s)} - 0.0696T_s$
$LaFe_{11.05}Co_{0.94}Si_{1.01}$	$Q_{magn} * \Delta t = \frac{2.04 + 0.516\sin(-6.17T_s)}{1.14 + \cos(0.28\sin(-12.7T_s) - 0.0549T_s)}$ $Q_{demagn} * \Delta t = \frac{0.6224 + 0.992}{1.086 - sin(0.04885T_s)}$
$MnFeP_{0.45}As_{0.55}$	$Q_{magn} * \Delta t = 1.77 + \frac{133}{T_s + 1.3\sin(1.55T_s) - 293\sin(-0.101T_s)}$ $Q_{demagn} * \Delta t = 2.57 + \frac{0.00256T_s \sin(-0.113T_s)}{\sin(-0.099T_s) - 1.03}$
$Pr_{0.65}Sr_{0.35}MnO_3$	$Q_{magn} * \Delta t = 0.16 + \frac{0.38}{1.06 + \cos(0.032T_s)}$ $Q_{demagn} * \Delta t = \frac{0.0147 - 0.00326T_s}{\sin(3.11 - 0.0475T_s) - 1.16}$

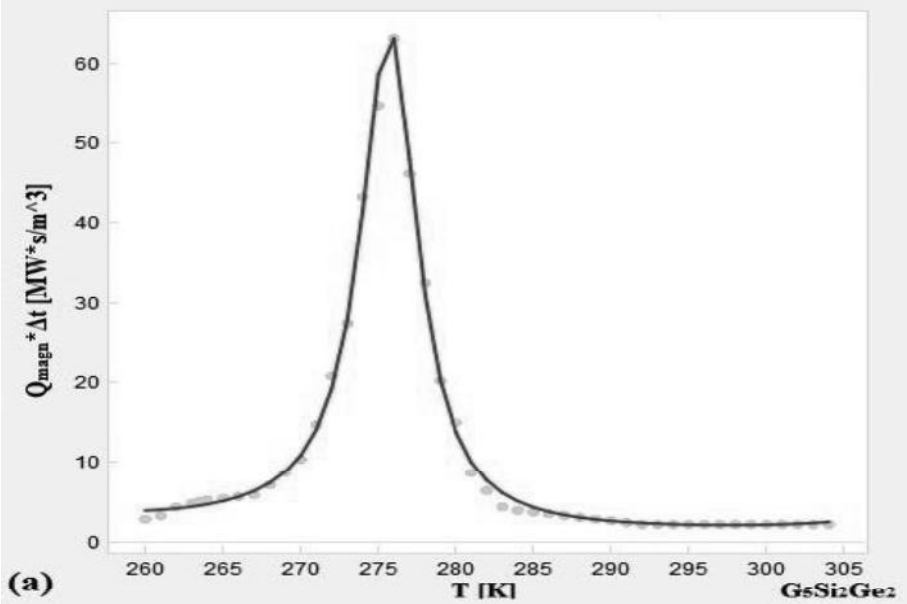

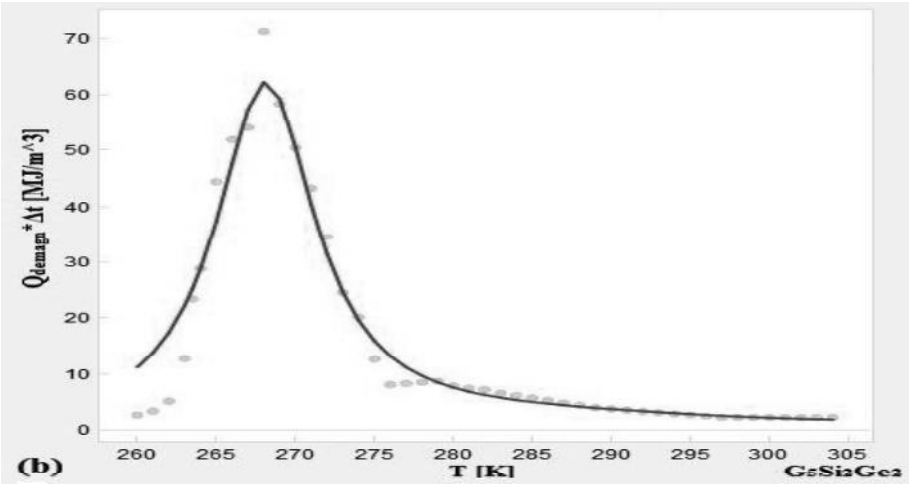

Figure III.17 *(a) $Q_{,magn}$ and (b) $Q_{,demagn}$ of $Gd_5(Si_2Ge_2)$.*

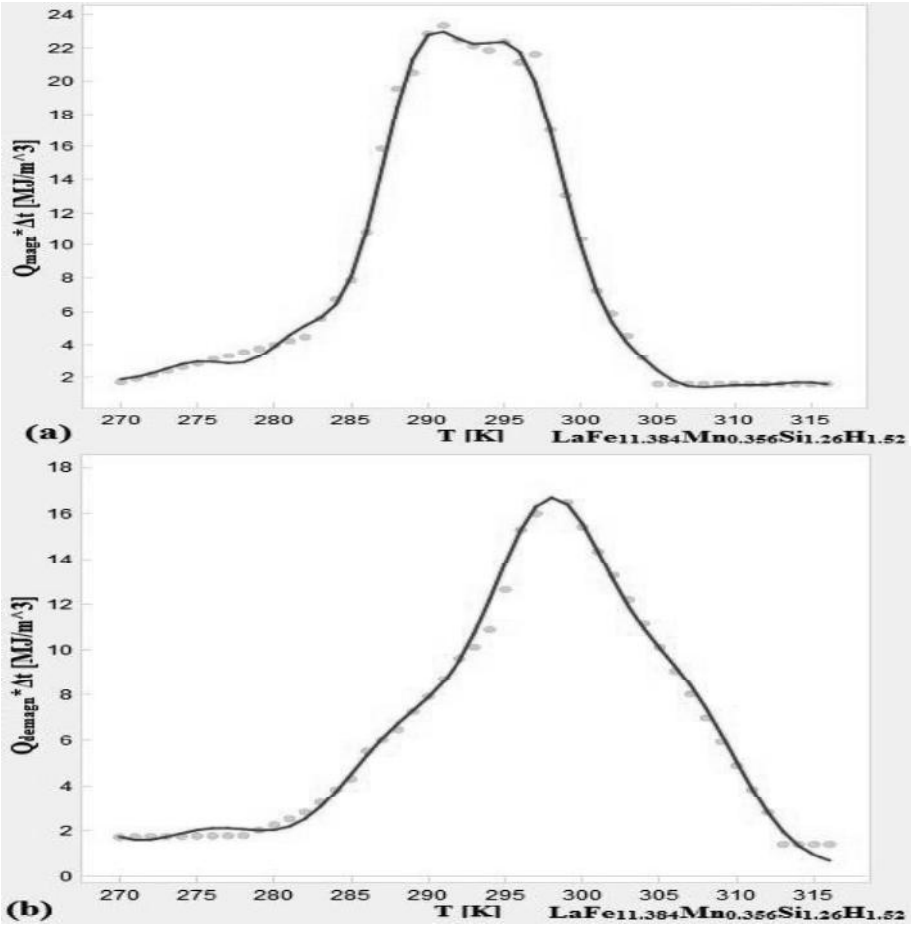

Figure III.18 *(a) $Q_{,magn}$ and (b) $Q_{,demagn}$ of $LaFe_{11.384}Mn_{0.356}Si_{1.26}H_{1.52}$.*

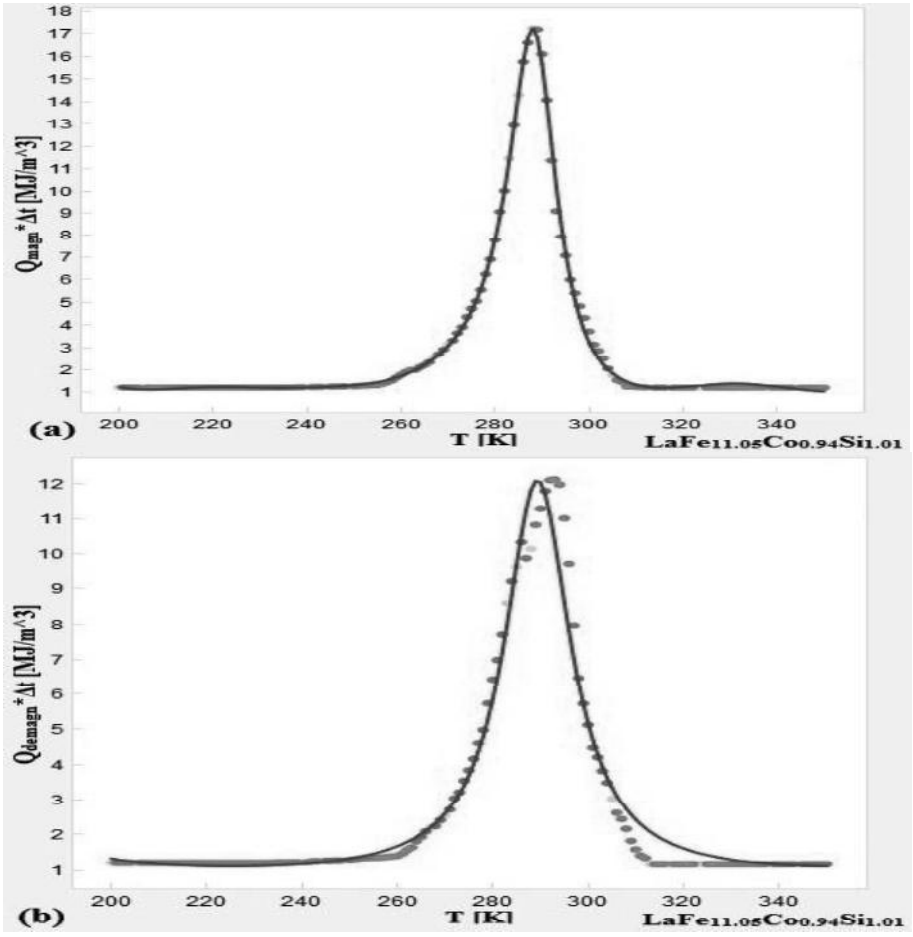

Figure III.19 *(a) $Q_{,magn}$ and (b) $Q_{,demagn}$ of $LaFe_{11.05}Co_{0.94}Si_{1.01}$.*

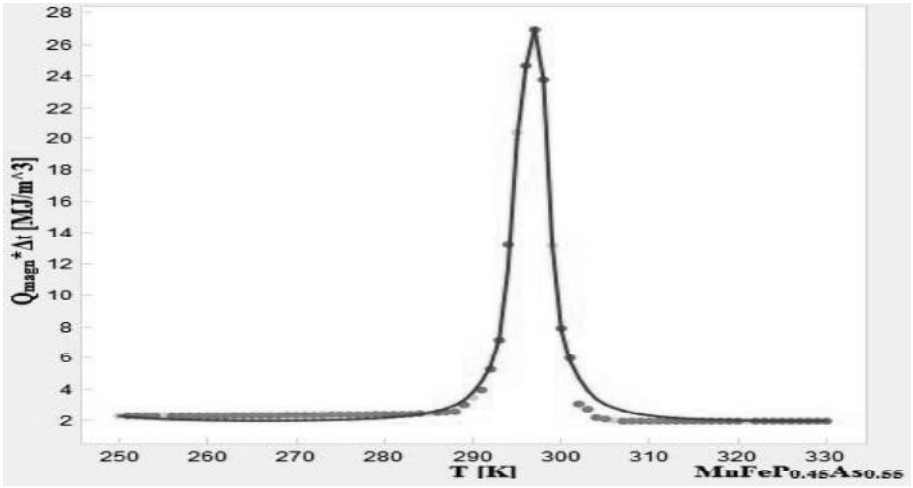

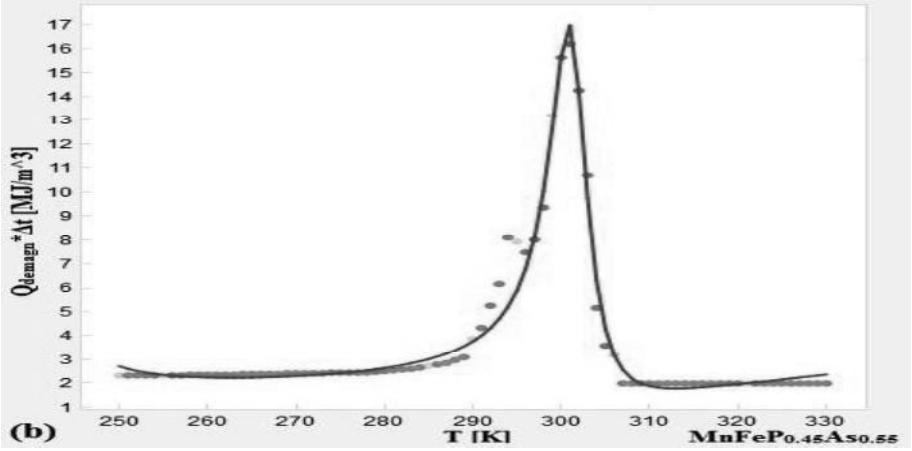

Figure III.20 *(a) $Q_{,magn}$ and (b) $Q_{,demagn}$ of $MnFeP_{0.45}As_{0.55}$.*

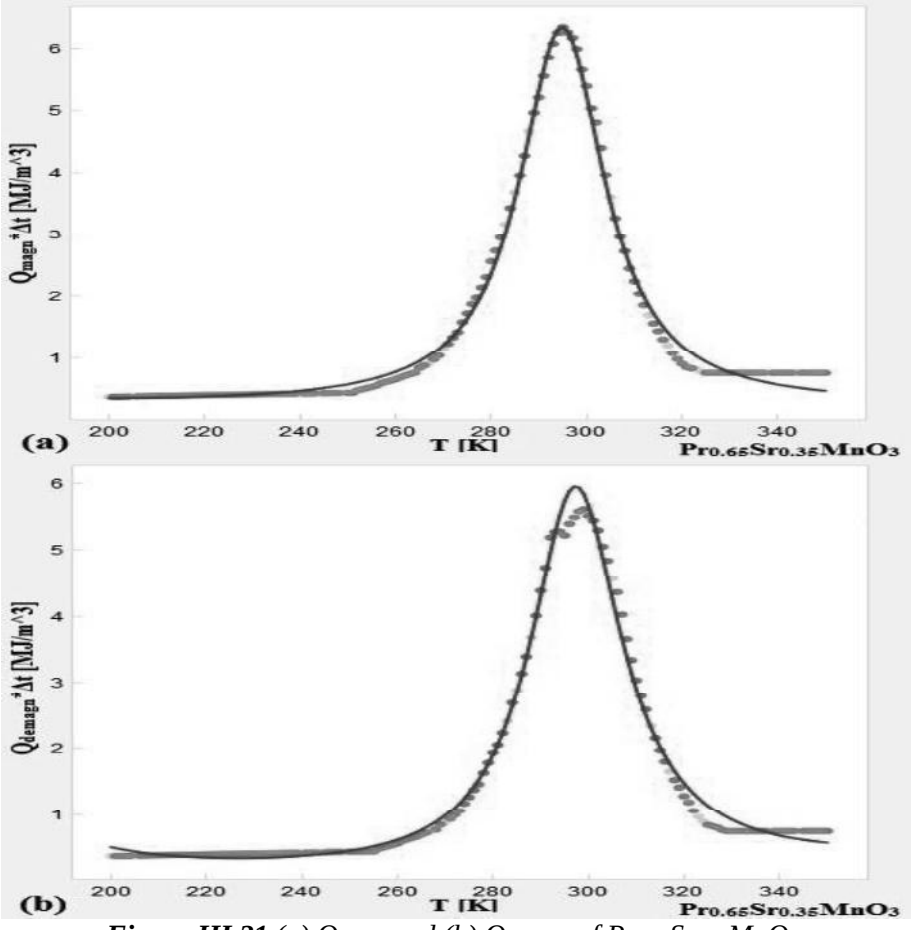

Figure III.21 *(a) $Q_{,magn}$ and (b) $Q_{,demagn}$ of $Pr_{0.65}Sr_{0.35}MnO_3$.*

III.4.2 Operating conditions

Several AMR cycles with the above mentioned magnetocaloric materials employed as refrigerant, have been simulated. As a matter of fact, next to $Gd_5(Si_2Ge_2)$,$LaFe_{11.384}Mn_{0.356}Si_{1.26}H_{1.52}$, $LaFe_{11.05}Co_{0.94}Si_{1.10}$, $MnFeP_{0.45}As_{0.55}$, $Pr_{0.65}Sr_{0.35}MnO_3$, also gadolinium (Gd) has been investigated, under the same operative conditions, in order to make a clearer comparison among the performances of the tested materials. The heat transfer fluid considered is pure water.

The simulations have been performed with fixed flow rate (5 l/min), AMR cycle frequency (1.25 Hz) and cold heat exchanger temperature T_C (288 K). The temperature of the hot heat exchanger T_H was varied in the range 295÷302 K to characterize the performance sensitivity of the heat rejection temperature in proximity of the Curie temperature of the employed refrigerant. The results presented were generated for a magnetic field induction, which varies from 0 to 1.5 T. The results have been collected in terms of ΔT_{span}, refrigeration power and coefficient of performances.

ΔT_{span} has been obtained evaluating the difference between T_H and the cold side temperature of the regenerator averaged in the last process of AMR cycle (fluid flow from hot to cold side of the regenerator), as shown by the following equation:

$$\Delta T_{span} = T_H - \int_{3\Delta t}^{4\Delta t} T_f(0, y, t)\, dt \qquad \text{(III.13)}$$

where Δt is the time duration of every AMR process, x=0 indicates the left boundary of the regenerator (cold side).

The refrigeration power has been calculated according to the following equation:

$$\dot{Q}_{ref} = \frac{1}{\tau}\int_{3\Delta t}^{4\Delta t} \dot{m}_f C_f \left(T_C - T_f(0, y, t)\right) dt \qquad \text{(III.14)}$$

where τ is the period of the AMR cycle, $\dot{m}_f$ is the fluid flow rate.

The Coefficient of Performance has been introduced as follows:

$$COP = \frac{\dot{Q}_{ref}}{\dot{Q}_{rej} - \dot{Q}_{ref} + \dot{W}_p} \qquad \text{(III.15)}$$

where $\dot{W}_p$ is the mechanical power associated to the circulation pump, $\dot{Q}_{rej}$ is the power related to heat supplied in the environment whom has been evaluated as:

$$\dot{Q}_{rej} = \frac{1}{\tau}\int_{\Delta t}^{2\Delta t} \dot{m}_f C_f \left(T_f(L, y, t) - T_H\right) dt \qquad \text{(III.16)}$$

x=L indicates the right boundary of the regenerator (hot side).

$\dot{W}_p$ is the mechanical power associated to the circulation pump:

$$\dot{W}_p = \frac{\dot{m}_f(\Delta p_{CF}+\Delta p_{HF})}{\eta_p \rho_f}(2\Delta t) \quad \text{(III.17)}$$

where η_p is the pump efficiency, Δp_{CF} and Δp_{HF} are the pressure drops across the regenerator, estimated during the cold-to-hot and the hot-to-cold fluid flow processes, respectively.

III.4.3 Results

In Figure III.22 one can see ΔT_{span} detected for the different material under each T_H investigated. The general trend shows that the temperature span increases with the increasing hot-side temperature. The greatest value of temperature span is that proper of $Gd_5(Si_2Ge_2)$ (from +7 to +14% with respect to pure Gd), even if the investigated temperature range does not include its Curie point; rather than $Pr_{0.65}Sr_{0.35}MnO_3$ of whom are registered the smallest ΔT_{span} despite that its Curie temperature is quite centered in the explored temperature range. LaFeSi compounds show value of ΔT_{span} very similar to Gd ones.

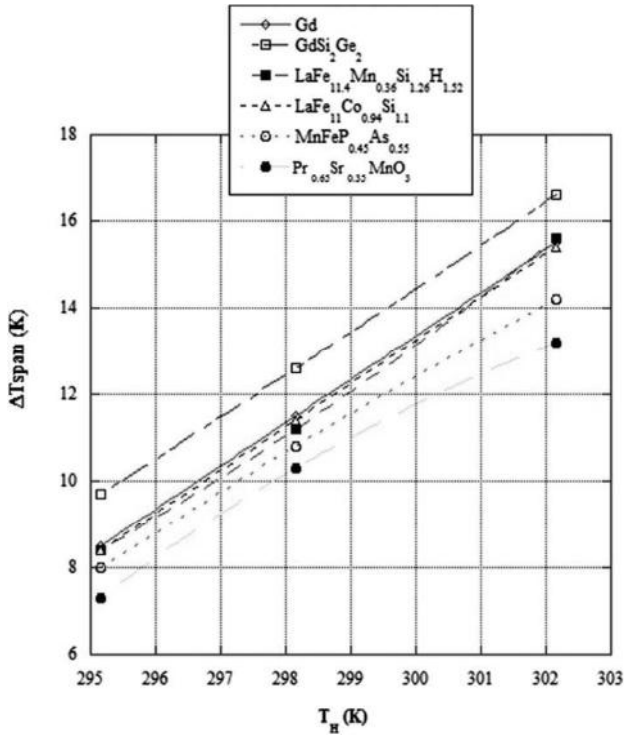

Figure III.22 *ΔT_{span} measured for the tested materials as a function of T_H and compared with gadolinium.*

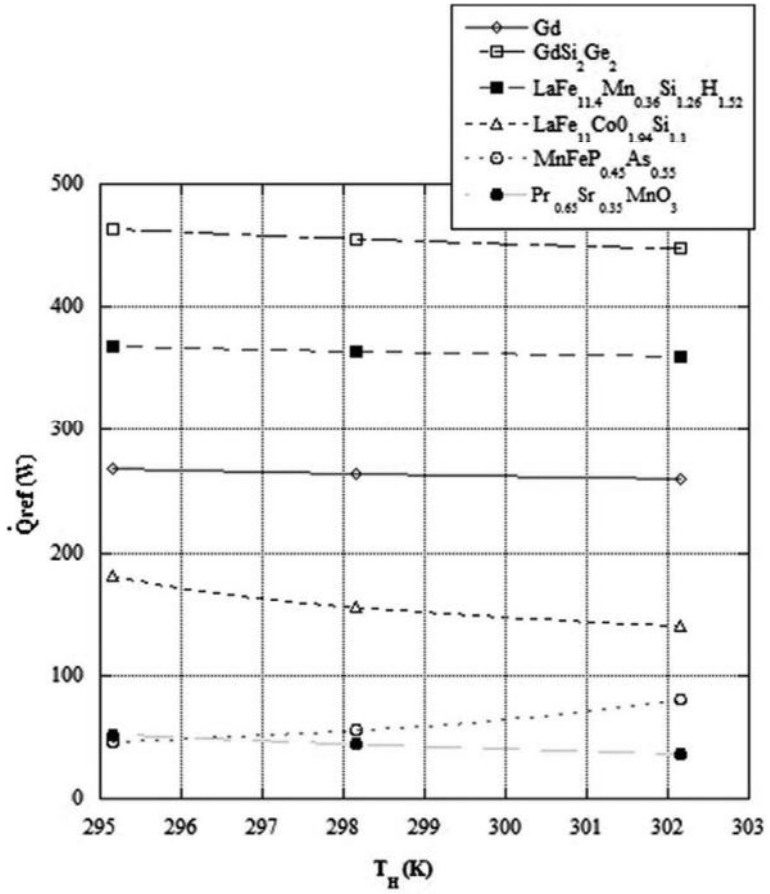

Figure III.23 *$\dot{Q}_{ref}$ evaluated for the tested materials as a function of T_H.*

Figures III.23 and III.24 show respectively refrigeration power ($\dot{Q}_{ref}$) and Coefficient of Performance (COP) as a function of hot heat exchanger temperature for all the materials presented in this work. The refrigeration power decreases with T_H for all the magnetic materials except, $MnFeP_{0.45}As_{0.55}$. Indeed, increasing the latter parameter, it is more difficult for the fluid that enters in the regenerator at a hotter temperature to cool the bed and reach a temperature lower than T_C during the same fixed heat transfer interval. $MnFeP_{0.45}As_{0.55}$ works in a temperature range quite far from its Curie temperature, therefore increasing T_H the MCE increases approaching the maximum. In particular, $Gd_5(Si_2Ge_2)$ shows the greater values of refrigeration power, whereas $Pr_{0.65}Sr_{0.35}MnO_3$ the lower ones. $Gd_5(Si_2Ge_2)$ shows refrigerating powers +73% greater than Gd ones. $LaFe_{11.384}Mn_{0.356}Si_{1.2}6H_{1.52}$ exhibits a significant magnetocaloric effect too, with a refrigeration power on average greater than Gd one between +37 and +46%. $Pr_{0.65}Sr_{0.35}MnO_3$ stronger underperforms Gd with a refrigerating

power around -80%. Figure III.24 clearly shows that COP decreases with the increasing of the amplitude of temperature investigated range. Indeed, increasing the hot heat exchanger temperature the refrigeration power decreases at an almost constant work of the pump. The highest values of COP have been estimated for $Gd_5(Si_2Ge_2)$ since that they are averaging higher than gadolinium of +40%; also in $LaFe_{11.384}Mn_{0.356}Si_{1.26}H_{1.52}$ it has been registered an increment of +30%, still considering gadolinium as benchmark. On the other side, $LaFe_{11.05}Co_{0.94}Si1.10$, $MnFeP_{0.45}As_{0.55}$ and $Pr_{0.65}Sr_{0.35}MnO_3$ always underperform gadolinium.

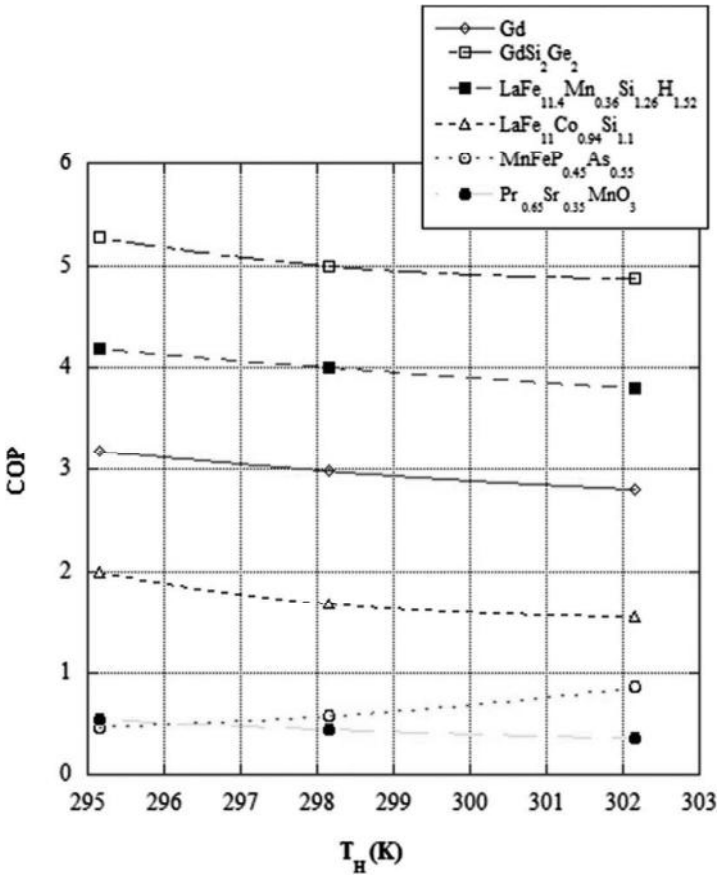

Figure III.24 *COP estimated for the tested materials as a function of T_H.*

III.4.4 Considerations

The tests performed reveal that as expected, from an efficiency point of view, the best candidates to magnetic refrigeration is $Gd_5(Si_2Ge_2)$ which exhibits the highest values of ΔT_{span}, $\dot{Q}_{ref}$ and COP, at all; on the other side $Gd_5(Si_2Ge_2)$ is a very expensive material, disadvantage which makes it

impractical for every economic plan of magnetic refrigerator commercialization. From a global point of view (performances and cost), the most promising materials are LaFeSiH compounds which are cheaper than rare earth compounds and they give a performance sufficiently higher than gadolinium. Instead manganites, in particular MnFePAs composites, could work quite well as long as they are tested in a very narrow range, centered around their Curie point.

III.5 A TEWI investigation of different magnetocaloric materials

After evaluated the energetic performances of new magnetocaloric material when employed as refrigerant in an AMR regenerator, in the present section attention is directed towards the evaluation of the environmental impact in terms of a greenhouse effect. The energetic performances of a commercial R134a refrigeration plant have been compared to the AMR refrigerator working with the materials tested in section *III.4* (pure gadolinium, $Gd_5(Si_2Ge_2)$, $LaFe_{11.384}Mn_{0.356}Si_{1.26}H_{1.52}$, $LaFe_{11.05}Co_{0.94}Si_{1.10}$, $MnFeP_{0.45}As_{0.55}$, $Pr_{0.65}Sr_{0.35}MnO_3$). As a matter of fact, a comparison in terms of TEWI (Total Equivalent Warming Impact) index has been made (Aprea et al., 2015c).

III.5.1 The TEWI concept

Worldwide, about 15% of the overall energy consumption originates from refrigeration. Human activities have increased the concentration of greenhouse gases in the atmosphere, thus resulting in a substantial warming of both earth surface and atmosphere that adversely affect the natural ecosystem. The impact of greenhouse gases on global warming is quantified by their GWP (Global Warming Potential). The GWP is defined as the mass of CO_2 that would result in the same net impact on global warming as the release of a single unit (kg) of the component.

A vapor compression plant produces both a direct and an indirect contribution to global warming. The former depends on the GWP of refrigerant fluids and on the fraction of refrigerant charge which is either directly released in the atmosphere during operation and maintenance, or is not recovered when the system is scrapped. The indirect contribution is related to energy-consumption of the plant. As a matter of fact, a vapor compression refrigerator requires electrical energy produced by a power plant that typically burns a fossil fuel, thus releasing CO_2 into the atmosphere. The amount of CO_2 emitted is a strong function of the COP of the vapor compression plant.

Magnetic refrigeration it is based on solid-state refrigerants whom have essentially zero vapor pressure, and therefore they are ecological with no

direct Ozone Depletion Potential (ODP) and zero direct Global Warming Potential (GWP).

The concept of total equivalent warming impact (TEWI) was developed to combine the effect of direct refrigerant emission with those due to energy consumption and the related combustion of fossil fuels for the electric energy production. TEWI provides a measure of the environmental impact of greenhouse gases originating from operation, service and end-of-life disposal of the equipment. TEWI is the sum of the direct contribution of the greenhouse gases used to make or operate the systems and the indirect contribution of carbon dioxide emissions resulting from the energy required to run the systems over their normal lifetimes.

The TEWI is calculated as:

$$TEWI = CO_{2,dir} + CO_{2,indir} \qquad [\text{kg } CO_2] \qquad \text{(III.18)}$$

$$CO_{2,dir} = RC\left[P_L + \left(\frac{1-P_R}{V}\right)\right] V \cdot GWP \qquad [\text{kg } CO_2] \qquad \text{(III.19)}$$

$$CO_{2,indir} = \alpha \cdot \frac{\dot{Q}_{ref}}{COP} \cdot H \cdot V \qquad [\text{kg } CO_2] \qquad \text{(III.20)}$$

The direct global warming effect of refrigerant fluids, stemming from the absorption they produce of long-wave radiations, depends on their GWP and on the fraction of refrigerant charge released in the atmosphere. The last is mainly due to leakage during the operational plant life time (P_L) and to the residual amounts which, according to the current state of technology, are not recyclable and thus are released to the atmosphere when taking the plant out of operation (1-P_R). In the simulation P_L is assumed as 5%, whereas P_R has not been considered. As already stated, the indirect contribution to TEWI consists in the so-called energy-related contribution.

Indeed, an electrical refrigerator requires electrical energy from a CO_2 releasing power plant that typically burns a fossil fuel. The amount of CO_2 emitted is a function of the refrigerator COP, of the power plant efficiency and of the fuel used in the conversion plant that affect the emissions per unit energy converted.

The typical power-plant technology adopted varies from one country to another. The literature provides some indicative, average levels of CO_2 release per KWh of electrical energy for various countries.

For Italy, the value is 0.6 kg CO_2/kWhe. The annual power consumption in the TEWI simulation is 290 kWh per year that corresponds to a commercial medium size wine cooler. R134a is an HFC with zero ODP and a GWP of 1300.

III.5.2 Operating conditions

Several AMR cycles with different magnetocaloric materials employed as refrigerant, have been simulated. The MCE materials kept under investigation have been the ones tested in section *III.4* (Gd, $Gd_5(Si_2Ge_2)$ and alloys of $LaFe_{11.384}Mn_{0.356}Si_{1.26}H_{1.52}$, $LaFe_{11.05}Co_{0.94}Si_{1.10}$, $MnFeP_{0.45}As_{0.55}$, $Pr_{0.65}Sr_{0.35}MnO_3$). In all of the cases, the secondary fluid is pure water. The simulations were performed with fixed: fluid flow rate (5 l/min), frequency of the AMR cycle (1.25 Hz) and cold heat exchanger temperature T_C (288 K). The hot heat exchanger temperature TH was varied in the range 295÷302 K to characterize the performance sensitivity of the heat rejection temperature in proximity of the refrigerant Curie temperature. The results presented were generated for a magnetic induction, which varies from 0 to 1.5 T.

III.5.3 Results

TEWI is the sum of the direct and indirect contribution to global warming. The direct contribution of the AMR cycle is zero because the refrigerant is solid and therefore has essentially zero vapor pressure and zero GWP. The direct contribution of the vapor compression plant accounts about 10 % of the whole value. The parameter that affects the indirect contribution of the TEWI is the COP of the plant.

In Figure III.25 is shown the Coefficient of Performance (COP) as a function of hot heat exchanger temperature for all the materials presented in this work and for the vapor compression plant. The Figure clearly shows that $Gd_5(Si_2Ge_2)$ and $LaFe_{11.384}Mn_{0.356}Si_{1.26}H_{1.52}$ have the highest values of COP and always over performs a vapor compression plant. The results of the simulation clearly show that $Gd_5(Si_2Ge_2)$ is the best magnetic material with a COP that is always greater than that of a traditional vapor compression plant in the same operating conditions (from a minimum of + 26 to a maximum of +44 %). Gd show energetic performances similar to a vapor compression plant. Instead $LaFe_{11.05}Co_{0.94}Si_{1.10}$, $MnFeP_{0.45}As_{0.55}$ and $Pr_{0.65}Sr_{0.35}MnO_3$ always under perfom vapor compression. Therefore, the COP of the AMR cycle working with these materials needs some improvements.

In order to make a comparison ΔTEWI has been defined according to the following equation:

$$\Delta TEWI = \frac{(TEWI_{AMR} - TEWI_{VC})}{TEWI_{VC}} \qquad \text{(III.21)}$$

Figures III.26(a) and (b) report ΔTEWI evaluated for the tested magnetocaloric materials and compared with the commercial R134a vapor compression plant. Figure III.26(a) show ΔTEWI estimated for Gd,

$Gd_5(Si_2Ge_2)$ and $LaFe_{11.384}Mn_{0.356}Si_{1.26}H_{1.52}$ as a function of T_H. The figure clearly shows that the AMR cycle working with these magnetic materials shows a lower greenhouse effect with respect to a vapor compression plant. In particular, with $Gd_5(Si_2Ge_2)$ ΔTEWI varies from a minimum of -44 % to a maximum of -38 %.

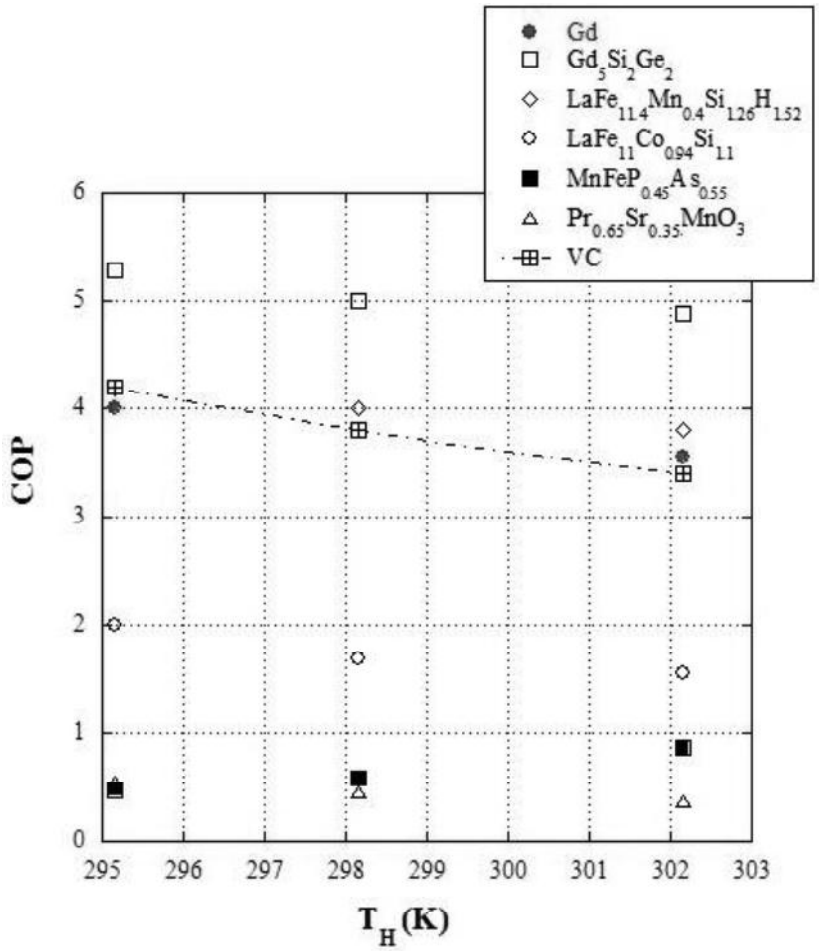

Figure III.25 *COP as a function of the hot heat exchanger temperature.*

In figure III.26(b) is reported ΔTEWI of $LaFe_{11.05}Co_{0.94}Si_{1.10}$, $MnFeP_{0.45}As_{0.55}$ and $Pr_{0.65}Sr_{0.35}MnO_3$ as a function of T_H. The figure clearly shows that the AMR cycle working with these magnetic materials strongly under performs a vapor compression plant. Therefore, these magnetic materials cannot be considered for a commercial use because showing a contribution in term of greenhouse effect greater than the one of a vapor compression plant.

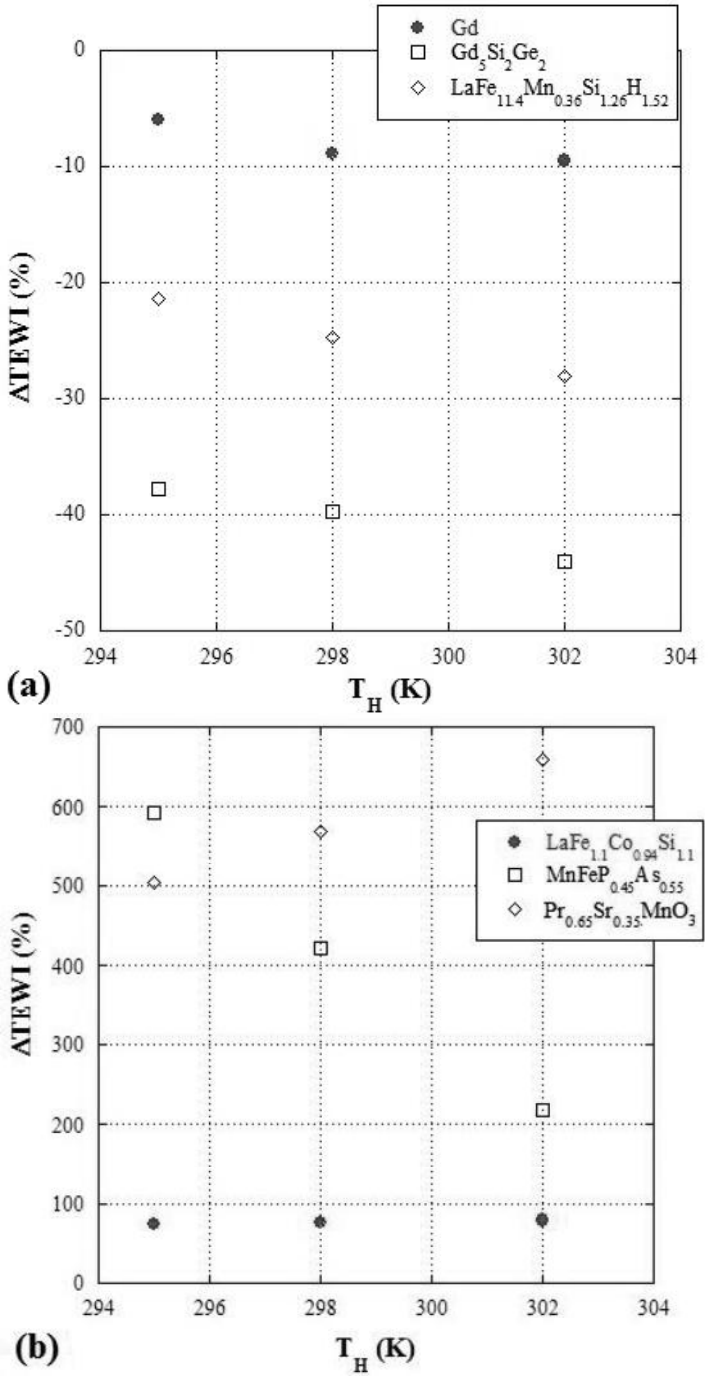

Figure III.26 *ΔTEWI of (a) Gd, $Gd_5(Si_2Ge_2)$, $LaFe_{11.384}Mn_{0.356}Si_{1.26}H_{1.52}$, (b) $LaFe_{11.05}Co_{0.94}Si_{1.10}$, $MnFeP_{0.45}As_{0.55}$ and $Pr_{0.65}Sr_{0.35}MnO_3$ as a function of the hot heat exchanger temperature.*

III.5.4 Considerations

Employing the tested material as solid-state refrigerant in an AMR refrigeration and evaluating the greenhouse effect by means of TEWI index, reveal that:

- $Gd_5(Si_2Ge_2)$ and $LaFe_{11.384}Mn_{0.356}Si_{1.26}H_{1.52}$ have TEWI indexes always lower the ones of the vapor compression plant. In particular, $Gd_5(Si_2Ge_2)$ is the best magnetic material because an AMR cycle working with the latter material shows a -40% greenhouse effect lower than the one of a traditional vapor compression plant.
- Gd, that is the benchmark material for magnetic refrigeration, shows a greenhouse effect similar to that of a vapor compression plant.
- $LaFe_{11.05}Co_{0.94}Si_{1.10}$, $MnFeP_{0.45}As_{0.55}$ and $Pr_{0.65}Sr_{0.35}MnO_3$ cannot be considered because show a contribution in term of greenhouse effect greater than the one of a vapor compression plant.

These results indicate that magnetic refrigeration is a promising refrigeration technology that will be used in chiller applications. An AMR cycle can be an eco-friendly technology if used with magnetic materials that show a significant magnetocaloric effect. As expected, from an efficiency point of view, the best candidates to magnetic refrigeration is $Gd_5(Si_2Ge_2)$ which exhibits the lower values of TEWI index, but on the other side is a very expensive material, disadvantage which makes it impractical for every economic plan of magnetic refrigerator commercialization. From a global point of view (performances and cost), the most promising material are LaFeMnSiH compounds which are really cheaper than rare earth compounds and they give a contribution to global warming sufficiently lower than that of a vapor compression plant.

III.6 An investigation about magnetocaloric regenerator design

Next to the investigations on new magnetocaloric materials and their environmental impact, also the regenerator design is a key aspect to be improved.

In this section is introduced an investigation conducted (Aprea et al., 2016b) about the magnetocaloric refrigerator design through the two-dimensional multiphysics numerical model working on two different magnetocaloric regenerators: (1) a packed bed and (2) a parallel plate magnetic regenerators made of gadolinium, operating at room temperature under a 1.5T magnetic field induction. Both models employ water as secondary fluid.

III.6.1 The regenerator's geometries

The performances of a magnetic refrigerator AMR based, are mostly influenced by:

- the MCE properties of the magnetic material employed;
- the regenerator geometry and related operating conditions;
- the irreversible heat losses due to non-idealities of the refrigerators.

The criteria to identify the best magnetic material for magnetic refrigeration have been largely treated in previous section. The benchmark material adopted in the investigation is gadolinium in order to easily extend the comparison to the experimental prototype (8Mag) improvements.

The irreversible heat losses of AMR regenerators have also great influence on the performances of the AMR cycle (Aprea et al. 2013). Main irreversible heat losses are:

- heat transfer between regenerator and heat transfer fluid;
- pressure drop by flow resistance;
- thermal conduction along the magnetic material;
- heat leakage;
- losses due to magnetic hysteresis and eddy currents;
- viscous dissipation in the secondary fluid;
- "dead volume" loss which is due to the heat transfer fluid trapped in the connecting lines between the bed and the heat exchangers.

In the cooling system, the regenerator geometry assumes paramount importance (Dikeos et al., 2006; Aprea et al., 2011a; 2012b) for gaining efficient heat transferring between magnetic material and fluid flow, thus minimizing the major loss in the cooling system. Two different regenerators are both widely used: a parallel plate regenerator, which yields lower pressure drops; a packed bed regenerator which can produce a larger temperature span, due to the larger extension of the heat transfer surface.

Next to the investigations on new magnetocaloric materials and their environmental impact, also the regenerator design is a key aspect to be improved.

This investigation compares the results of the numerical two-dimensional (2D) multiphysics model working with: (a) a packed bed and (b) a parallel plate magnetic regenerators made of gadolinium, operating at room temperature under 1.5 T as magnetic field induction. Both models employ water as secondary fluid.

The regenerator has a rectangular shape (20x45mm) which acts as a wrapper.

The area of the packed bed regenerator is filled with a regular matrix of 3600 circles that constitute the magnetocaloric material, i.e. gadolinium; every circle has a diameter of 0.45mm and the amount of the area occupied

by all the circles is about 60% of the total rectangular area. A group of channels is formed by stacking particles in the regenerator area: the fluid flows through these interstitial channels. In Figure III.27 is shown a scheme representing the AMR packed bed regenerator considered.

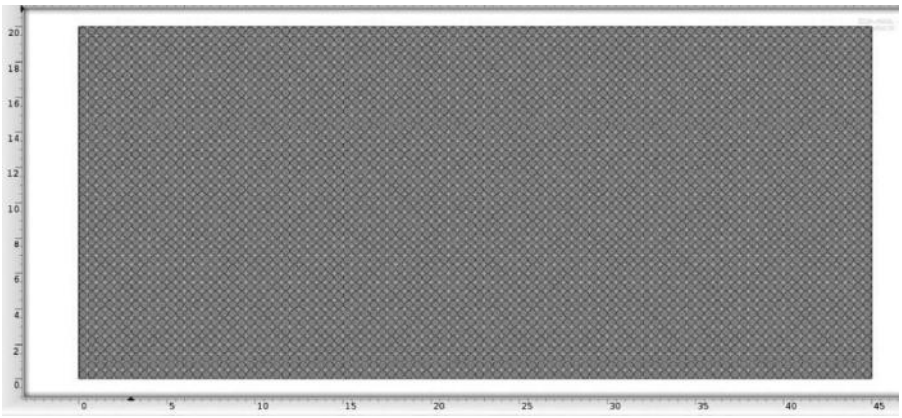

Figure III.27 *The packed bed AMR regenerator geometry: a 20x45mm wrapper contains 3600 spheres.*

The area of the parallel plate AMR regenerator contains 27 parallel plates made of gadolinium: every plate has a thickness of 0.5mm. The amount of the area occupied by all the plates is 60% of the total rectangular area. A group of channels is formed between the plates in the regenerator area, where the secondary fluid flows. Figure III.28 reports the parallel plate geometry of the regenerator.

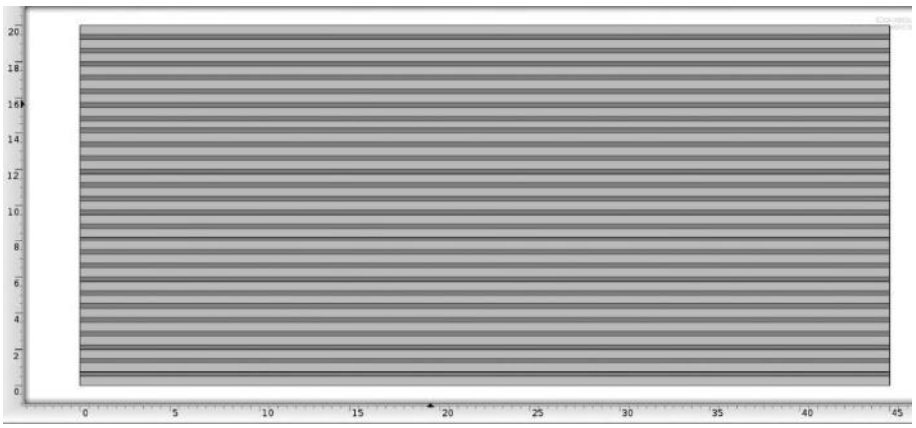

Figure III.28 *The parallel plate AMR regenerator geometry: a 20x45mm wrapper contains 27 plates and 26 channels.*

Both the models consider both the fluid flow and heat transfer between the solid and the fluid; the fluid flow in the positive x direction during the

isofield cooling process and in the opposite direction during isofield heating. The two models are supported by the same mathematical formulation which describes the AMR cycle, including several distinct groups of equations according to the different processes of the AMR cycle that the regenerator experiences (see section *III.2.2*).

III.6.2 Operating conditions

Several AMR cycles have been simulated on both the models in order to compare their performances by varying fluid flow rate at fixed AMR frequency. All the results have been obtained working with 1.25 Hz as AMR frequency, in the 288-298 K temperature range and investigating the regenerators behaviors while the secondary fluid velocity changes in 0.0595-0.25 m/s range.

The applied magnetic field has a variable intensity from 0 to 1.5 T. The secondary fluid employed is pure water, whereas the magnetocaloric material involved is gadolinium. Cold and hot heat exchangers temperatures (T_C = 288 K; T_H = 298 K) have been chosen in order to characterize the performance sensitivity of the regenerator in a range which embraces the gadolinium Curie temperature, i.e. 294 K.

III.6.3 Results

The results obtained are presented in terms of temperature span, cooling power, coefficient of performance (COP) and pump power, in order to quantify the pressure losses influence on COPs, for both the regenerator geometries. As a matter of fact, the results provide an indication about the operating conditions under which packed bed configuration has to be preferred to parallel plate and vice versa.

In Figure III.29 is reported the ΔT_{span} evaluated as in (III.13) for both the regenerator geometries under each fluid flow velocity investigated. The figure reveals that for both the model, the ΔT_{span} decreases with the fluid velocity. Indeed, corresponding to a small fluid mass flow rate, the fluid can be regenerated to reach lower cold side temperature. The maximum ΔT_{span} is reached in correspondence of a fluid velocity of about 0.1 m/s. Furthermore, one can observe that although, for low speed, packed bed configuration lets to ΔT_{span} greater than parallel plate ones, for high values of fluid velocity parallel plate geometry ensure larger temperature spans. The latter regenerator configuration seems to exhibit a less sensitive behavior with respect to velocity than the former, in terms of ΔT_{span}.

Figure III.30 reports the refrigeration power as a function of fluid velocity, obtained for packed bed and parallel plate AMR regenerator. The refrigeration power has been calculated according to the (III.14).

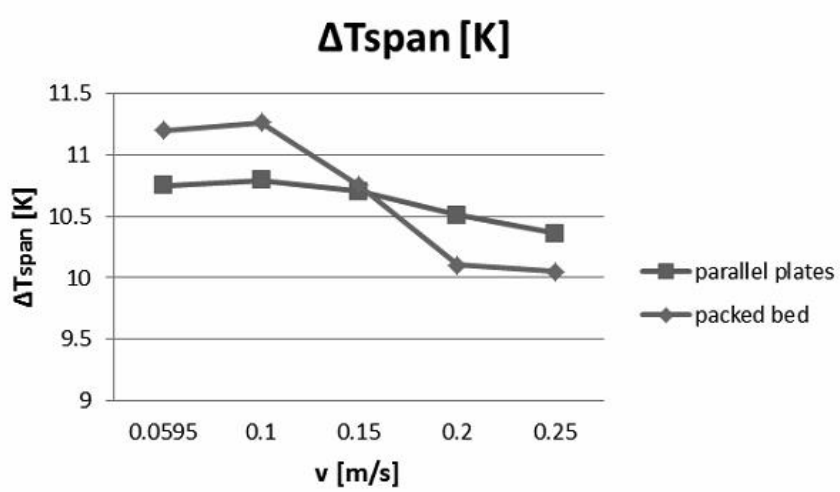

Figure III.29 *ΔT_{span} evaluated for both the regenerator configuration for variable fluid flow velocity and therefore fluid flow rate.*

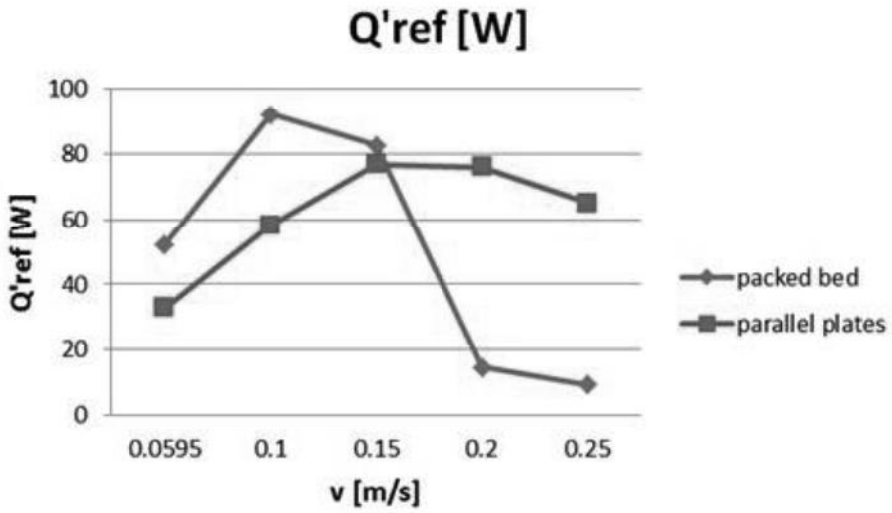

Figure III.30 *The refrigeration power evaluated for both the regenerator configuration for variable fluid flow velocity and therefore fluid flow rate.*

Figure III.30 clearly shows that the cooling power increases with the fluid flow rate and then decreases reaching a maximum. Indeed, corresponding to a small fluid mass, although the fluid can be regenerated to reach lower exit temperature, a small amount of transfer fluid can produce only a little refrigerating capacity. On the other hand, excessive quantities of transfer fluid perturb the temperature profile of the AMR, decreasing the temperature difference between the fluid and the bed. The bed quickly becomes

overwhelmed by the fluid flow and the efficiency of the heat transfer decreases quickly causing a loss in cooling power. From the figure one can observe that the points where the geometries confer the maximum refrigeration power differs from each other. As a matter of fact, if the secondary fluid has moved into the regenerator with a velocity of 0.15 m/s, packed bed and parallel plate configurations provide quite the same $\dot{Q}_{ref}$. Furthermore, with lower flow speeds, parallel plate shows a drastic reduction of its cooling capacity, higher than packed bed; whereas for values greater than 0.15 m/s, where a slump in packed bed's performances happens, parallel plate responds in a very satisfactory manner, providing refrigerant powers 3 times higher than the former geometry.

To estimate the performance of the two models, the Coefficient of Performance has been estimated as in (III.15). In Figure III.31 the COP evaluated for both the geometries by varying fluid flow rate, are reported. The figure clearly shows that COPs increase until reaching the maximum point whose value, in both the geometries, is the same (about 3), but the velocities where it is achieved are different. COPs show the same trends of refrigeration power: packed bed is better with low speed; parallel plate are to be preferred for high ones. A packed-bed regenerator is characterized by the best heat transfer surface, with a more marked pressure drop. A flat plate regenerator is characterized by a lower heat transfer surface and lower pressure drops. Therefore, another parameter is the responsible of such COP fall in packed bed configuration, for high velocity: pressure losses and, therefore, the mechanical power of the circulation pump.

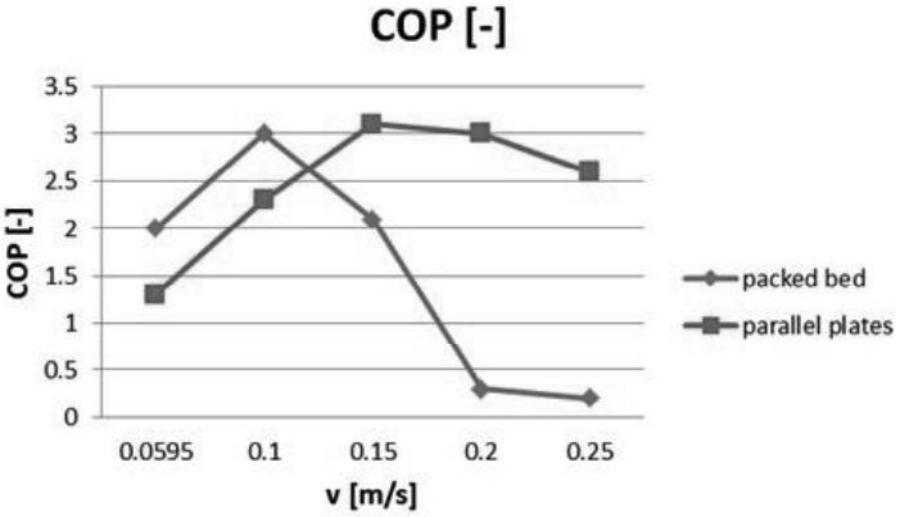

Figure III.31 *The refrigeration power evaluated for both the regenerator configuration for variable fluid flow velocity and therefore fluid flow rate.*

Figure III.32, which exhibits the work of the pump employed to allow the circulation of secondary fluid, reveals a significant reality: despite in the parallel plate configuration the pressure losses are negligible and not influenced by a change of velocity, a packed bed regenerator is strongly affected by pressure losses that seriously limit its operation at high flow speeds.

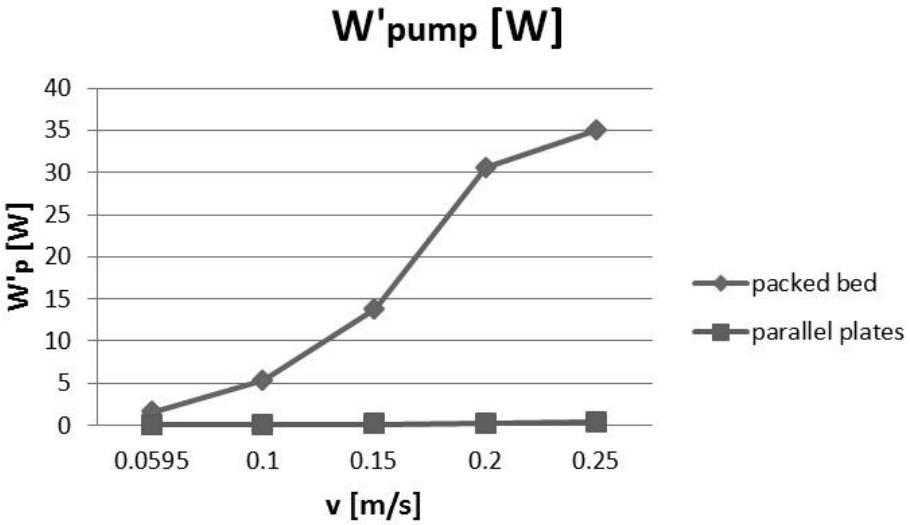

Figure III.32 *The work of the secondary fluid circulation pump reported versus fluid velocity.*

III.6.4 Considerations

After an accurate analysis of all the above-mentioned parameters, a general trend, which describes the performance of the two geometries under a general framework, has been carried out. It is possible to assert that for low values of fluid velocity, packed bed configuration has to be preferred since it offers ΔT_{span}, refrigeration power and COP higher than parallel plate ones and therefore a more satisfactory behaviour. For high flow speed the situation is completely upside down: parallel plate geometry provides good results whereas packed bed suffers a significant slump in its performance, caused also by a huge increment of pressure losses whom limits its use.

Conclusions

The present thesis aims to explore, report and explain all the aspects of the research about magnetic refrigeration, treated during the PhD period. The personal contribution in the above-mentioned research field has combined both the numerical and the experimental research that have been done hand in hand.

The first chapter contains an accurate description and illustration about all the generalities concerning magnetic refrigeration. Indeed, the purpose is to provide the reader with all the necessary tools required for understanding and deepening all the aspects of the investigations treated in the following chapters.

The second chapter illustrates the development of a Rotary Permanent Magnet Magnetic Refrigerator (RPMMR) and all the investigations made to explore its performance and to become aware of its limits and of the aspects to be optimized. The device, named 8Mag, has been developed at the Refrigeration Lab (LTF) of the University of Salerno in cooperation with the University of Naples "Federico II" and it is the first rotary magnetic refrigerator developed in Italy. To characterize the energy performances of 8Mag, it has been performed in various tests under different operating conditions. It has been tested its performances under zero load where a maximum temperature span of 13.5 K, under no thermal load, has been detected. Even if some efficiency losses were observed at low utilization factor, it has been asserted that the device operates as planned. Following two campaigns have been conducted in order to explore the energetic performances of 8Mag: 1) by changing the cycle frequencies, the cooling load and fluid flow rate, while the hot side temperature was fixed, in order to give an overview of the performances and to underline an optimal operating frequency, for each operating condition; 2) fixing flow rate and AMR cycle frequency to the optimal value, a further investigation has been conducted by varying cooling load. As a result of the experimental analysis, it has been observed that the behavior of 8Mag is in accordance with those of other devices built around the world. Furthermore, considering that 8Mag offers a reduction of thermal losses, it is possible to assert conclude that the tests presented here show promising performances. To improve the prototype,

new experimental tests focused on the identification of the worst causes of energy losses have been scheduled.

The third chapter treats all the aspects dedicated to the numerical modeling which operates parallel to the experimental tests. To this purpose a two-dimensional numerical model of a packed-bed AMR regenerator has been developed. The mathematical structure and the model implementations have been accurately described. Then the operating conditions and the results of its experimental validation with the 8Mag prototype have been illustrated.

Once validated the two-dimensional multiphysics model an investigation on new materials has been conducted in order to identify the best candidates to be employed in the 8Mag prototype. Different materials, among the rare-earth and transition metals, have been tested with the model as refrigerants and the tests performed reveal that from an efficiency point of view, the best candidates to magnetic refrigeration is $Gd_5(Si_2Ge_2)$ which exhibits the highest energetic performances when it is employed as magnetic refrigerant. On the other side $Gd_5(Si_2Ge_2)$ is a very expensive material, disadvantage which makes it impractical for every economic plan of magnetic refrigerator commercialization. As a matter of fact, it has been asserted that from a global point of view (performances and cost), the most promising materials are LaFeSiH compounds which are really cheaper than rare earth compounds and they give a performance sufficiently higher than gadolinium.

Then, evaluated the energetic performances of new magnetocaloric material, the environmental impact in terms of a greenhouse effect has been deepened. The energetic performances of a commercial R134a refrigeration plant have been compared to the AMR refrigerator working with the magnetocaloric materials previously tested and a comparison in terms of TEWI (Total Equivalent Warming Impact) index has been performed. The tests reveal that $Gd_5(Si_2Ge_2)$ and $LaFe_{11.384}Mn_{0.356}Si_{1.26}H_{1.52}$ have TEWI indexes always lower the ones of the vapor compression plant and that Gd, the benchmark material for magnetic refrigeration, shows a greenhouse effect similar to that of a vapor compression plant. These results indicate that magnetic refrigeration is a promising refrigeration technology that will be used in chiller applications. An AMR cycle can be an eco-friendly technology if used with magnetic materials that show a significant magnetocaloric effect.

Lastly, also the regenerator design has been investigated, since it is a key aspect in magnetic refrigeration. Attention has been focused on the magnetocaloric refrigerator design through the two-dimensional multiphysics numerical model working on two different magnetocaloric regenerators: (1) a packed bed and (2) a parallel plate magnetic regenerators made of gadolinium. It has been possible to assert that, for low values of fluid velocity, packed bed configuration should be preferred since it offers

energetic performances higher than parallel plate ones and therefore a more satisfactory behaviour. For high flow speed the situation is completely upside down: parallel plate geometry provides good results whereas packed bed suffers a significant slump in its performance, caused also by a huge increment of pressure losses whom limits its use.

The two-dimensional model and the prototype constitute an exhaustive apparatus able to walk hand in hand and to conduct the research on magnetic refrigeration to future developments aimed at getting closer to the day of large-scale trade and production of a magnetic refrigerator.

References

Aprea C., Maiorino A. (2010) A flexible numerical model to study an active magnetic refrigerator for near room temperature applications. *Appl. En.*, **87**, 2690–2698.

Aprea C., Greco A., Maiorino A. (2011a) A numerical analysis of an active magnetic regenerative cascade system. *Int. J. Energy Res.*, **35**, 177-188.

Aprea C., Greco A., Maiorino A. (2011b) A numerical analysis of an active magnetic regenerative refrigerant system with a multi-layer regenerator. *Energy Convers. Manag.*, **52**, 97-107.

Aprea C., Greco A. and Maiorino A. (2012a) An experimental evaluation of the greenhouse effect in the substitution of R134a with CO_2. *Energy*, **45**, 753-761.

Aprea C, Greco A and Maiorino A (2012b) Modeling an Active Magnetic Refrigeration system: a comparison with different models of incompressible flow through a packed bed. *Appl. Therm. Eng.*, **36**, 296-306.

Aprea C., Greco A. and Maiorino A. (2013) A dimensionless analysis or the optimization of an AMR cycle. *Int. J. En. Res.*, **37**, 1475-1487.

Aprea C., Cardillo G., Greco A., Maiorino A. and Tura A. (2014a) Design and construction of an experimental Rotary Permanent Magnet Magnetic Refrigerator. Proc. of the *6th IIR/IIF International Conference on Magnetic Refrigeration at Room Temperature, THERMAG 2014;* September 7-10, 2014, Victoria, Canada.

Aprea C., Greco A., Maiorino A., Mastrullo R. and Tura A. (2014b) Initial experimental results from a rotary permanent magnet magnetic refrigerator, *Int. J. Refrig.*, **43**, 111–122.

Aprea C., Cardillo G., Greco A., Maiorino A. and Masselli C. (2015a) A comparison between experimental and 2D numerical results of a packed-bed active magnetic regenerator. *Appl. Therm. Eng.*, **90**, 376-383.

Aprea C., Greco A., Maiorino A. and Masselli C. (2015b) A comparison between rare earth and transition metals working as magnetic materials in an AMR refrigerator in the room temperature range. *Appl. Therm. Eng.*, **91**, 767-777.

Aprea C., Greco A., Maiorino A. and Masselli C. (2015c) Magnetic refrigeration: an eco-friendly technology for the refrigeration at room temperature. *J. of Phys.: Conf. Ser.* **655** (1), 012026.

Aprea C., Greco A. and Maiorino A. (2016a) An experimental investigation on the substitution of HFC134a with HFO1234yf in a domestic refrigerator. *Appl. Therm. Eng.*, **106**, 959-967.

Aprea C., Greco A., Maiorino A. and Masselli C. (2016b) A two-dimensional investigation about magnetocaloric regenerator design: parallel plates or packed bed? Proceedings of *34th UIT Heat Transfer Conference*, July 04-06, 2016, Ferrara, Italy.

Aprea C., Greco A., Maiorino A. and Masselli C. (2016c) The energy performances of a rotary permanent magnet magnetic refrigerator. *Int. J. of Refrig.*, **61**, 1-7.

Aprea C., Cardillo G., Greco A., Maiorino A. and Masselli C. (2016d) A rotary permanent magnet magnetic refrigerator based on AMR cycle. *Appl. Therm. Eng.*, **101**, 699-703.

Bahl C.R.H, Engelbrecht K., Eriksen D., Lozano J.A., Bjørk R., Geyti J., Nielsen K.K., Smith A. and Pryds N. (2014) Development and experimental result from a 1 kW prototype AMR. *Int. J. Refrig.*, **37**, 78-83.

Balli M., Sari O., Mahmed C., Besson C., Bonhote P., Duc D. and Forchelet J. (2012) A pre-industrial magnetic cooling system for room temperature application, *Appl. Energy*, **98**, 556–561.

Barclay J.A. (1982). The theory of an active magnetic regenerative refrigerator. *Los Alamos report*, LA-UR, **83**, 1251.

Barclay J.A (1994) Active and passive magnetic regenerators in gas/magnetic refrigerators. *J. All. Comp.*; **207**-**208**, 355–361.

Bjørk R., Bahl C.R.H. and Katter M. (2010a) Magnetocaloric properties of $LaFe_{13-x-y}Co_xSi_y$ and commercial grade Gd. *J. Magn. Magn. Mater.*, **322** (24), 3882-3888.

Bjørk R., Bahl C.R.H., Smith A. and Pryds, N. (2010b) Review and comparison of magnet designs for magnetic refrigeration. *Int. J. Refrig.*, **33** (3), 437-448.

Blanco J.A., Gignoux D. and Schmitt D. (1991) Specific heat in some gadolinium compounds. II. Theoretical model. *Phys. Rev. B*, **43** (13), 145-151.

Bouchard J., Nesreddine H. and Chahine R. (2005) Impact of demagnetization on magnetocaloric effect in pure gadolinium. Proc. of the *1st IIR/IIF International Conference on Magnetic Refrigeration at Room Temperature, THERMAG 2005;* September 28-30, 2005 Montreux, Switzerland.

Bouchard J., Nesreddine H. and Galanis N. (2009) Model of a porous regenerator used for magnetic refrigeration at room temperature. *Int. J. Heat. Mass Transf.*, **52,** 1223-1229.

Bouvier M., Lethillier P. and Schmitt D. (1991) Specific heat in some gadolinium compounds. I. Experimental. *Phys. Rev. B*, **43** (13) 137-144.

Brown G.V. (1976) Magnetic heat pumping near room temperature. *J. Appl. Phys.*, **47** (8), 3673-3680.

Chen J.C. and Yan Z.J. (1998) The effect of thermal resistances and regenerative losses on the performance characteristics of a magnetic Ericsson refrigeration cycle. *J. Appl. Phys*., **84** (4), 1791–1795.

Dan'kov S.Y., Tishin A.M., Pecharsky V.K. and Gschneidner Jr. K.A. (1998) Magnetic phase transitions and the magneto-thermal properties of gadolinium. *Phys Rev. B*, **57** (6), 3478-3490.

de Oliveira N.A. and von Ranke P.J. (2005) Theoretical calculations of the magnetocaloric effect in $MnFeP_{0.45}As_{0.55}$: a model of itinerant electrons, *J. Phys. Condens. Matter*, **17**, 3325-3332.

Debye P. (1926) Einige bemerkungenzur magnetisierungbeitiefer, temperatur. *Ann. of Phys.*, **81**, 1154-1160.

Dikeos J., Rowe A., and Tura A. (2006) Numerical analysis of an active magnetic regenerator (AMR) refrigeration cycle. Proc. of *AIP Conference*, **823**; July 26-27, 2006, Syracuse, New York (USA).

Dikeos J. and Rowe A. (2013) Validation of an active magnetic regenerator test apparatus model. *Int. J. Refrig.*, **36**, 921–931.

Engelbrecht K., Eriksen D., Bahl C.R.H., Bjørk R., Geyti J., Lozano J.A., Nielsen K.K., Saxild F., Smith A. and Pryds N. (2012) Experimental results for a novel rotary active magnetic regenerator. *Int. J. Refrig.*, **35** (6), 1498-1505.

Engelbrecht K. and Pryds. N. (2014) Progress in magnetic refrigeration and future challenges. Proc. of the *6th IIR/IIF International Conference on Magnetic Refrigeration at Room Temperature, THERMAG 2014;* September 7-10, 2014, Victoria, Canada.

Ergun S. (1952) Fluid flow through packed columns. *Chem. Eng. Prog.*, **48** (2), 89-94.

Eriksen D., Engelbrecht K.L., Bahl C.R.H., Bjørk R., Nielsen K.K., Insiga A.R. and Pryds N. (2015) Design and experimental tests of a rotary active magnetic regenerator prototype. *Int. J. Refrig.*, **58**, 14-21.

EU No 517/2014, European Regulation No 517/2014 on fluorinated greenhouse gases and repealing Regulation (EC) No 842/2006, 2014, *Off. J. Eur. Union.*

Franco V., Blazquez J.S., Ingale B. and A. Conde (2012) The Magnetocaloric Effect and Magnetic Refrigeration Near Room Temperature: Materials and Models. *Annu. Rev. Mater. Res.*, **42**, 305–342.

Gao Q., Yu B.F., Wang C.F., Zhang B., Yang D.X. and Zhang Y. (2006) Experimental investigation on refrigeration performance of a reciprocating active regenerator of room temperature magnetic refrigeration. *Int. J. Refrig.*, **29**, 622–636.

Giauque W.F. (1927) A thermodynamic treatment of certain magnetic effects. A proposed method of producing temperatures considerably below 18 absolute. *J. of the Amer. Chemic. Soc.*, **49**, 1864-1870.

Griffel M., Skochdopole R.E. and Spedding F.H. (1954) The heat capacity of gadolinium from 15 to 355 K. *Phys. Rev.*, **93** (4), 657-61.

Guillou F., Legait U., Kedous-Lebouc A. and Hardy V. (2012) Development of a new magnetocaloric material used in a magnetic refrigeration device, Proc. of *EPJ Web of Conferences, EMM-FM2011 - First Euro Mediterranean Meeting on Functionalized Materials*, **29**.

Guillou F., Porcari G., Yibole H., van Dijk N. and Brück E. (2014) Taming the first-order transition in giant magnetocaloric materials. *Adv. Mater.*, **26**, 2671-2675.

Hu F.X., Shen B.G., Sun J.R., Cheng Z.H., Rao G.H. and Zhang X.X. (2001) Influence of negative lattice expansion and metamagnetic transition on magnetic entropy change in the compound $LaFe_{11.4}Si_{1.6.}$ *Appl. Phys. Lett.*, **78,** 3675–3677.

Holtzberg F., Gambino R. J. and McGuire T. R. (1967) New ferromagnetic 5 : 4 compounds in the rare earth silicon and germanium systems. *J. Phys. Chem. Solids*, **28** (11), 2283-2289.

Kaviany M. (1995) *Principles of Heat Transfer in Porous Media*. Springer, New York, NY, p. 33, 46-47, 130, 228-229.

Kitanovski A. and Egolf P.W. (2006) Thermodynamics of magnetic refrigeration. *Int. J. of Refrig.*, **29** (1), 3-21.

Kitanovski A., Tomc U. and Poredos A. (2016) Future developments in magnetocaloric refrigeration and heat pumping. Proc. of the *7th IIR/IIF International Conference on Magnetic Refrigeration at Room Temperature,THERMAG 2016;* September 11-14, 2016, Turin, Italy.

Jotani Y., Kanha Y., Ishizuka M. and Tsutsumi A. (2014) Experimental investigation of an active magnetic regenerative heat circulator applied to self-heat recuperation technology. *Appl. Therm. Eng.*, **70** (2), 1202-1207.

Kyoto Protocol to the United nation Framework Convention on climate change. United Nation Environment Program (UN), 1997, Kyoto, JPN.

Lawton Jr L.M., Zimm C.B. and Jastrab A.G. (1999) Reciprocating active magnetic regenerator refrigeration apparatus. *U.S. Patent No*. **5**, 934, 078.

Law Y., Franco V., Keblinski P. and Ramanujam R.V. (2013) Active transient cooling by magnetocaloric materials. *Appl. Therm. Eng.*, **52** (1), 17-23.

Lionte S., Vasile C. and Siroux M. (2015) Numerical analysis of a reciprocating active magnetic regenerator. *Appl. Therm. Eng.*, **75**, 871-879.

Liu Y., Infante I.C., Lou X., Bellaiche L., Scott J.F. and Dkhil B. (2014) Giant Room-Temperature Elastocaloric Effect in Ferroelectric Ultrathin Films. *Adv. Mat.*, **26** (35), 6132-6137.

Lozano J.A., Engelbrecht K., Bahl C.R.H., Nielsen K.K., Eriksen D., Olsen U.L., Barbosa Jr. J.R., Smith A., Prata A.T. and Pryds, N. (2013) Performance analysis of a rotary active magnetic refrigerator. *Appl. En.*, **111**, 669-680.

Lozano J.A., Engelbrecht K., Bahl C.R.H., Nielsen K.K., Barbosa Jr. J.R., Prata A.T. and Pryds N. (2014) Experimental and numerical results of high frequency rotating active magnetic refrigerator. *Int. J. Refrig.*, **37**, 92–98.

Lu S.G., Rožič B., Zhang Q.M., Kutnjak Z., Li X., Furman E., Gorny L.J., Lin M., Malič B., Kosec M., Blinc R. and Pirc R. (2010) Organic and inorganic relaxor ferroelectrics with giant electrocaloric effect. *Appl. Phys. Lett.*, **97** (16), 162904.

Montreal Protocol on substances that deplete the ozone layer. United Nation Environment Program (UN), 1987, New York (NY), USA.

Morrison K., Sandeman K.G., Cohen L.F., Sasso C.P., Basso V., Barcza A., Katter M., Moore J.D., Skokov K.P. and Gutfleisch O. (2012) Evaluation of the reliability of the measurement of key magnetocaloric properties: a round robin study of La(Fe,Si,Mn)H_δ conducted by the SSEEC consortium of European laboratories. *Int. J. Refrig.*, **35** (6), 1528-1536.

Mota-Babiloni, A., Navarro-Esbrí, J., Molés, F., Barragán-Cervera, A., Peris, B. and Verdù, G. (2016) A review of refrigerant R1234ze(E) recent investigations. *Appl. Therm. Eng.*, **95**, 211–222.

Niemann R., Diestel A., Backen A., Rossler U.K., Behler C., Hahn S., Wagner M.F., Schultz L. and Fahler S. (2014) Controlling reversibility of the magneto-structural transition in first-order materials on the micro-scale Proc. of the *6th IIR/IIF International Conference on Magnetic Refrigeration at Room Temperature, THERMAG 2014;* September 7-10, 2014, Victoria, Canada.

Oliveira P., Trevizoli P., Barbosa J. and Prata T. (2012) A 2D hybrid model of the fluid flow and heat transfer in a reciprocating active magnetic regenerator. *Int. J. Refrig.*, **35**, 98-114.

Ožbolt M., Kitanovski A., Tušek J. and Poredoš A. (2014) Electrocaloric refrigeration: thermodynamics, state of the art and future perspectives. *Int. J. of Refrig.*, **40**, 174-188.

Palm B. (2008) Hydrocarbons as refrigerants in small heat pump and refrigeration systems – A review. *Int J of Refr*, **31** (4), 552-563.

Pecharsky V.K. and Gschneidner Jr K.A. (1997) Giant magnetocaloric effect in Gd5(Si2Ge2). *Phys. rev. lett.*, **78**(23), 4494.

Phana M.H. and Yub S.C. (2007) Review of the magnetocaloric effect in manganite materials. *J. of Magn. and Magn. Mat.*, **308**, 325–340.

Romero Gómez J., Ferreiro Garcia R., Carbia Carril J. and Romero Gómez M. (2013) Experimental analysis of a reciprocating magnetic refrigeration prototype. *Int. J. Refrig.* **36** (4), 1388-1398.

Russek, S., Auringer, J., Boeder, A., Chell, J., Jacobs, S. and Zimm, C. (2010) The performance of a rotary refrigerator with layered beds. Proc. of the *4th IIR/IIF International Conference on Magnetic Refrigeration at Room Temperature, THERMAG 2010;* August 23-27, 2010, Baotou, Inner Mongolia, China.

Sandeman K.G. (2014) DDREAM: reducing rare earth use in magnetocaloric applications. Proc. of the *6th IIR/IIF International Conference on Magnetic Refrigeration at Room Temperature, THERMAG 2014;* September 7-10, 2014, Victoria, Canada.

Scarpa F., Tagliafico G. and Tagliafico L.A. (2012) Control optimization in experiments for the heat transfer assessment of saturated packed bed regenerators. *Int. J. Heat. Mass T.*, **55** (23-24), 6944-6950.

Tagliafico L.A., Scarpa F., Valsuani F. and Tagliafico G. (2013) Preliminary experimental results from a linear reciprocating magnetic refrigerator prototype. *App. Therm. Eng.*, **52** (2), 492-497.

Tomc U., Tušek J., Kitanovski A. and A. Poredos (2013) A new magnetocaloric refrigeration principle with solid state thermo-electric thermal diodes. *Appl. Therm. Eng.*, **58** (1-2),1-10.

Trevizoli V.P., Barbosa Jr. J.R., Oliveira P.A., Canesin F.C. and Ferreira R.T.S. (2012) Assessment of demagnetization phenomena in the performance of an active magnetic regenerator. *Int. J. Refrig.*, **35** (4), 1043-1054.

Tura, A. and Rowe A. (2011) Permanent magnet magnetic refrigerator design and experimental characterization. *Int. J. Refrig.*, **34** (3), 628-639.

Tušek J., Kitanovski A., Zupan J., Prebil I. and Poredoš A. (2013) A comprehensive experimental analysis of gadolinium active magnetic regenerators. *Appl. Therm. Eng.*, **53** (1), 57-66.

Tušek J., Engelbrecht K., Millán-Solsona R., Mañosa L., Vives E., Mikkelsen L.P. and Pryds N. (2015) The Elastocaloric Effect: A Way to Cool Efficiently. *Adv. Energy Mater.* **5** (13).

Velazquez D., Palacios E., Beltran J. and Burriel R. (2014) A 2D numerical model for a parallel plate regenerator and parameter analysis. Proc. of the *6th IIR/IIF International Conference on Magnetic Refrigeration at Room Temperature, THERMAG 2014;* September 7-10, 2014, Victoria, Canada.

von Moos L., Bahl C.R.H., Nielsen K.K. and Engelbrecht K. (2015) The influence of hysteresis on the determination of the magnetocaloric effect in $Gd_5Si_2Ge_2$. *J. Phys. D Appl. Phys.*, **48,** 1e7.

Vuarnoz D. and Kawanami T. (2012) Numerical analysis of a reciprocating active magnetic regenerator made of gadolinium wires. *Appl. Therm. Eng.*, **37**, 388-395.

Vuarnoz D. and Kawanami T. (2013) Experimental validation of a coupled magnetothermal model for a flat parallel-plate active magnetic regenerator. *Appl. Therm. Eng.*, **54** (2), 433-439.

Warburg E. (1881) Magnetische Untersuchungen. Über einige Wirkungen der Coërcitivkraft. *Ann. Phys*, **13**, 141-164.

Yu B.F., Gao Q., Zhang B., Meng X.Z. and Chen Z. (2003) Review on research of room temperature magnetic refrigeration. *Int. J. of Refrig.*, **26** (6), 622-636.

Yu B., Liu M., Egolf P.W. and Kitanovski A. (2010) A review of magnetic refrigerator and heat pump prototypes built before 2010. *Int. J. Refrig.*, **33**, 1029-1060.

Zamni L., El Maudni El Alami S., Balli M., Forchelet J. and Sari O. (2012) Corrosion tests of gadolinium in various heat conducting fluids. Proc. of the *5th IIR/IIF International Conference on Magnetic Refrigeration at Room Temperature, THERMAG 2012;* September 17-20, 2012, Grenoble, France.

Zimm C. (2003) Rotating bed magnetic refrigeration apparatus, 2003, US Patent 6,526,759.

Zimm C., Boeder A., Chell J., Sternberg A., Fujita A., Fujieda S. and Fukamichi K. (2006) Design and performance of a permanent-magnet rotary refrigerator. *Int. J. Refrig.*, **29** (8), 1302–1306.

List of symbols

Roman symbols

A	cross section of the regenerator, m2
B	magnetic field induction, T
$\bar{B}$	average magnetic field intensity, T
C	heat capacity, J. kg-1. K-1
CO_2	CO_2 contribution to global warming, kg_{CO2}
COP	coefficient of performances, -
D	diameter, m
f	frequency, Hz
F	factor, Pa
GWP	global warming potential, kg_{CO2}. kg-1
H	annual operating hours
H	magnetic field intensity, A. m-1
k	thermal conductivity, W. m-1. K-1
L	length, m
m	magnetic moment
m’	fluid flow rate, kg. s-1
M	magnetization, A. m-1
M	mass, kg
p	pressure, Pa
P	fraction of an AMR cycle
P	percent leak rate, %
Q	heat, J
Q’	thermal power, W
RC	refrigerant charge, kg_{CO2}
RCP(S)	entropy relative cooling power, J/kg
RCP(T)	temperature relative cooling power K2
S	entropy, J. K-1
s	specific entropy, J. kg-1. K-1
T	temperature, K
t	time

t	time duration of every AMR process, s
TEWI	total equivalent warming impact, kg_{CO2}
u	longitudinal velocity, m.s-1
V	plant useful life, yr
V	velocity, m. s-1
V	volume, m+3
V’	volumetric fluid flow rate, l. min-1
v	orthogonal velocity, m.s-1
W	work, J
W’	power, W
X	longitudinal spatial coordinate, m
y	orthogonal spatial coordinate, m

Greek symbols

α	CO_2 emission from power conversion, kg_{CO2}. kWhyr-1
Δ	finite difference
δ	factor, -
δ	width, K
ε	mean porosity, -
θ	rotation angle, rad
η	isentropic efficiency
Λ	magnetic parameters, T2.-3
μ	dynamic viscosity, kg. m-1. s-1
μ	magnetic permeability, H. m-1
ν	cinematic viscosity, m2. s-1
ρ	density, kg. m-3
τ	duration of a whole AMR cycle, s
ϕ	utilization factor, -
χ	magnetic susceptibility, -
ω	angular velocity, rad. s-1

Subscripts

0	undisturbed
0	vacuum
ad	adiabatic
add	additional
AMR	active magnetic regenerator
B	breakdown
C	cold reservoir
c	Curie

CF	cold-to-hot fluid flow
closed	hole fully closed
cool	performance
demagn	demagnetization
dir	direct
el	electronic
el,h	absorbed by electric heater
el,m	absorbed by electric motor
el,p	absorbed by the pump
Ergun	Ergun equation
f	fluid
field	high magnetic field intensity
FWHM	full width half maximum
H	hot reservoir
H	constant magnetic field
HF	hot-to-cold fluid flow
HFi	fluid outgoing from the probe
HFo	fluid outgoing from hot side
High	high magnetic field
in	inlet
indir	indirect
L	lattice
L	regular
LFo	fluid outgoing from cold side
loss	difference between AMR and span
Low	low magnetic field
M	constant magnetization
M	magnetization phase
M	magnetic
Mag	magnets
magn	magnetization
max	maximum
opening	hole opening
out	outlet
p	constant pressure
p	particle
p	pump
PB	packed bed
R	refrigerant recycling
r	regeneration
r	relative permeability index
ref	refrigerant
rej	rejected
S	constant entropy

s	solid
span	difference
ST	structural
T	constant temperature
VC	vapor compression plant